

Response to Referees

Atmospheric Chemistry and Physics

Taquet et al.: “CO₂ and CO temporal variability over Mexico City from ground-based total column and surface measurements”

We thank the two reviewers for their very constructive comments, which helped to prepare an improved revised manuscript.

1. Response to Reviewer #1

Overview:

The paper by Taquet et al reports on measurements from Mexico City, including three sites, two within the city itself and one at the high-altitude site at Altzomoni. This group is very experienced in FTIR columns measurements, using both high resolution FTIR spectrometers at fixed locations as part of the NDACC/TCCON networks, but also the use of portable EM27/SUN FTIR spectrometers in the COCCON network. This study uses quite an extensive set of data and a methodology based on previous work reported by Stremme et al in 2013. The data set and instrumentation are described in good detail, and any reader who wishes to understand the exact procedure will need to refer to the Stremme paper for details. It is my impression that what the authors produce here is a very promising report of Mexico emissions over a 5-year period and are able to compare this with in situ data as well as satellite based TROPOMI measurement. Within the constraints of their method, that is a simplified approach that avoids the use of complicated modelling, these data sets seem to compare well, given the spatial and inherent uncertainty limitations of the ground-based column measurements.

In terms of principal criteria, the manuscript is rated as good (3) for scientific significance (the methods are not new but are followed with a highly experienced team), rated excellent (4) for scientific quality, and in general rated as good(3) to excellent(4) in presentation quality (see technical corrections below)

In general, the manuscript is well written, gives a very good scientific motivation for the work, has clear description of the measurements and references the paper by Stremme where a very detailed account of the method can be read (not required to be repeated here).

Comments:

Given that understanding of emissions in mega cities is a global question, is the study method only limited to Mexico City? Could this method be applied to others cities or does Mexico city offer very unique geography that means this cannot really be applied elsewhere?

Reply: We thank the reviewer for highlighting this aspect. Indeed, the simple methodology employed in our manuscript for estimating emissions holds potential applicability to cities experiencing periods of reduced ventilation during some hours of the day and therefore it mainly depends on the geographical location and topography. For cities characterized by flat topography, the wind might play a key role and correlation between wind direction/speed and the carbon monoxide column might be important for most approaches.

There are already plenty of approaches for satellite-based column measurements like Pommier et al. (2013) and Tu et al. (2020), which map the measurements upwind and downwind the source to estimate the emissions. Conceptually, a similar approach could be applied using two or more ground-based instruments (Hase et al., 2015; Chen et al., 2016; Frey et al., 2018) positioned upwind and downwind of the urban plumes. However, the efficacy of such methodologies is contingent upon meteorological conditions, often limiting emission estimates to short-term periods and constraining statistical analyses. This is the case in our study during which the UNA station was dominantly downwind (see Figure S6) under the prevailing wind conditions, and VAL never is a representative background station because of its situation in a highly industrialized area. Our methodology has so far only been applied to Mexico City (Stremme et al., 2013), which presents a special combination of low daytime ventilation conditions and an urban area large enough for the column growth rate to be dominated by the emission flux. Most cities fall somewhere in between the limits where the growth rate of the column is directly related to emission fluxes and the downwind-upwind difference is an important key to get the emissions. However, it is likely that a similar simple method, tailored to the unique geography of each city, might be applicable in many cases.

In our manuscript we added at l. 875:

“The methodology employed here for monitoring the long-term temporal variability of CO emission fluxes is likely to be adapted to other urban areas where the topography damps the ventilation down for several hours each day, thereby establishing that the column growth rate is dominated by the emission flux.”

Why not use a chem/trans model in this study? Clearly there is the yet to be published study by Che et al presumably on a subset of this data. Are there specific reasons why a more complicated modelling exercise is not undertaken for the entire measurement record by these authors? Is the suggestion that this simpler approach here should be adopted elsewhere?

Reply: A chemical/transport model provides valuable information to track cities emissions and understand the source processes using either surface or columnar measurements. Che et al. (2024) and Che et al. (submitted to *Journal of Geophysical Research*) successfully estimate Mexico city CO₂ emissions using the data of the MERCI-CO₂ intensive campaign (Oct2020 - May 2021) and obtains very consistent results with inventories using both space- and ground-based measurements and the lagrangian XSTILT model.

Nevertheless, such models necessitate substantial computational time and memory resources and a large number of measurement stations to ensure statistical robustness.

Such models require some approximations due to the available data (i.e., meteorological fields, prior information, background estimate, etc.), which, while partially representative of the complexity of atmospheric turbulence and mixing at fine spatial and temporal scales, are not exhaustive. The optimization of the model configuration, which relies on specific parametrizations, can be not straightforward, in particular for long-term periods and, particularly in regions with complex orography. Despite numerous recent efforts to quantify the different types of error due to these approximations, it remains a challenge to ascertain to what extent the results depend on the assumptions and parameters used.

Our study highlights that at specific stations and under specific climatic and topographic conditions, columnar measurements and their growth rate are directly connected to emissions. The emission data derived directly from columnar measurements provide independent information from the transport/chemistry models. This data can be used not only to explore the temporal variability of the emissions of a city but also to identify possible inaccuracies in the parameterization of complex models. Nevertheless, it is evident that our approach cannot supplant more sophisticated chemical transport models in furnishing more precise data or absolute values concerning emissions, chemical transport, and sources.

We thank the reviewer for raising this point and add at the end of the manuscript at 1.878:

“Although the straightforward model presented here is not intended to replace a complex transport/chemical model for a precise estimate of city emissions, the results obtained demonstrate that it is nevertheless possible to track their temporal evolution with a high degree of reliability.”

A few other comments;

1. Page 19, line 561: are these low costs sensors different to the CO₂ sensor mentioned on page 7?

Reply: We thank the reviewer for mentioning this unclear point:

The low cost sensors mentioned at this line of the manuscript are the same as the one referred to in page 7. The following description was added to Page 7 of the new manuscript, line 220:

“Additionally, the VAL site included a low-cost medium precision CO₂ sensor, as a part of a network implemented during the MERCI-CO₂ campaign. It consists of a NDIR-type of sensor (SenseAir, model HPP3) that can measure in the 0 to 1000 ppm range and after a calibration and target gas follow-up procedure, can produce data with <1% accuracy (Porrás et al., 2023).” We also added the reference Porrás et al. (2023) at line 566.

2. Page 21, lines 619/620: what is the significance of these slight decreases?

Reply: The slight decrease observed in the ΔXCO atmospheric concentration trend (which is consistent with the surface CO decreasing trend) was also

reported in other longer-term studies (Garcia-Franco, et al., 2019; Molina, 2021, Hernández-Paniagua et al., 2021). The decreasing trend likely results from the successive air quality management programs implemented in the CDMX since the 1990s to improve the air quality, which combined regulatory actions with technological change based on scientific, technical, social, and political considerations (Molina, 2021). Vehicle emissions were curbed through technological advancements and fuel quality enhancements (including removal of lead from gasoline, mandatory use of catalytic converters, reinforcement of vehicle inspection and maintenance, mandatory “no driving day” rule), while industrial and commercial emissions were mitigated by measures such as refinery closures, industrial relocation, fuel substitution, ect. The decreasing trend is also accentuated by including in the analysis the COVID-19 lock-down period, for which the monthly variability and average significantly decreased compared to the previous years. The slight decrease also observed for ΔXCO_2 in Figure 8 likely reflects the same facts, given that an important part of anthropogenic CO_2 emissions in Mexico are due to the mobile sources.

We added in the manuscript in 1.639:

“The long term $\Delta_m XCO$, also observed in other studies (Garcia-Franco, et al., 2020; Molina, 2021, Hernández-Paniagua et al., 2021) likely reflect the successive air quality management programs implemented in the CDMX since the 1990s to improve the air quality, including technological advancements and fuel quality enhancements as well as refinery closures, industrial relocation, or fuel substitution.”

3. Page 21, line 622: possible reasons for the low ratios?

Reply: The observation of lower $\Delta XCO/\Delta XCO_2$ ratios during the raining season (where both CO and ΔXCO_2 are minimum) are in accordance with the observation of Linian-Abanto et al. (2021). This seasonal dependence could be the result of (1) a change in the relative contribution of the different types of sources measured at the stations driven by a change in the dominant wind direction (2) a change in the turbulence/mixing conditions and pollutant concentration driven by the meteorological synoptic patterns.

- (1) Typically low emission ratios ($CO/CO_2 < 0.02$) correspond to high combustion efficiencies, originating from the burning of well-processed liquid fuels or gasses (vehicle engines, natural gas stoves, etc.) while higher emission ratios (CO/CO_2 from 0.03 to 0.1) reflect low combustion efficiency, due to use poorly processed solid fuels (coal stoves or biofuels, biomass burning, etc.) (Liñán-Abanto et al., 2021 and therein references). Therefore higher $\Delta XCO/\Delta XCO_2$ are expected during the typical period of the biomass burning contrasting with the rest of the year.
- (2) Since this seasonal occurrence of low ratio during the rain season is observed at both VAL and CCA sites, it is likely explained by synoptic meteorological patterns. Typically, within the MCMA, the most severe pollution episodes happen in winter (cold dry season) and spring (warm dry season) due to the formation of strong surface-based inversions overnight and early in the morning.

These inversions create highly stratified atmospheric conditions that trap vehicle emissions and industrial pollutants near the surface. Late spring is the season when ozone concentrations in México City often surpass the normative limits and the government takes action to reduce emissions from the traffic sector. Conversely, in summer, a deep easterly flow over Mexico City brings abundant tropical moisture from the Gulf of Mexico, resulting in frequent cloud cover and rainfall. This weather pattern reduces the occurrence and intensity of nocturnal inversions and aids in washing away pollution. Therefore, the lower $\Delta XCO/\Delta XCO_2$ levels observed during the rainy season are likely due to a reduced contribution of polluted air masses originating from the city.

We added in line 643: “Regarding the low seasonal variability observed for the CO/CO₂ ratios, it is likely related to mass burning episodes and high-pressure weather conditions that occur during the dry season.”

4. Page 22, line 654: are there other independent traffic patterns that might shed light on the lack of lock-down signal?

Reply: A difference in the ΔXCO_2 and ΔXCO (UNA-VAL) was expected during the COVID-19 lock-down period, especially for CO, because the main source of CO near UNAM is the road traffic, in contrast with the Northern part of the city, which is highly industrialized. Due to the suspension of the academic activity, reduced business activity and remote work becoming widespread during the COVID19 lock-down period, the reduction of the road traffic in this area was significant (Hernández-Paniagua et al., 2021: Supplementary Material Table S1).

The absence of lower ΔCO (UNA-VAL) values in Figure 10 shows either that the decrease in the CO emissions is homogeneous across the city or that some other phenomenon is masking the local decrease in these emissions. In the study by Hernández-Paniagua et al. (2021), which examines the impact of the COVID-19 lockdown on the MCMA air quality, the effect of the lockdown is clearly observed regarding the NO₂ (a robust tracer of motor vehicle emissions) variability but much less evident for CO. They first highlight the role of the meteorological conditions (accumulation of contaminants during stagnant atmospheric conditions which can mask their temporal variability) and attribute the quasi absence of the CO anomaly to a possible increase of the domestic liquid petroleum and natural gas burning because of the stay-at-home order.

Figure 3 of our study shows a negative anomaly during these months at both VAL and UNA stations, showing that the long-term total column variability captured a decrease of the CO emissions due to the global lock-down effect at the two stations. However, the fact that no difference is observed in horizontal (VAL-UNAM) ΔCO gradients shows that the two stations captured the composition of a homogeneously mixed layer, which may be due to the stagnant atmospheric conditions that tend to favor the accumulation of pollutants (i.e: on an intraday scale), and mask the impact of local sources.

Technical Corrections:

1. Page 6, line 179: Nation -> Nafion **Done**
2. Page 7, line 215: what is the CO2 sensor (ie, type, model etc)?

Reply: See response to the comment 1

3. Page 9, line 279: remove “the” **Done**
4. Page 9, line 295: remove “the” **Done**
5. Page 10, line 324: “in order of” probably sounds better with “of order of” **Done**
6. Page 18, line 553: “the total columns XCO2 and XCO” -> “the total column mole fractions XCO2 and XCO...” **We replace this part by “The XCO₂ and XCO” to simplify the text, the XCO₂ and XCO being defined before.**
7. Page 24, line 684: “ upwind the city...” -> “upwind of the city...” **Done**
8. Page 24, line 689: “ ..in the Stemme...” -> “ ..in Stremme ...” **Done**
9. Page 24, line 698: “... mountain around ...” -> “ ... mountains around...” **Done**
10. Page 24, line 709: “... would be ..” -> “ ...is...” **Done**
11. Page 24, line 711-714: does it matter though if these uncertainties have both systematic and random components?

Reply: We agree with the reviewer that the relative contribution of the random and systematic error is not reported in our manuscript. As we aim to estimate the average emissions, we only use one “extrapolation factor” in time and space. By definition, random error can be reduced by $\sqrt{(N-1)}$ when averaging N measurements, while systematic error can't.

The distinction between random and systematic errors would only make sense if the time extrapolation factor can be based on traffic activity measurements and the spatial extrapolation factor can be derived from a statistically representative number of distributions on individual days. We did not use this strategy in our study because we only present a rough estimate of the uncertainty.

Anyway, Stremme et al. (2013) report an evaluation of the error due to the temporal extrapolation, using the modeled temporal distribution at various times (boxcar, triangle, trapezoid distributions and the distribution from the official inventory) and found a standard deviation (STD) of $26\% \times \text{AVG}$ and a standard error of $\approx 10\% = 26\% / \sqrt{(N-1)}$ assuming $N=8$ distributions. As the result is an average estimate of the emission and many days contribute to the estimation, the systematic error due to the temporal interpolation factor is likely much higher than the random error of the fitted growth rate.

12. Page 24, line 717: what are these instrumental and retrieval effects, just briefly? What size are these factors?

Reply: We more specifically refer to the airmass dependent effect mostly affecting the CO₂ due to spectroscopic inadequacies (e.g. line widths, neglect of line-mixing, inconsistencies in the relative strengths of weak and strong lines). This effect can affect the intraday pattern of CO₂ (Wunch et al., 2010), if the actual profile of the target gas in the atmosphere differs from the a-priori profile assumed in the retrieval. PROFFAST applies an Airmass Dependent

Correction Factor (ADCF) similar to TCCON (Deutscher et al., 2010; Wunch et al., 2010) but this effect is not yet fully resolved and can cause some imprecisions in the diurnal patterns. To give an idea of the influence of this effect we used the ADCF equation and the coefficient reported in the technical note of the COCCON website (https://www.imk-asf.kit.edu/downloads/Coccon/2021-04-30_Instrument-Calibration.pdf) corresponding to the used version of PROFFAST:

$$X_{corr_adcf}(x)/X_{uncorr_adcf} = \{1 + x^4 \cdot (b + c \cdot x^8)\} / \{1 + x_{ref}^4 \cdot (b + c \cdot x_{ref}^8)\}$$

where b and c are the ADCF coefficients. We calculate the correction for the minimum and maximum SZA compliant with our applied filters (SZA < 70). For the SZA close to zero the correction is minimum (ADCF close to 1.). The relative difference between the two results was found to be 0.18% for CO₂ (which corresponds to about 0.7 ppm) and 3.8% for CO (which corresponds to about 0.005 ppm). Therefore the correction can be significant for diurnal variability of CO₂ (< 1-2 ppm) while it can be neglected for studying CO anomalies (> 0.02 ppm). A further retrieval-associated effect one might discuss here is the non-ideal column sensitivity of the retrieval. It seems, for CO in the PBL and assuming small SZA, it is near 0.95 (so only 5% underestimation), and for CO₂ it is ~ 1.25, so ~ 25% overestimation in the retrieval.

We complement the following lines (l. 738-740) in the manuscript:

“CO₂ emissions could not be directly estimated using the same method, given its complex diurnal pattern, which is a cumulative result of both natural and anthropogenic contributions and likely been influenced by additional factors, related to instrumental and retrieval effects (i.e: air mass dependence error with a sub-percentage error for CO₂, non-ideal column sensitivity of the retrieval which represent near 25% overestimation for CO₂ anomaly and 5% underestimation for CO anomaly in the PBL.)”

13. Page 25, figure 11 caption, line 731: is that t/year or kt/year? **Done**
14. Page 27, lines 807/808: The mention of other components is presumably industrial and domestic burning as described in the next sentence? Need to link these two sentences more clearly.

Reply: We agree with the reviewer that this part was unclear and rephrased the two sentences in l. 828-836:

“The CO/CO₂ ratios calculated from the SEDEMA data for total emissions are similar to ours (0.014 and 0.011 in 2016 and 2018, respectively), suggesting that our average CO/CO₂ ratio is actually representative of the global mixing of the different sources of the MCMA, and not only dominated by the road traffic. Interestingly, according to the SEDEMA inventory, road traffic, the main anthropogenic CO source is identified by ratios (0.019 and 0.016 in 2016 and 2018, respectively) only slightly higher than our global average; whilst the industrial and domestic burning sectors, which represent the second main CO₂ anthropogenic sources, produces a one order of magnitude lower ratio. In any case, our measurements are well representative of the main source of the CO and CO₂ anthropogenic emissions”.

15. Page 28, line 837: “.. effects to the advection, ...” -> “ ..effects of advection, ..” **Done**

16. Page 29, line 861: “redaction” is not the correct term which means to remove text for publication, so “writing” is better here. **Done**

2. Response to Reviewer #2

Taquet et al. investigated the variability of CO₂ and CO in the Mexico City Metropolitan Area (MCMA) on different (annual, seasonal, and diurnal) time scales, based on ground-based in situ and remote sensing measurements. Enhancement ratios (CO/CO₂) were derived from both the in situ and remote sensing measurements and used to estimate CO₂ emissions in the MCMA by combining them with TROPOMI CO data. The estimated annual CO₂ emissions showed the reduction in 2020, likely due to the COVID-19 lockdown, which is not yet reflected in the emission inventories.

The topic of this manuscript is important and relevant to the scope of Atmospheric Chemistry and Physics. In addition, the analysis method is appropriate, and the writing structure is well organized. I recommend that this article be published after addressing the following concerns and questions.

Specific comments

Abstract: The abstract only describes what was done in this study, so please write what was revealed.

Reply: We replaced some parts of the abstract to highlight our findings:

“Accurate estimates of greenhouse gas emissions and sinks are critical for understanding the carbon cycle and identifying key drivers of anthropogenic climate change. In this study, we investigate the variability of CO and CO₂ concentrations and their ratio over the Mexico City Metropolitan Area (MCMA) from long-term time-resolved columnar measurements at three stations, using solar absorption Fourier transform infrared spectroscopy (FTIR). Using a simple model and the mixed layer height from a ceilometer, we determined the CO and CO₂ concentration in the mixed layer from the total column measurements and found good agreement with surface cavity ring-down spectroscopy measurements. In addition, we used the diurnal pattern of CO columnar measurements at specific time intervals to estimate an average growth rate that, when combined with the space-based TROPOMI CO measurements, allowed deriving annual CO and CO₂ MCMA emissions from 2016 to 2021. A decrease of more than 50% of the CO emissions was found during the COVID19 lockdown period with respect to the year 2018. These results demonstrate the feasibility of using long-term EM27/Sun column measurements to monitor the annual variability of anthropogenic CO₂ and CO emissions in Mexico City without recourse to complex transport models. This simple methodology could be adapted to other urban areas if the orography allows

low ventilation for several hours per day, which allows that column growth rate to be dominated by emission flux.”

L97: What does the “ground-based satellite produce” mean?

Reply: We thank the reviewer to detect this mistake, and replace this part by “atmospheric monitoring and satellite products validation”

L129-131: Please add latitude, longitude, and elevations of the VAL, UNA, and ALTZ stations. **Done**

Figure 1: What do the triangle and cross symbols represent?

Reply: We thank the reviewer for pointing out that the information was missing. We added the information in the legend of Figure 1 and complement the manuscript in l. 707 and l.721-722.

L179 and L210: Nation air dryer → Nafion air dryer **Done**

L276: VRM-scaling → VMR-scaling **Done**

L281: The degree of freedom for the CO retrievals in the MIR region is not expected to be as large. Do you evaluated the impact of using a single prior in the profile retrieval of CO?

The CO retrieval from the MIR measurements is a Network for Detection of Composition Change (NDACC) product (Pougatchev et al., 1994; Rinsland et al. 1998) for more than 30 years. There are typically up to 4 degrees of freedom of signal (DOFs) in the profile retrieval, with information from the bottom up to the upper stratosphere (Velasco et al. 2007, Borsdorff et al 2014). High mountain sites might have less DOFs. In Mexico City, we have a lower spectral resolution and in Alzomoni, due to the altitude above 4000 m, we also have slightly less degrees of freedom. In the NDACC retrievals, a fixed a priori is normally used, so that the measured change is coming from the measurements and not from variable a priori information. The “block constraint”, as described by v.Clarmann and Grabowsky, (2007) ensures that the growth rate in the mixing layer is not damped and the impact of the free troposphere to the column in the mixed layer is very small. It is important to use a single apriori, to be sure that the column growth rate is a result of the measurement and not introduced by a variable a-priori information.

We added the citations in l. 285: “(Pougatchev et al., 1994; Rinsland et al. 1998)”

L419: The description of Figure 4 in the text precedes Figure 3. Please swap the order of Figures 3 and 4. **Done**

Figure 3: Figures 3C and 3D are not explained in the text. Please add their explanations or omit these figures. **Done:** We added references of these figures in the text in l. 481, 482, 484 and 499.

L479-480: To understand what is described in this sentence, which figure should readers refer to? **Done: We cite the figure 4C in this sentence.**

Figure 5: What factors contribute to the difference in the diurnal patterns in ΔXCO_2 between the UNA and VAL sites? Can this difference be explained by differences in the spatiotemporal patterns of wind direction within the MCMA?

We really appreciate the commentary of the reviewer and detail below the possible reasons which can explain this difference.

In our manuscript, the XCO and XCO₂ diurnal patterns were calculated after discarding days with high ventilation, based on ERA5 data. Figure S6 shows wind rose diagrams characterizing the surface wind (at 10 m) measured by the local UNA and VAL meteorological stations using the RUOA and REDMET networks, after selecting the data which comply with the Ventilation Index filter.

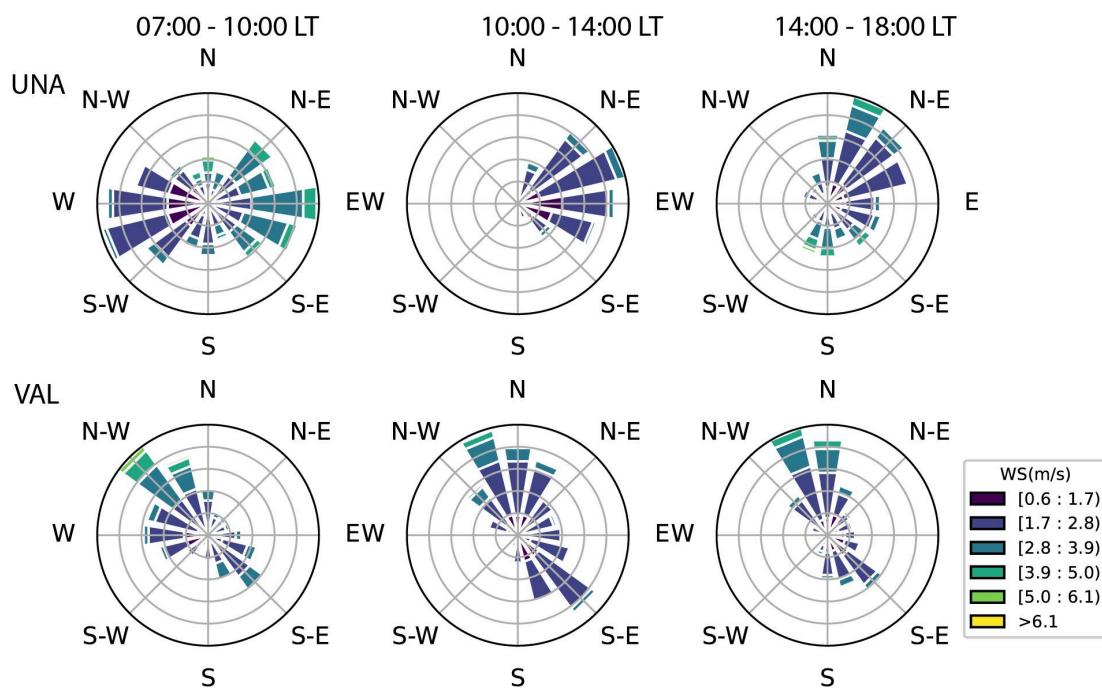


Figure S6: Dominant surface wind speed and direction at the UNA and VAL stations (average over 01/09/2019-01/06/2021) calculated from the REDMET(VAL) and RUOA (UNA) meteorological stations, selecting days complying with the VI filter described in the manuscript.

Figure S6 shows a dominant average surface wind direction over the Mexico valley from the North, at least after 10 LT. However, a real difference appears in terms of spatio-temporal variability at the scale of the MCMA. While the wind rose diagram for the UNA station shows an important disparity in surface wind direction and a significant intraday variability, the VAL station shows a very constant wind direction all day long, which mainly coincide with the CO distribution observed from the Tropomi data in Figure 1 of the manuscript. The wind direction and advection of the air mass near the VAL station are likely mainly controlled by the topographic barriers of the region

see topography in the new version of Figure 1), which can explain the gradient in the CO distribution upwind of the VAL station. The air mass measured at the VAL station likely has a contribution of both local sources emissions and air mass coming from the north. In contrast, near the UNA station, the flat ground allows a more efficient mixing and due to the dominant North-NorthEast wind component, the captured air mass likely often reflects the MCMA plume emissions. In addition the West-Northwest wind component at UNA is likely to be the effect of down-slope flows from the mountain ridge in the early morning (6 - 9 LT). At VAL, the plateau-to-basin winds are the main influx into the basin coming from the northwest in the morning. There can also be an influence from an up-valley flow in the mornings (de Foy et al., 2006). These observations are supported by the carbon monoxide distribution over the MCMA from Tropomi, shown in Figure 1 of the manuscript. The gradients in the total columns of carbon monoxide shown by Tropomi (Figure 1) are different near the VAL and UNA stations, and even the same global ventilation pattern would impact both sites differently. Especially the stronger gradient in the typical upwind direction will lead to a high variability at VAL. Only at UNAM the area is homogenous enough, so that we can assume that the ventilation plays a minor role during morning and up to noon.

We modified Figure 1 to highlight the topography of the region. We added the figure S6 in the supplementary data and added the following lines in the manuscript l. 584-594:

“The difference observed between the diurnal pattern of the XCO and XCO₂ at VAL and UNA is likely due to the different advection drivers in the region mainly controlled by the topography. A Northern surface wind direction (Figure S6) is generally dominating over the Mexican valley but is locally highly influenced by the mountainous barriers. The West-northwest wind component at UNA is likely to be the effect of down-slope flows from the mountain ridge in the early morning (6 – 9 LT mostly), while at VAL, the plateau-to-basin winds are the main influx into the basin coming from the northwest in the morning. There can also be an influence from an up-valley flow in the mornings (de Foy et al., 2006). More generally the VAL station is likely influenced by the north mountain, generating a significant gradient in the CO distribution upwind of the VAL station (Figure 1). In contrast, near the UNA station, the flat ground allows a more efficient mixing and due to the dominant North-Northeast wind component in the late morning, the captured air masses likely often reflects the MCMA plume emissions.”

and at l.864: “The same strategy could not be applied at the VAL station, likely because of dominant southward advection of the air mass, due to the complex topography in this part of the MCMA. In contrast, the UNA station is located in a flat ground downwind of the main anthropogenic source of the MCMA which likely allows establishing a direct relationship between the columnar measurements and the MCMA CO and CO₂ emissions.”

L529 and L798: Please define the “MGRA”. We thank the reviewer for the types here and replace “MGRA” by “MAGR”

L530: What does the “ELD” represent? Please add the explanation.

Reply: We added some explanation in lines 533-536: “To explore the 2020 lock-down influence on the diurnal pattern, three different periods were distinguished for each plot, the first one (blue trace: 2016 - 2021) corresponding to the whole measurement period excluding the interval between March and June 2020 corresponding to the lock-down period (hereafter, called “ELD” for “excluding the lock down period”), where a significant MAGR decrease was observed;”

Figures 7A and 7B: Are the “Surface” and “From FTIR Tot.col.” legends reversed?

Reply: We thank the reviewer for pointing out this mistake and modified the legend.

L648: Fig. 9 instead of Fig. 7?

Reply: We thank the reviewer for pointing out this mistake and replaced “Fig.7” by “Fig. 9”.

L683: Over what domain is $(CO_{MCMA} - CO_{bgrd})$ integrated? Area?

Reply: We added in l. 703: “In Eq. (8), $(CO_{MCMA} - CO_{bgrd})$ is integrated over the area where the CO TROPOMI total columns are higher than a predefined background value.” The way to define the background value is explained in the following sentences.

L694: What does the “mixed layer column” mean and how is it defined?

Reply: We thank the reviewer for pointing out this unclear point and we replaced the sentence at l. 714: “The mixed layer column at UNA from the TROPOMI data was found to be 1.93×10^{18} molec.cm⁻² (Fig. 1), which is consistent with our EM27/SUN ground-based measurements (average of 2.17×10^{18} molec.cm⁻²)” with:

“The fresh CO was estimated from the TROPOMI data by removing the background (1.45×10^{18} molec.cm⁻²) to the average total columns found at UNA (1.93×10^{18} molec.cm⁻²) and was found to be 4.79×10^{17} molec.cm⁻².”

L717: The factors related to instrumental and retrieval effects would also affect the CO columns. How do these factors affect the CO emission estimates?

Reply: We more specifically refer to the airmass dependent effect mostly affecting the CO₂ due to spectroscopic inadequacies (e.g. line widths, neglect of line-mixing, inconsistencies in the relative strengths of weak and strong lines). This effect can affect the intraday pattern of CO₂ (Wunch et al., 2010), if the actual profile of the target gas in the atmosphere differs from the a-priori profile assumed in the retrieval. PROFFAST applies an Airmass Dependent Correction Factor (ADCF) similar to TCCON (Deutscher et al., 2010; Wunch et al., 2010) but this effect is not yet fully resolved and can cause some imprecisions in the diurnal patterns. To give an idea of the influence of this effect we used the ADCF equation and the coefficient reported in the technical note of the COCCON website (https://www.imk-asf.kit.edu/downloads/Coccon/2021-04-30_Instrument-Calibration.pdf) corresponding to the used version of PROFFAST:

$$X_{corr_adcf}(x)/X_{uncorr_adcf} = \{1 + x^4 \cdot (b + c \cdot x^8)\} / \{1 + x_{ref}^4 \cdot (b + c \cdot x_{ref}^8)\}$$

where b and c are the ACDF coefficients.

We calculate the correction for the minimum and maximum SZA compliant with our applied filters ($SZA < 70$). For the SZA close to zero the correction is minimum (ADCF close to 1.). The relative difference between the two results was found to be 0.18% for CO_2 (which corresponds to about 0.7 ppm) and 3.8% for CO (which corresponds to about 0.005ppm). Therefore the correction can be significant for diurnal variability of CO_2 (<1-2 ppm) while it can be neglected for studying CO anomalies (>0.02ppm). A further retrieval-associated effect one might discuss here is the non-ideal column sensitivity of the retrieval. It seems, for CO in the PBL and assuming small SZA, it is near 0.95 (so only 5% underestimation), and for CO_2 it is ~ 1.25 , so $\sim 25\%$ overestimation in the retrieval.

We complement the following lines (l. 738-740) in the manuscript:

“ CO_2 emissions could not be directly estimated using the same method, given its complex diurnal pattern, which is a cumulative result of both natural and anthropogenic contributions and likely been influenced by additional factors, related to instrumental and retrieval effects (i.e: air mass dependence error with a sub-percentage error for CO_2 , non-ideal column sensitivity of the retrieval which represent near 25% overestimation for CO_2 and 5% underestimation for CO in the PBL)”.

L758: Please define the “GRA”. We replace “GRA” with “AGR”.

Supplementary file

Caption of Figure S2: after applying the calibration factors → after applying the calibration factors **Done**

Table S1: Are the digits of the calibration factor of “VERTEX-XCO MIR” insufficient? **We added 2 additional digits for the calibration factor.**

Caption of Table S3: *corresponds → The asterisks (*) correspond **Done**

References

Borsdorff, T. and Sussmann, R.: On seasonality of strato-mesospheric CO above midlatitudes: New insight from solar FTIR spectrometry at Zugspitze and Garmisch, Geophys. Res. Lett.,36, L21804, doi:10.1029/2009GL040056, 2009. 5001, 5013, 5014

Che, K., Lauvaux, T., Taquet, N., Stremme, W., Xu, Y., Alberti, C., Lopez, M., García-Reynoso, A., Ciais, P., Liu, Y., Ramonet, M., Grutter, M. (2024). CO_2 emissions estimate from Mexico City using ground- and space-based remote sensing. submitted to Journal of Geophysical Research.

Chen, J., Viatte, C., Hedelius, J. K., Jones, T., Franklin, J. E., Parker, H., Gottlieb, E. W., Wennberg, P. O., Dubey, M. K., and Wofsy, S. C.: Differential column measurements using compact solar-tracking spectrometers, *Atmos. Chem. Phys.*, 16, 8479–8498, <https://doi.org/10.5194/acp-16-8479-2016>, 2016.

de Foy, B., Varela, J. R., Molina, L. T., and Molina, M. J.: Rapid ventilation of the Mexico City basin and regional fate of the urban plume, *Atmos. Chem. Phys.*, 6, 2321–2335, <https://doi.org/10.5194/acp-6-2321-2006>, 2006.

Frey, M. M.: Characterisation and application of portable solar absorption spectrometers for the detection of greenhouse gas emissions from regional anthropogenic sources, PhD thesis, Karlsruher Institut für Technologie (KIT), <https://doi.org/10.5445/IR/1000088312>, 2018. a, b, c

Hase, F., Frey, M., Blumenstock, T., Groß, J., Kiel, M., Kohlhepp, R., Mengistu Tsidu, G., Schäfer, K., Sha, M. K., and Orphal, J.: Application of portable FTIR spectrometers for detecting greenhouse gas emissions of the major city Berlin, *Atmos. Meas. Tech.*, 8, 3059–3068, <https://doi.org/10.5194/amt-8-3059-2015>, 2015.

García-Franco, J. L. (2020). Air quality in Mexico City during the fuel shortage of January 2019. *Atmospheric environment*, 222, 117131.

Hernández-Paniagua, I. Y., Valdez, S. I., Almanza, V., Rivera-Cárdenas, C., Grutter, M., Stremme, W., García Reynoso, A., Ruiz-Suárez, L. G. (2021). Impact of the COVID-19 lockdown on air quality and resulting public health benefits in the Mexico City metropolitan area. *Frontiers in public health*, 9, 642630.

González Del Castillo, E., Taquet, N., Bezanilla, A., Stremme, W., Ramonet, M., Laurent, O., Xu, Y., Delmotte, M., Grutter, M.: CO₂ variability in the Mexico City region from in situ measurements at an urban and a background site, *Atm.*, 35, 377–393, <https://doi.org/10.20937/ATM.52956>, 2022.

Hernández-Paniagua, I. Y., Valdez, S. I., Almanza, V., Rivera-Cárdenas, C., Grutter, M., Stremme, W., García Reynoso, A., Ruiz-Suárez, L. G. (2021). Impact of the COVID-19 lockdown on air quality and resulting public health benefits in the Mexico City metropolitan area. *Frontiers in public health*, 9, 642630, doi:<https://doi.org/10.3389/fpubh.2021.642630>

Liñán-Abanto, R. N., Salcedo, D., Arnott, P., Paredes-Miranda, G., Grutter, M., Peralta, O., Carabali, G., Serrano-Silva, N., Ruiz-Suárez, L. G., Castro, T. (2021). Temporal variations of black carbon, carbon monoxide, and carbon dioxide in Mexico City: Mutual correlations and evaluation of emissions inventories. *Urban Climate*, 37, 100855. <https://doi.org/10.1016/j.uclim.2021.100855>

Molina, L. T. (2021). Introductory lecture: air quality in megacities. *Faraday discussions*, 226, 9-52.

Pommier, M., McLinden, C. A., & Deeter, M. (2013). Relative changes in CO emissions over megacities based on observations from space. *Geophysical research letters*, 40(14), 3766-3771.

Porras, S., González del Castillo, M.E., López, O., Arredondo, T., Rivera, O., Ramonet, M., Laurent, O.,

Grutter, M.: Diseño y despliegue de una red piloto para la medición de CO₂ con un sistema de microsensores, UNAM internal report, 2023: http://www.epr.atmosfera.unam.mx/Microsensores-2022/documentos/4_Red_piloto_CO2.pdf (last accessed on May 20, 2024)

Pougatchev et al., Ground-based infrared solar spectroscopic measurements of carbon monoxide during 1994 Measurement of Air Pollution From Space flights, JOURNAL OF GEOPHYSICAL RESEARCH, VOL. 103, NO. D15, PAGES 19,317-19,325, AUGUST 20, 1998

Rinsland, C. P., et al. (1998), Northern and southern hemisphere ground-based infrared spectroscopic measurements of tropospheric carbon monoxide and ethane, *J. Geophys. Res.*, 103(D21), 28197–28217, doi:[10.1029/98JD02515](https://doi.org/10.1029/98JD02515).

Tu, Q., Schneider, M., Hase, F., Khosrawi, F., Ertl, B., Necki, J., Dubravica, D., Diekmann, C. J., Blumenstock, T., and Fang, D.: Quantifying CH₄ emissions in hard coal mines from TROPOMI and IASI observations using the wind-assigned anomaly method, *Atmos. Chem. Phys.*, 22, 9747–9765, <https://doi.org/10.5194/acp-22-9747-2022>, 2022b.

Velazco, V., Wood, S.W., Sinnhuber, M., Kramer, I., Jones, N.B., Kasai, Y., Notholt, J., Warneke, T., Blumenstock, T., Hase, F. and Murcray, F.J., 2007. Annual variation of strato-mesospheric carbon monoxide measured by ground-based Fourier transform infrared spectrometry. *Atmospheric chemistry and physics*, 7(5), pp.1305-1312.

von Clarmann, T. and Grabowski, U.: Elimination of hidden a priori information from remotely sensed profile data, *Atmos. Chem. Phys.*, 7, 397–408, doi:10.5194/acp-7-397-2007, 2007.

CO₂ and CO temporal variability over Mexico City from ground-based total column and surface measurements

Noémie Taquet¹, Wolfgang Stremme¹, María Eugenia González del Castillo¹, Victor Almanza¹, Alejandro Bezanilla¹, Olivier Laurent², Carlos Alberti³, Frank Hase³, Michel Ramonet², Thomas Lauvaux⁴, Ke Che⁴, Michel Grutter¹

¹Instituto de Ciencias de la Atmósfera y Cambio Climático, Universidad Nacional Autónoma de México, México

²Laboratoire des Sciences du Climat et de l'Environnement (LSCE), IPSL, CEA-CNRS-UVSQ, Université Paris-Saclay, Gif-sur-Yvette, France

³Institute of Meteorology and Climate Research (IMK-ASF), Karlsruhe Institute of Technology (KIT), Karlsruhe, Germany

⁴Groupe de Spectrométrie Moléculaire et Atmosphérique (GSMA), Université de Reims-Champagne Ardenne, UMR CNRS 7331, Reims, France

Correspondence to: Noémie Taquet (noemi.taquet@gmail.com)

Abstract.

Accurate estimates of greenhouse gas emissions and sinks are critical for understanding the carbon cycle and identifying key drivers of anthropogenic climate change. In this study, we investigate the variability of CO and CO₂ concentrations and their ratio over the Mexico City Metropolitan Area (MCMA) from long-term time-resolved columnar measurements at three stations, using solar absorption Fourier transform infrared spectroscopy (FTIR). Using a simple model and the mixed layer height from a ceilometer, we determined the CO and CO₂ concentration in the mixed layer from the total column measurements and found good agreement with surface cavity ring-down spectroscopy measurements. In addition, we used the diurnal pattern of CO columnar measurements at specific time intervals to estimate an average growth rate that, when combined with the space-based TROPOMI CO measurements, allowed deriving annual CO and CO₂ MCMA emissions from 2016 to 2021. A decrease of more than 50% of the CO emissions was found during the COVID19 lockdown period with respect to the year 2018. These results demonstrate the feasibility of using long-term EM27/Sun column measurements to monitor the annual variability of anthropogenic CO₂ and CO emissions in Mexico City without recourse to complex transport models. This simple methodology could be adapted to other urban areas if the orography favours low ventilation for several hours per day, which allows that column growth rate to be dominated by emission flux.

1 Introduction

The greenhouse gas (GHG) mitigation strategies implemented in megacities following the 1997 Kyoto Protocol and the 2015 Paris Agreement play a crucial role in the global action plan to mitigate climate change, given that cities are accountable for more than 70% of the global anthropogenic emissions (Duren and Miller, 2012). With the recent progress in space-based and ground-based remote GHG measurements in terms of accuracy, spatial coverage/resolution and temporal frequency, GHG emissions can increasingly be constrained by comparing bottom-up and top-down estimates. Top-down approaches are generally based on ground or space-based atmospheric measurements coupled with inverse modelling, using 3D-Eulerian (i.e: WRF-Chem) or Lagrangian and hybrid (i.e: STILT, Hysplit) approaches (Wu et al., 2018, Che et al., 2022; Lian et al., 2023). The quantification of anthropogenic CO₂ enhancements from cities using satellite data e.g: GOSAT (Wang et al., 2019), OCO-2 (Ye

45 et al., 2020) or TanSat (Liu et al., 2018) is still challenging due to the sparsity of the observations, the low signal
46 from the anthropogenic contribution compared to the background levels and biogenic contribution, and some
47 inconveniences inherent to space-measurements such as the non-negligible aerosol effects (Wang et al., 2020 and
48 references therein). Some studies have estimated the urban enhancements of anthropogenic CO₂ concentrations
49 along with CO and NO₂ from satellite measurements, as these air pollutants can serve as tracers of anthropogenic
50 CO₂ (Silva et al., 2013; Park et al., 2021 and references therein). The CO/CO₂ ratio is often used to determine the
51 combustion efficiency of the cities (Park et al., 2021 and references therein). With the development of a new
52 generation of space-based observatories, such as Sentinel-5P and OCO-2,3, the evolution of GHGs at the city scale
53 can now be characterised with a finer temporal and spatial resolution (Kiel et al., 2021) but more validation efforts
54 are needed. As inverse modelling is likely undermined by the approximations used for defining the emission
55 patterns, transport processes and meteorology, top-down approaches may lead to discrepancies in emissions
56 estimates, in particular in sites with complex orography.

57 Ground-based total column FTIR instruments provide valuable long-time concentration measurements of
58 GHG and pollutant reactive species, as well as anthropogenic tracers, constituting a key element to validate
59 regional and local inventories. Some studies reported estimates of CO₂ and CH₄ emissions from large urban areas
60 (Babenhauserheide et al., 2018 in Tokyo; Hedelius et al., 2018 in the California Southern Coast Air Basin
61 California megacity), using data from high-resolution FTIR instruments (i.e: Bruker IFS120/5HR) contributing to
62 the Total Column Carbon Observing Network (TCCON). Nevertheless, only a few TCCON stations are located in
63 urban areas (Toon et al., 2009; Chevallier et al., 2011; Sussman et al., 2020). The development of the Collaborative
64 Carbon Column Observing Network (COCCON, Frey et al., 2019), using a new generation of portable low spectral
65 resolution FTIR spectrometers (EM27/SUN, Gisi et al., 2012; Hase et al., 2016) able to simultaneously measure
66 the CO₂, CO, H₂O and CH₄ average total columns with a similar quality as TCCON, has considerably densified
67 the number of measurements in urban environments. Some studies reported emission estimates for big cities by
68 means of the deployment of several EM27/SUN instruments at strategic sites throughout the cities (Hase et al.,
69 2015 and Zhao et al., 2019 in Berlin; Vogel et al., 2019 in Paris; Makarova et al., 2021 in St Petersburg; Zhou et
70 al., 2022 in Beijing and Xianghe; Che et al. 2022, in Beijing; Rißmann et al., 2022 for Munich) coupling
71 measurements with inverse modelling. Most of these studies were based on short-term campaign observations,
72 applying the Differential Column Methodology (DCM, Chen et al., 2016) or dedicated dispersion models (Hase
73 et al., 2016), coupled with simple mass balance-based methods or inverse modelling to derive emissions. Most of
74 these studies reported significant discrepancies between the estimates, depending on the models used (Viatte et
75 al., 2017).

76 In this study, we aimed to determine the Mexico City Metropolitan Area (MCMA) CO₂ and CO emissions
77 using ground-based FTIR and surface measurements, without resorting to complex dispersion and/or chemistry
78 transport models. The MCMA, with a population around 22 million inhabitants, is in the top ten most populous
79 cities in the world and ranks among the major emitters of GHGs in North America. The available information of
80 GHGs emission estimates are mainly based on the inventories reported by the Ministry of the Environment of
81 Mexico City (SEDEMA), which is updated every two years, but lagging several years behind. In the report based
82 on 2018, the latest published before the COVID19-lock-down (2020), a total emission of 75.2 Mt CO₂-eq is
83 estimated for the MCMA, 87% of which is attributed to fossil fuel combustion and 58% originates from the
84 transport sector (SEDEMA Inventory, 2018). The Mexico City government is actively engaged in the C40 Climate

85 Change Program and implemented significant policy measures since 2008, including promoting sustainable
86 transportation systems, implementing energy efficiency measures, increasing the use of renewable energy sources,
87 and adopting green building practices. On a national scale, the country is committed to reduce its GHGs emissions
88 by 35% by 2030 with respect to its base level, as stated in the last Nationally Determined Contributions report
89 (NDC-2022, UNFCCC). To assess the effect of the national and local mitigation policies, the installation of
90 ground-based GHG measurement networks and the refinement of bottom-up estimates by comparing them with
91 the top-down method (i.e: inverse modelling) is of critical importance to obtain a comprehensive GHGs database
92 that can serve as follow-up of the mitigation actions.

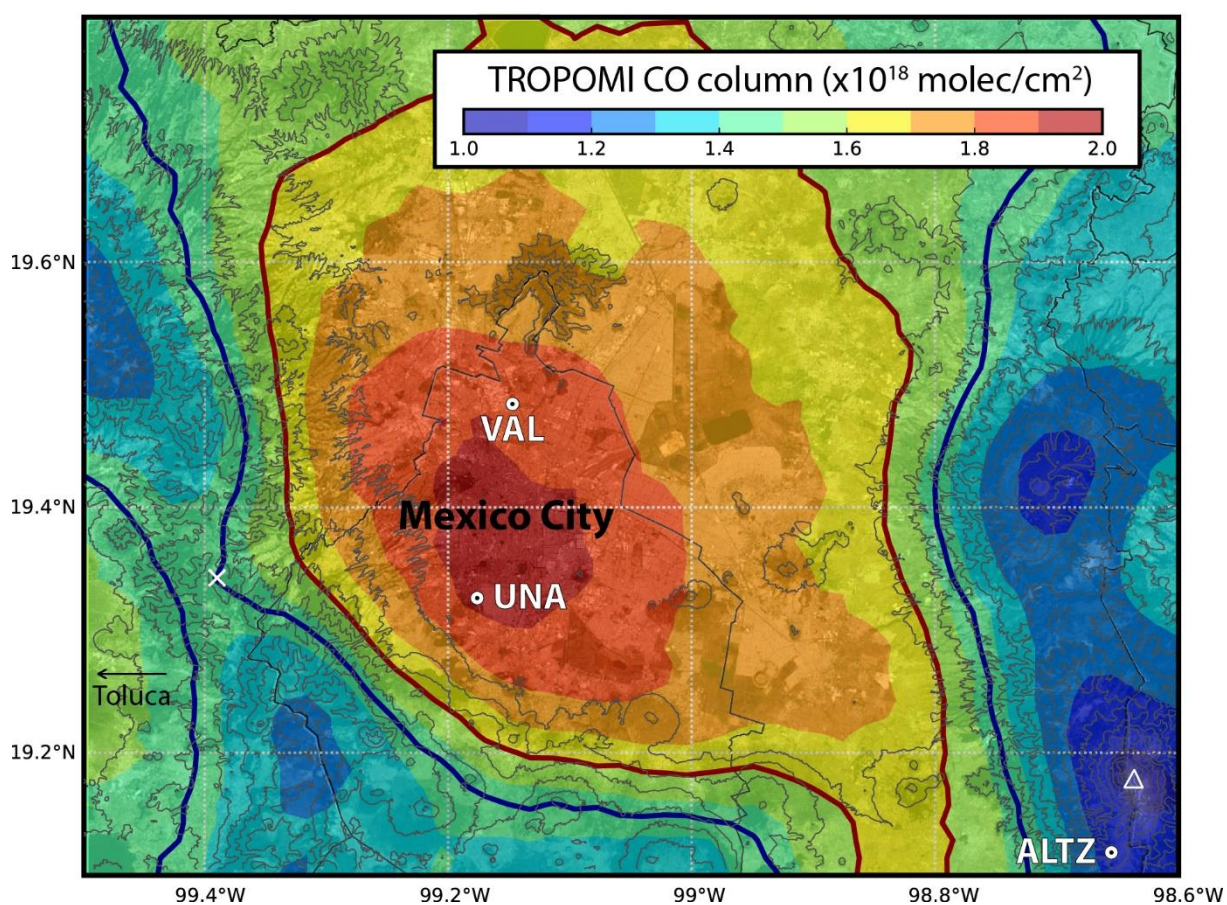
93 The Institute of Atmospheric Sciences and Climate Change (ICAyCC, Spanish acronym) at UNAM
94 (Universidad Nacional Autónoma de México) deployed in the last decade a wide range of surface gas sensors and
95 ground-based remote sensing instruments across the MCMA (Grutter, et al., 2003; Molina et al., 2010; Bezanilla
96 et al., 2014; Stremme et al., 2009; 2013; Baylon et al., 2017) in the frame of research projects related to air quality
97 assessment, **atmospheric monitoring and satellite products validation**. Since 2013, UNAM has contributed to the
98 Network for the Detection of Atmospheric Composition Change (NDACC), performing continuous composition
99 measurements of the free troposphere from the high altitude Altzomoni Atmospheric Observatory (ALTZ) station,
100 located 60 km southeast of Mexico City at 3985 m a.s.l. Baylon et al., (2017) reported the background CO₂
101 variability and trend from this station between 2013 and 2016. Stremme et al., (2013) reported the first top-down
102 estimate of carbon monoxide (CO) emissions for the MCMA, based on FTIR CO total column measurements and
103 the Infrared Atmospheric Sounding Interferometer (IASI) data. These authors derived the CO₂ emissions for the
104 MCMA using the CO emission estimates and the average CO/CO₂ ratio reported in Grutter (2003), using FTIR
105 measurements. In 2018, the Mexican/French “Mexico City’s Regional Carbon Impacts (MERCICO2)” project
106 (coordinated by UNAM and LSCE) was launched aiming to assess the CO₂ emissions from MCMA using
107 EM27/SUN measurements and inverse modelling to evaluate the effectiveness of the mitigation strategies
108 implemented by the local authorities. Xu et al., (submitted) examined the performance of a modelling system based
109 on WRF-Chem to assess the whole-city emissions using the EM27/SUN measurements deployed in the frame of
110 the MERCICO2 project. The complex orography of the region posed a challenge in the atmospheric transport
111 simulations and thus for the top-down estimates using inverse modelling. Indeed, Mexico City is situated in a high
112 altitude basin (~2300 m. a.s.l.), surrounded by mountains reaching up to 5.6 km a.s.l., and is prone to accumulate
113 anthropogenic emissions, especially during the dry season, when the atmospheric boundary layer ventilation is
114 limited (Burgos-Cuevas et al., 2023). The boundary layer dynamics in the basin and the wind surface circulation
115 is complex, due to the temperature contrasts and rough topography.

116 In this study, we report the long-term (2013-2021) variability of the CO₂ and CO total columns and
117 surface concentrations (from 2014) above the MCMA using long-term ground-based FTIR and surface Cavity
118 Ring-Down Spectroscopic (CRDS) measurements. Using the mixed layer height data from the continuous
119 ceilometer measurements at UNAM, we examined the consistency of the surface and total column measurements
120 of our network. We also determined an average CO/CO₂ ratio based on FTIR and surface measurements at different
121 temporal resolutions (from daily to intraday). Then, using the spatial distribution of TROPOMI CO column
122 measurements, we explore the potential of our FTIR network to capture the variability of the megacity CO and

123 CO₂ emissions using a simplified model, i.e.: without recourse to complex numerical simulations. Our estimates
 124 are compared with the available bottom-up and previous top-down estimates.

125 2 Sites, instrumentation and measurement protocols

126 We used in this study the column-averaged dry-air mole fractions of CO₂ and CO (XCO₂ and XCO) from
 127 three permanent FTIR stations distributed in a radius of 100 km around MCMA (Fig. 1), and the surface
 128 measurements performed at UNA and ALTZ sites. The measurement periods for the different instruments at each
 129 site are reported in Table 1. The VAL station is located at the northern part of the city in a highly industrialised
 130 zone. The UNA station is situated at the south of the city in the main campus of UNAM. The third station is the
 131 ALTZ background site (3985 m a.s.l.), located 60 km ESE from UNAM, within the Izta-Popo National Park. The
 132 equipment of the different stations and measurement protocols are described in the following sub-sections.



133 **Figure 1: Map of the ALTZ, UNA and VAL stations and average distribution (2018-2022) of carbon monoxide total**
 134 **columns over the Mexico City Metropolitan Area (MCMA) calculated from the TROPOMI CO product. Red and blue**
 135 **contour lines represent the inner and outer area used to calculate the effective area (see details in text). The cross symbol**
 136 **indicate the smallest CO total column value observed upwind the city at the elevation of the Mexican basin, which is**
 137 **used to estimate the background. The average total column can be decomposed into two main contributors: i) a**
 138 **background of around 1.45×10^{18} molec.cm⁻² (limits represented by blue contour lines) and ii) the local influence**
 139 **corresponding to the carbon monoxide emitted on the same day. The total columns are highly influenced by the**
 140 **topography which is clearly visible over the highest terrains of the region, near to the Popocatepétl and Iztaccíhuatl**
 141 **volcanoes at the south east of Mexico City. The mountains of Ajusco are located southwest of Mexico City. The**
 142 **enhancement in the center of the metropolitan area reflects the carbon monoxide locally emitted on the same day.**

144

145

146 **Table1: Instrumentation and measurement periods used in this study.**

Station	Instrument	Measurement period	Product
ALTZ (19.119°N, 98.655°W 3.99 km a.s.l.)	IFS120/5HR	01/01/2013 - 01/06/2021	XCO and XCO ₂
	EM27/SUN #038	21/10/2020 - 20/12/2020 & 10/02/2021 - 22/02/2021	XCO and XCO ₂
	EM27/SUN #104	07/02/2020 - 18/02/2020	XCO and XCO ₂
	CRDS G2401 Picarro	15/11/2015 - 01/06/2021	Surface CO and CO ₂
UNA (19.326°N, 99.176°W 2.28 km a.s.l.)	Vertex	15/11/2015 - 20/06/2017	XCO
	EM27/SUN #038	07/05/2021 - 25/05/2021	XCO and XCO ₂
	EM27/SUN #062	17/03/2016 - 01/06/2017	XCO ₂
	EM27/SUN #104	01/06/2017 - 01/06/2021 04/04/2019 - 19/09/2019	XCO and XCO ₂ XCO and XCO ₂
	CDRS G2401 Picarro	15/11/2015 - 01/06/2021	Surface CO and CO ₂
CL31 Vaisala ceilometer	15/11/2015 - 01/06/2021	Mixed Layer Height	
VAL (19.484°N, 99.147°W 2.26 km a.s.l.)	EM27/SUN #104	23/09/2019 - 01/06/2021	XCO and XCO ₂

147

148 **2.1 The UNA station: Total columns, surface concentrations and mixed-layer height measurements**

149 Atmospheric total columns of several gas species, such as O₃, NH₃, CH₄, CO, and HCHO have
150 continuously been measured at UNA since 2010 (Bezanilla et al., 2014; Plaza-medina et al., 2017; Baylon et al.,
151 2017; Rivera-Cardenas et al., 2021; Herrera et al., 2022) using solar absorption FTIR spectroscopy.

152 Measurements are performed in the mid-infrared (MIR) and near-infrared (NIR) spectral ranges using a Bruker
153 model Vertex 80 spectrometer. The instrument has a Maximum optical Path Difference (MPD) of 12 cm
154 (corresponding to a spectral resolution of 0.075 cm⁻¹) and is equipped with two detectors, a liquid-nitrogen cooled
155 mercury-cadmium-telluride (MCT) and InGaAs detectors. Solar absorption measurements are performed using a
156 home-built solar tracker. A full description of the instrumental set-up and measurement protocols is given in
157 Bezanilla et al. (2014) and Plaza-Medina et al. (2017). The CO measurements are routinely performed in the MIR
158 spectral range with a spectral resolution of 0.1 cm⁻¹, using the MCT detector.

159 In March 2016, an EM27/SUN spectrometer was implemented at UNA to continuously measure XCO₂,
160 XCH₄, XH₂O, XCO total columns from solar NIR spectra with a spectral-resolution of 0.5 cm⁻¹ (MPD of 1.8 cm).
161 The spectrometer is equipped with its own solar tracker (Bruker CAMTracker; Gisi et al., 2011) capturing and
162 redirecting the solar beam into a RockSolid™ pendulum interferometer equipped with a Quartz beamsplitter. The
163 EM27/SUN, with serial number #62 installed at the UNA station (hereafter EM27-SUN_62), was initially operated
164 with a standard InGaAs-diode detector sensitive to the 5500-11000 cm⁻¹ spectral range, to which a second InGaAs
165 detector with Ge filter was added in 2017 for CO measurements through a second channel (4000 – 5500 cm⁻¹)
166 (Hase et al., 2016). Further details on the technical characteristics and systematic performance evaluation of the
167 EM27/SUN spectrometer are given in Frey et al., (2019) and Alberti et al., (2022). The spectrometer was installed
168 in a home-made protective box, including a remotely-controlled dome cover, a GPS and a PCE-THB-40 data-

169 logger for precise timing and surface pressure measurements. Double sided forward-backward interferograms are
170 routinely recorded with a scanner velocity of 10 kHz, so that the recording time of one measurement (averaging
171 10 IFGs scans) is close to one minute.

172 Additionally, CO₂, CO, CH₄ and H₂O surface measurements are continuously performed at the UNA
173 station using a Cavity Ring-Down Spectrometer (CRDS, model G2401 from Picarro Inc.). The CRDS spectrometer
174 uses a laser to quantify the spectral features of gas-phase molecules in an optical cavity offering effectively of up
175 to 20 km absorption path length. Frequency shifts are prevented with a high-precision-wavelength monitor and
176 temperature and pressure are precisely controlled by the analyzer. The quantification is improved by the
177 simultaneous spectral analysis of the measured gases. A calibration system using 3 gas standards provided by the
178 National Oceanic and Atmospheric Administration Earth System Research Laboratory (NOAA ESRL), traceable
179 to the WMO2007 scale, was set up in 2018 at UNA and in 2019 at ALTZ. Data collected before the installation of
180 the calibration systems were corrected with calibration coefficients obtained in 2018. The sampling inlet using
181 Synflex tubing was placed at 24 m a.g.l. at UNA station and includes a Nafion air dryer, as described in detail by
182 González del Castillo et al. (2022). Data are continuously collected at 0.3 Hz rate and their uncertainties, calculated
183 as the standard deviation of raw data over 1-minute intervals when measuring calibration gases, are equal to 0.03
184 ppm at UNA (González del Castillo et al., 2022).

185

186 Finally, continuous mixed-layer height (MLH) measurements are performed since 2008 at UNA using a
187 CL31 ceilometer instrument (Vaisala). This is a robust commercial instrument which emits light pulses at 10 kHz
188 repeating frequency at 910 nm using an indium-gallium-arsenide diode laser. It detects the backscatters signal
189 through a single lens with a silicon avalanche photodiode. The resulting backscattering profiles have a vertical
190 resolution of 10 m and reach an altitude of 7,500 m. The profiles have been used to retrieve MLH above the city
191 since 2011 (García-Franco et al., 2018).

192 **2.2 The ALTZ background station: Total columns and surface measurements**

193 The Altzomoni Atmospheric Observatory (ALTZ) was equipped with a high-resolution FTIR
194 spectrometer (model IFS120/5HR, Bruker) in 2012, capable of measuring atmospheric spectra in the NIR and MIR
195 spectral regions with 257 cm MPD, equivalent to a spectral resolution of 0.0035 cm⁻¹. The instrument is installed
196 into a container with a motorised dome cover on the roof and a microwave communication system (60 km line-of-
197 sight to the university campus), which allows a fully-remote control of the instruments. When the dome is open, a
198 solar tracker (CAMTracker; Gisi et al., 2012) collects the solar beam and orients it toward the spectrometer
199 entrance. The spectrometer can be operated with KBr or CaF₂ beam splitters, 3 different detectors (MCT, InSb,
200 and InGaAs) and a set of 7 optical filters is installed in a rotating wheel. The measurement routine consists in the
201 acquisition of high (0.005 cm⁻¹), medium (0.02 cm⁻¹ and 0.1 cm⁻¹) and low (0.5 cm⁻¹) resolution spectra in the NIR
202 and MIR spectral ranges using the different NDACC filters (~40 min for a complete sequence).

203 The NIR CO and CO₂ spectra (0.02 cm⁻¹) used in this study were recorded as the average of two scans
204 taken for approximately 38 s with a scanner speed of 40 kHz. The MIR CO spectra (0.005 cm⁻¹) are deduced from
205 the coaddition of 6 scans (<200 s) with a scanner speed of 40 kHz. Due to a spectrometer laser replacement, the
206 IFS120/5HR measurements were interrupted between November 2020 and February 2021 (Table 1). To avoid an
207 important gap in the measurements, an EM27/SUN (EM27/SUN_38) was temporarily installed at the station

208 during this period. The intercalibration factors used for combining the two types of measurements were determined
 209 from previous side-by-side measurements performed during February 2021 (see Table S1 and section 3.1.3).

210 A CRDS (model G2401 from Picarro Inc.) instrument was implemented at the station in 2014 providing
 211 continuous CO₂, CO, CH₄ and H₂O surface measurements (González del Castillo et al., 2022). The sampling inlet
 212 using Synflex tubing was placed at 4 m a.g.l. and includes a Nafion air dryer (similar installation to UNA). A
 213 calibration system similar to that implemented at UNA, using 3 NOAA ESRL gas standards, was set up in 2019.
 214 The station also includes meteorological instruments, pressure and temperature sensors and visible cameras among
 215 other instrumentation for atmospheric and environmental monitoring.

216 2.3 The VAL station: Total column measurements

217 The VAL station, located in Vallejo in the northern part of MCMA, is part of the city's air quality network
 218 (RAMA) run by SEDEMA. An EM27/SUN spectrometer (EM27/SUN_104) was installed at this station in 2019
 219 together with a surface CO₂ sensor. The VAL spectrometer has been performing measurements with the two
 220 detectors since November 2019. **Additionally, the VAL site included a low-cost medium precision CO₂ sensor, as
 221 a part of a network implemented during the MERCI-CO2 campaign. It consists of a NDIR-type of sensor
 222 (SenseAir, model HPP3) that can measure in the 0 to 1000 ppm range and after a calibration and target gas follow-
 223 up procedure, can produce data with <1% accuracy (Porrás et al., 2023).**

224 3.1 FTIR data processing and analysis

225 In this study, we used the solar absorption measurements acquired by five different FTIR instruments
 226 (i.e: three EM27/SUN, a Vertex 80 and a IFS120/5HR) to estimate the XCO₂, and XCO total columns at each
 227 station. The retrieval strategies were adapted as a function of the spectral resolution and averaging kernel of each
 228 species. Table 2 summarises the different products used in this study, and their retrieval parameters.

229

230 **Table 2: FTIR analysis: Description of the different FTIR products, retrieval strategies and parameters used in this study.**

Instrument (spectral resolution)	Gas	Microwindows (cm ⁻¹)	Interfering gases	Retrieval code	Retrieval method
EM27/SUN and IFS-120/5HR LowRes (0.5 cm ⁻¹)	CO ₂	6173.0-6390.0	H ₂ O, CH ₄	PROFFAST	Scaling VMR COCCON strategy
	CO	4208.7-4318.8	H ₂ O, HDO, CH ₄ , HF		
	O ₂	7765.0 - 8005.0	H ₂ O, CO ₂ , HF		
IFS-120/5HR (0.02 cm ⁻¹) (TCCON-type)	CO ₂	6180.0 – 6260.0 6310.0-6380.0	H ₂ O, CH ₄ ,HDO	PROFFIT9.6	Scaling VMR
	CO	4208.7- 4257.3 4262.0 – 4318.8	CH ₄ , H ₂ O, HDO		
	O ₂	7765.0-8005.0	H ₂ O, CO ₂ , HF		
IFS-120/5HR (0.005 cm ⁻¹) (NDACC-type)	CO	2057.70-2058.00 2069.56-2069.76 2157.50-2159.15	O ₃ , N ₂ O, H ₂ O, OCS and CO ₂	PROFFIT9.6	Profile NDACC strategy

Vertex80 (0.1cm ⁻¹)	CO	2056.70 – 2059.00 2068.56-2069.77 2156.50-2160.15	O ₃ , N ₂ O, H ₂ O, OCS and CO ₂	PROFFIT9.6	Profile
------------------------------------	----	---	---	------------	---------

231

232 **3.1.1 EM27/SUN spectra analysis**

233 Double-sided interferograms from the EM27/SUN were analysed following the standardised COCCON protocol,
 234 using PREPROCESS and PROFFAST codes, developed by the KIT and made freely available ([https://www.imk-
 236 asf.kit.edu/english/COCCON.php](https://www.imk-

 235 asf.kit.edu/english/COCCON.php)). The codes and retrieval methods are fully described in Sha et al. (2020), Frey
 237 et al. (2021) and Alberti (2023) and only briefly summarised here. The PREPROCESS algorithm generates the
 238 required spectra by a Fast Fourier Transform. The processing incorporates various quality checks, as a signal
 239 threshold, intensity variations during recording, requirement of proper spectral abscissa scaling, and generates
 240 spectra only from raw measurements passing all checks (the remaining ones being flagged). We used the ILS
 241 parameters (i.e: modulation efficiency amplitude and phase error) reported on the KIT-COCCON website
 242 (<https://www.imk-asf.kit.edu/english/COCCON.php>) and in Alberti et al. (2022), corresponding to the initial KIT
 243 calibration of the spectrometers (Frey et al., 2019, Alberti et al., 2022). The PROFFAST-PCXS module (i.e:
 244 forward model of PROFFAST) pre-calculates daily lookup tables of the molecular absorption cross-sections
 245 according to the meteorological parameters and gas trace VMR profiles priors. The latest PROFFAST-PCXS
 246 version uses the HITRAN 2020 spectroscopic linelists (with some extensions, e.g., line mixing parameters added
 247 for CH₄). Here, we used the standard COCCON linelists as incorporated in the previous PROFFAST version, i.e:
 248 HITRAN 2008 for CH₄, HITRAN 2012 for CO₂, a modified version of HITRAN 2009 by Toon (2014) for H₂O, a
 249 TCCON standard linelist for O₂, and the same solar line list as previously used by TCCON (compiled by G.C.
 250 Toon for GGG2014). The least-squares fitting code PROFFAST-INVERS retrieves the total columns by scaling
 251 the prior VMR profiles iteratively until adjusting the fit to the measured spectra. The intraday variability of surface
 252 pressure is considered in the retrieval, interpolated from the in-situ pressure measurements. For tying the column-
 253 averaged abundances provided by COCCON to TCCON data, PROFFAST applies post-process Airmass-
 254 Dependent (ADCF) and -Independent (AICF) corrections, independent from the instrument, similar as used in the
 255 TCCON process (Sha et al., 2020, and Alberti, 2023). The corrections and parameters used are reported in the
 256 COCCON website and Alberti, (2023).

256 We automatized and adapted the data processing to obtain a preliminary “real-time” hourly-updated
 257 analysis (hereafter, AN1) for each site, additionally to the off-line treatment (hereafter, AN2) applying the standard
 258 COCCON procedure. The meteorological data used in the AN1 retrieval were derived from the daily-available
 259 radiosonde data, provided by Servicio Meteorologico Nacional (SMN) from measurements performed in the early
 260 morning (6 AM LT) at the Mexico City International Airport. The AN1 strategy adopted fixed VMR priors for
 261 each species, consisting in the averaged profile of 41 years (1980-2020) run of the Whole Atmospheric Community
 262 Climate Model (WACCM), as commonly used in the NDACC community. The AN2 processing, generating the
 263 COCCON standard products, used the daily TCCON meteorological data and priors (GGG2014 version of MAPS
 264 files), downloaded from the Caltech server, which are based on National Centers for Environmental Prediction
 265 (NCEP) reanalysis. For both AN1 and AN2 processing, we used the in situ intraday surface pressure measurements
 266 from the PCE-THB-40 sensors. A correction factor was applied to the pressure measurements to take into account

267 the bias between the different pressure sensors used, previously intercompared by a few days of side-by-side
268 measurements.

269 CO_2 , O_2 , and CO were analysed in the 6173.0-6390.0 cm^{-1} , 7765.0- 8005.0 cm^{-1} and 4208.7- 4318.8 cm^{-1}
270 spectral windows, respectively. The XCO_2 and XCO column-averaged dry air mole fractions were calculated using
271 the O_2 retrieved total columns, according to Wunch et al. (2009):

$$272 \quad X_{gas} = 0.2095 (C_{gas} / C_{O_2}) \quad (1)$$

273 where C_{gas} and C_{O_2} are the target gas and O_2 total columns, respectively.

274 The real-time (AN1) and COCCON (AN2) XCO_2 and XCO products showed relative differences lower than 0.05%
275 and 5%, respectively. The results presented hereafter are based on the official COCCON products (AN2 analysis).

276 3.1.2 Vertex80 and IFS120/5HR spectra analysis

277 High (0.005 cm^{-1}) and medium (0.02 cm^{-1} and 0.1 cm^{-1}) resolution solar-absorption spectra are processed
278 using the PROFFIT9.6 code (Hase et al., 2004).

279 XCO_2 is retrieved from the NIR 0.02 cm^{-1} resolution spectra applying the procedure described in Baylon et al.
280 (2017), in which two independent CO_2 and O_2 VMR-scaling retrievals are performed using fixed WCCAM VMR
281 priors and NCEP-derived meteorological data. Spectral windows and interfering gases (Table 2) are similar to
282 those used in the standard TCCON procedure. XCO_2 is then calculated from the retrieved CO_2 and O_2 total columns
283 by applying Eq. (1).

284 For the ALTZ analysis, CO was retrieved from the high (0.005 cm^{-1}) resolution spectra in the MIR region, applying
285 the standard NDACC procedure (Pougatchev et al., 1994; Rinsland et al. 1998; Table 2). It uses a profile retrieval
286 strategy with fixed WACCM VMR priors and NCEP meteorological data. Since the O_2 specie is not analysed in
287 the MIR region, the XCO was determined using the dry air columns (C_{dryair}):

$$289 \quad XCO = \frac{C_{CO}}{C_{dryair}} \quad (2)$$

290 with:

$$291 \quad C_{dryair} = \left(\frac{P_g}{g} \cdot m_{dryair} \right) - \left(C_{H_2O} \frac{m_{H_2O}}{m_{dryair}} \right) \quad (3)$$

292 where C_{CO} and C_{H_2O} are the retrieved CO and H_2O total columns, g the column-averaged gravity acceleration, P_g
293 the ground pressure and m_{dryair} and m_{H_2O} , the dry air and H_2O molecular masses respectively. In addition, we
294 analysed XCO from the NIR spectral region to complement the MIR time-series, occasionally interrupted when
295 the liquid nitrogen was missing at the station. The CO and O_2 columns in the NIR region were analysed using
296 scaling retrievals in the same spectral windows as that used by TCCON (Table 2), but with fixed WACCM VMR
297 priors and NCEP meteorological data. XCO was calculated from the CO and O_2 retrieved total columns applying
298 Eq. (1). To minimise the air mass dependence effect (likely low for CO), we filtered out data with a SZA $>60^\circ$.
299 XCO NIR and MIR products were compared and intercalibrated (section 3.1.3).

300 For UNA, we used the XCO total columns calculated from the Vertex80 measurements to complement the
301 EM27/SUN time series during the period when it was operating with a single detector (between March 2016 and
302 September 2017). CO was analysed from the 0.1 cm^{-1} resolution spectra in the MIR spectral range, using a standard
303

304 NDACC profile retrieval strategy and the PROFFIT9.6 retrieval program with constant WACCM VMR priors and
305 NCEP meteorological data. Spectral windows (Table 2) were adapted following Pougatchev and Rinsland (1995).
306 Previous CO total columns time series retrieved from the same method at UNA were presented in Garcia-Franco
307 et al. (2018) and Borsdorff et al. (2018, 2020). Only the constraint of these CO retrievals were adjusted for the
308 Megacity and allowed in addition a free fitting of the mixing layer concentration, following the work by Stremme
309 et al. (2009) in which low resolution MIR- spectra with a different retrieval program have been analysed.

310 **3.1.3 Measurement precision and FTIR product intercomparison**

311 Side-by-side measurements were performed at the ALTZ and UNA stations on several occasions (Table1)
312 to assess the FTIR measurement precisions, to characterise the bias between the different products and to define
313 the inter-calibration factors for the XCO₂ and XCO products. We used the EM27/SUN_62 products as reference,
314 for which we previously applied the standard XCO₂ and XCO calibration factors reported in Alberti et al. (2022),
315 to inter-calibrate our results with the COCCON network and the Karlsruhe TCCON station operated by KIT. The
316 linear regression parameters from the different measurement pairs and the calibration factors are presented in the
317 Supplementary data (Table S1 and S2).

318 We found a bias lower than 0.2% and 1.0% between the three EM27/SUN, for XCO₂ and XCO respectively, and
319 a coefficient of determination (R²) higher than 0.99.

320 On the other hand, the precision of the EM27/SUN measurements was assessed by calculating the standard
321 deviation over a 5 min-interval period, and found to be on average 2.7 ppb and 0.3 ppm for XCO and XCO₂,
322 respectively.

323 The intercomparison of the IFS120/5-HR high resolution (0.02 cm⁻¹) products and the EM27/SUN XCO₂ products
324 was performed for the daily average data used in this study. The calibration factors were determined using i) the
325 EM27/SUN XCO₂ products and ii) the IFS 120/5-HR low resolution (0.5 cm⁻¹) product (Fig. S2), processed in the
326 same way as the COCCON EM27/SUN data but having the advantage of being measured even outside the
327 campaigns carried out with the EM27/Sun. We finally found a bias around 0.4% (slope=0.996), and a coefficient
328 of determination R² of 0.92. This bias is of order of that expected when comparing TCCON and COCCON products
329 (Frey et al., 2019), when no empirical calibration is applied. On the other hand, a bias of 2% (and R²=0.92) was
330 found comparing the XCO from the EM27/SUN and the Vertex (MIR) products at UNA.

331 One of the main contributions of the apparent bias observed when comparing products from different instruments
332 and using different retrieval strategies can be due to their respective Averaging Kernel (AK) which characterise
333 the smoothing error. It is especially the case in the comparison of XCO from the EM27/SUN (i.e: NIR scaling
334 retrieval product, Degree Of Freedom (DOF) =1) and from the Vertex (MIR profile-product, DOF > 2). To assess
335 this effect, we refined the comparison after smoothing the vertically resolved Vertex profiles with the EM27/SUN
336 AK (following Rodgers, 2000; Borsdorff et al., 2014, 2018) and re-calculating the smoothed Vertex total columns.
337 After this smoothing, the bias is reduced to 0.2% instead of 4.1% for the CO total columns. For the XCO product,
338 which includes the use of the surface pressure for the MIR product and the retrieved O₂ column for the NIR product
339 the bias is reduced to 0.4% instead of 3.5%.

340 3.2 Surface CRDS data analysis

341 The surface CO₂ and CO data acquired with the CRDS analysers were processed and averaged following
 342 the procedure described in González del Castillo et al. (2022). Data were averaged and their standard deviation
 343 calculated, per minute, then per hour. To extract the trend and seasonal CO and CO₂ variability, data were filtered
 344 by discarding hours generally affected by transient and very local effects. Data recorded between 13 and 17h with
 345 standard deviations lower than 6.0 ppm were selected for the UNA station, while nighttime data (19 to 5h) with
 346 standard deviations lower than 2.0 ppm were selected for the ALTZ station, according to González del Castillo et
 347 al. (2022).

348 3.3 Mixed Layer height from the Lidar measurements

349 The MLH is retrieved using a combined algorithm based on the gradient method and a wavelet-covariance
 350 transformation as described in detail by García-Franco et al. (2018). These results were compared with radiosonde
 351 data and MLH values derived from surface and vertical column densities of trace gases, and more recently Burgos-
 352 Cuevas et al. (2022) used the variance of the vertical velocity from a Doppler Lidar (Wind Cube 100, Leosphere)
 353 and compared with the ceilometer results at the same location. These studies show that the ceilometer retrieved
 354 MLHs compare well with other techniques during the daytime (they agree within 15% with the trace gas method),
 355 which are relevant for this study, whereas late afternoon and nighttime retrieved values might be affected by
 356 aerosol residual layers at higher altitudes.

357 3.4 Mixed layer CO and CO₂ concentrations from FTIR measurements

358 Pollutant concentrations within the mixed layer are often estimated using surface measurements, although
 359 surface concentrations are very sensitive to the air mass vertical transport, unlike the total columns. It is especially
 360 the case within the Mexico City basin where the mixed layer has a strong diurnal dynamics controlling the vertical
 361 distribution of the emitted pollutants (Stremme et al., 2009; Garcia-Franco et al., 2018). An estimate of the CO₂
 362 and CO vertically averaged concentrations across the mixed layer can be made using the total columns measured
 363 at the UNA and ALTZ stations. The dry air mole fraction measured at the UNA station (XCO_2^{UNA}) is the weighted
 364 mean of that measured in the mixed layer (CO_2^{ML}) and in the free troposphere at the ALTZ station (XCO_2^{ALTZ}):
 365

$$366 \quad XCO_2^{UNA} = w_1 \times CO_2^{ML} + w_2 \times XCO_2^{ALTZ} \quad (4)$$

$$367 \quad CO_2^{ML} = \frac{XCO_2^{UNA} - w_2 \times XCO_2^{ALTZ}}{w_1} \quad (5)$$

368
 369 The weights (w_1 and w_2) depend on the pressure difference between the mixed-layer height (MLH) and the UNA
 370 station, the pressure on top of the mixed layer is calculated assuming an exponential decay and an effective scale
 371 height H_{scale} (assumed to be 8.0 km):
 372

$$373 \quad w_1 = \left(1 - e^{-\frac{MLH}{H_{scale}}}\right) \text{ and } w_2 = \left(e^{-\frac{MLH}{H_{scale}}}\right) \quad (6)$$

374 The MLH above Mexico City was estimated using the hourly-averaged measurements of the ceilometer at the
 375 UNA station. The hourly-averaged CO_2^{ML} and CO^{ML} products were calculated applying the same strategy for the
 376 entire time series and are reported in Fig. 7, concurrently to the surface data.

377 4 Results

378 The FTIR XCO_2 and XCO daily-averaged time series and CO_2 and CO surface concentrations obtained at the
 379 UNA, VAL and ALTZ stations between November 2015 and June 2021 are shown in Fig. 2. Trends and seasonal
 380 variabilities were fitted using a Fourier series analysis (Eq. (7) and black and red solid lines in Fig. 2), following
 381 Wunch et al. (2013):

382

$$383 f(x) = ax + \sum_{k=0}^n a_k \cos(2\pi kx) + b_k \sin(2\pi kx), \text{ with } n = 2 \quad (7)$$

384

385 where x is the time (decimal year), a the mean growth rate (ppm/year), and a_k and b_k the Fourier coefficients
 386 modulating the annual cycles. The coefficients for each gas species and station are reported in Table 3.

387

388 *Table 3: Fourier series fitting parameters for the UNA, VAL and ALTZ XCO_2 and XCO time series presented in Fig. 2, and*
 389 *calculated from Eq.(7).*

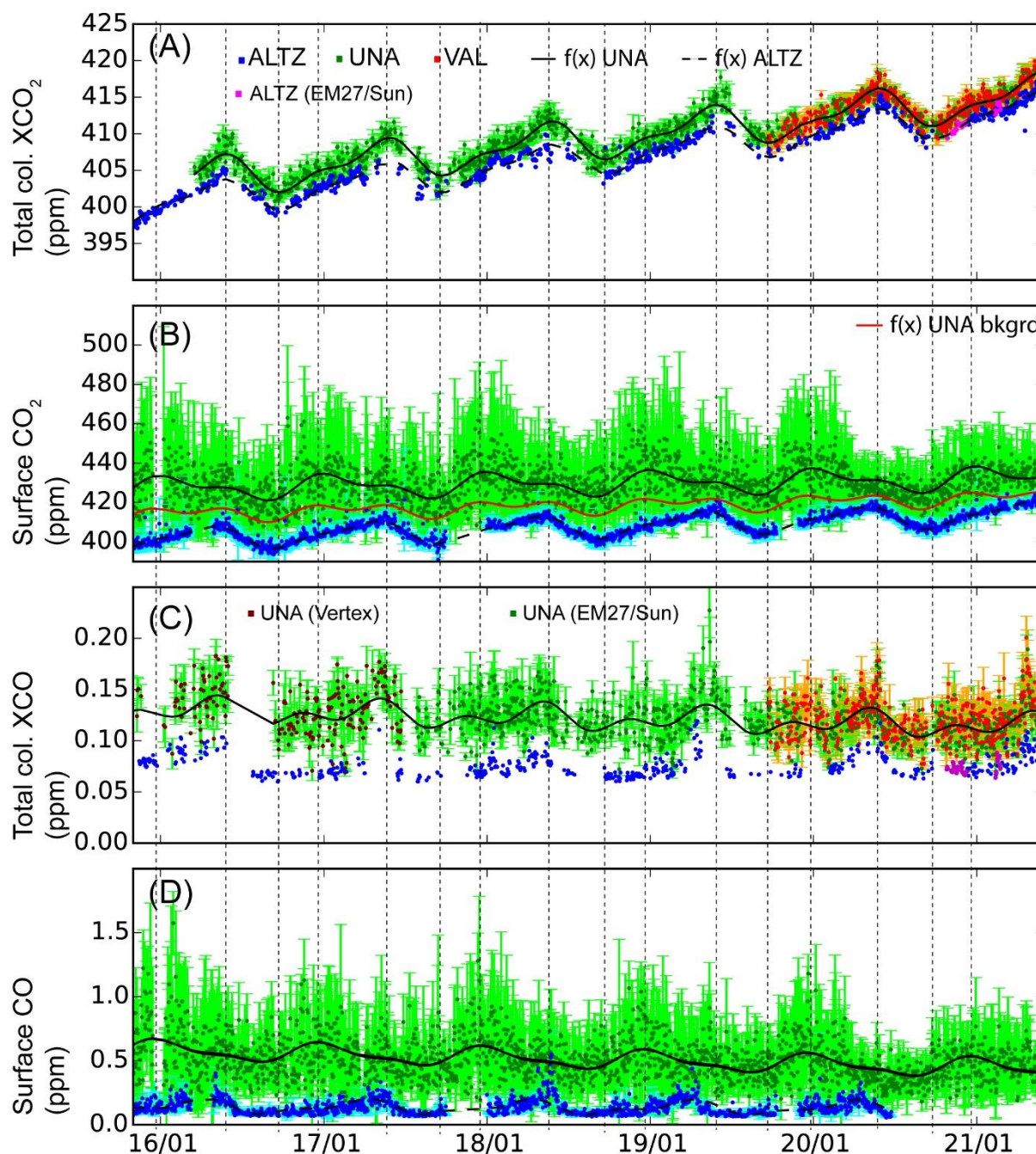
Fitting parameters (ppm/year)	XCO_2 , UNA Tot. Col.	XCO_2 ALTZ Tot. Col.	CO_2 UNA Surface	CO_2 ALTZ Surface	XCO UNA Tot. Col.	CO UNA Surface
a	2.25 ± 0.02	2.40 ± 0.01	1.6 ± 0.1	2.48 ± 0.02	$(-4.0 \pm 0.8) \times 10^{-3}$	$(-2.7 \pm 0.1) \times 10^{-2}$
a_1	-1.06 ± 0.04	-0.78 ± 0.04	1.7 ± 0.2	-0.39 ± 0.05	$(-2.4 \pm 0.7) \times 10^{-3}$	$(6.5 \pm 0.4) \times 10^{-2}$
a_2	2.11 ± 0.04	1.93 ± 0.04	1.1 ± 0.2	-0.36 ± 0.05	$(-3.2 \pm 0.8) \times 10^{-3}$	$(1.5 \pm 0.4) \times 10^{-2}$
b_1	0.71 ± 0.04	0.64 ± 0.04	2.1 ± 0.2	4.62 ± 0.05	$(8.6 \pm 0.8) \times 10^{-3}$	$(6.5 \pm 4.0) \times 10^{-3}$
b_2	-0.78 ± 0.04	-0.45 ± 0.04	-2.1 ± 0.2	-1.69 ± 0.05	$(-7.9 \pm 0.7) \times 10^{-3}$	$(-2.2 \pm 0.4) \times 10^{-2}$

390 4.1 Trends and interannual variability

391 The total column XCO_2 time series (Fig. 2A) at ALTZ and UNA show a similar mean growth rate around 2.4
 392 ppm/year (2.4 and 2.3 ppm/year for ALTZ and UNA, respectively, Table 3) over the whole measurement period.
 393 A similar mean growth rate is also found for the surface CO_2 time series (Table 3 and Fig. 2 B) in ALTZ (2.5
 394 ppm/year). These values are consistent with those estimated at the Mauna Loa Observatory (MLO) reference
 395 station for the 2016-2021 period (average of 2.5 ± 0.5 calculated from surface data available in the NOAA site
 396 <https://gml.noaa.gov/ccgg/trends>).

397 At the UNA station a surface mean growth rate of 1.6 ppm/year is found, lower than that observed from the total
 398 column measurements. Comparing the surface mean growth rates with those reported by González del Castillo et

399 al. (2022) for the 2014-2019 period, we observe a significant difference for the UNA station (2.3 ppm/year in
 400 González del Castillo et al., 2022) but very similar values for the ALTZ station (2.6 ppm/year in González del
 401 Castillo et al., 2022). The difference observed at UNA could stem from (i) starting our new time series at the end
 402



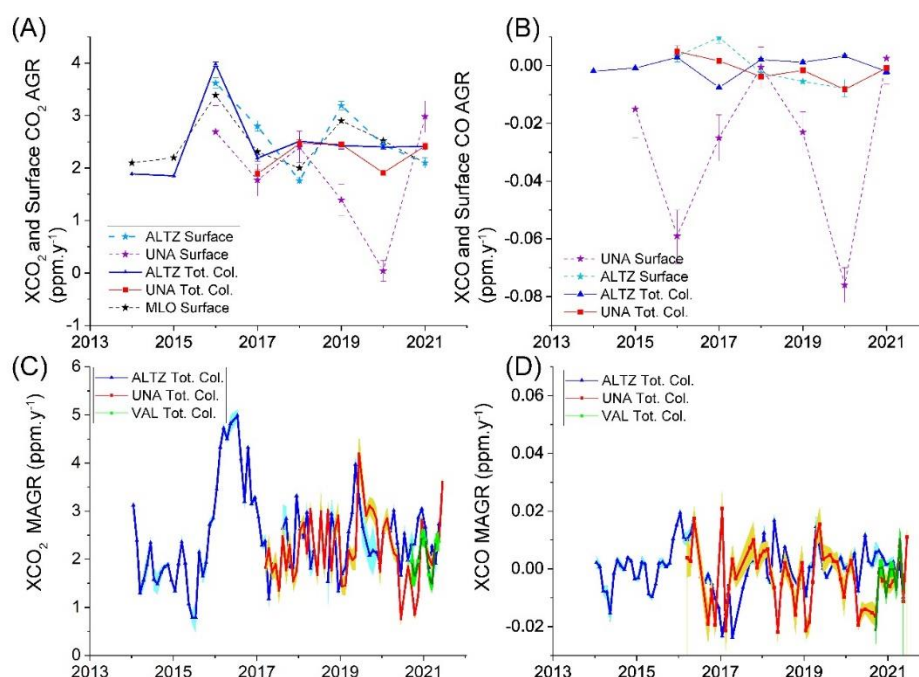
403
 404 **Figure 2:** Time series of (A) the total column XCO_2 from the FTIR measurements (B) the CO_2 surface concentration
 405 from the CRDS measurements, (C) the total column XCO from the FTIR measurements (D) the CO surface
 406 concentration from the CRDS measurements for the UNA (in green), VAL (in red) and ALTZ (in blue) stations. For
 407 each time series, the daily average data are presented as dots with their daily standard deviations. Black traces show
 408 the annual fit calculated from the Fourier series (Eq. (7)). In (A) and (C), we distinguished between ALTZ data obtained
 409 from the IFS120/5HR (in blue) and from the EM27/Sun (in magenta) and in (C), between the CO total columns obtained
 410 from the VERTEX instrument (in brown) and the EM27/Sun (in green) at the UNA station. In (B) the red curve
 411 corresponds to the background fit, calculated following González del Castillo et al. (2022), to determine the annual trend
 412 and seasonal cycles. Dash lines highlight the minimum and maximum of the annual cycles for the different products.

413 of 2015, when the annual growth rate is maximum (González del Castillo et al., 2022) and (ii) the inclusion of the
 414 2019-2021 period, when the mean growth rate clearly decreased. At the VAL station, the total column XCO₂ time
 415 series are found very similar to those observed at UNA stations (Fig. 2A). Figure S1 shows that 86% of the daily
 416 average data at VAL and UNA have a difference lower than 1.0 ppm, although a large part of the comparison was
 417 done during the COVID19 lock-down period (Table1), for which lower gradients are expected due to the decrease
 418 of the anthropogenic emissions.

419 The interannual variability can be explored through the time series of the mean annual growth rate (AGR) and the
 420 monthly-sampled annual growth rate (MAGR), according to Buchwitz et al. (2018). The MAGR is calculated by
 421 month, as the difference between the monthly-average Xgas data of a year *i* and the monthly-averaged data of the
 422 previous year (*i-1*). The AGR is obtained for each year, averaging all of the MAGR. The AGR and MAGR for
 423 total column and surface measurements are presented in Fig. 3. We include data from the MLO in Fig. 3A, for
 424 which the AGR (dashed black curve) was derived from the surface data available in the NOAA site.

425 At ALTZ, the interannual variability of the total column XCO₂ AGR (Fig. 3A) was found similar to that obtained
 426 from both the ALTZ and MLO surface data, with a coincident peak in 2016, reaching an AGR value of 3.5 (surface
 427 data) and 4.0 (total column data) ppm/year. Surface data AGR time series show a second peak in 2019, which is
 428 not apparent for the total column XCO₂ time series. The time series of the MAGR (Fig. 3C) allows better
 429 identifying and characterising the period and duration of the anomalies. The 2016 XCO₂ anomaly has a duration
 430 up to 15 months (from October 2015 to March 2017), reaching a maximum value (around 5.0 ppm/year) between
 431 March and July 2016, corresponding to a factor of 2.8 higher than the 2013-2015 base level (1.8 ppm/year).

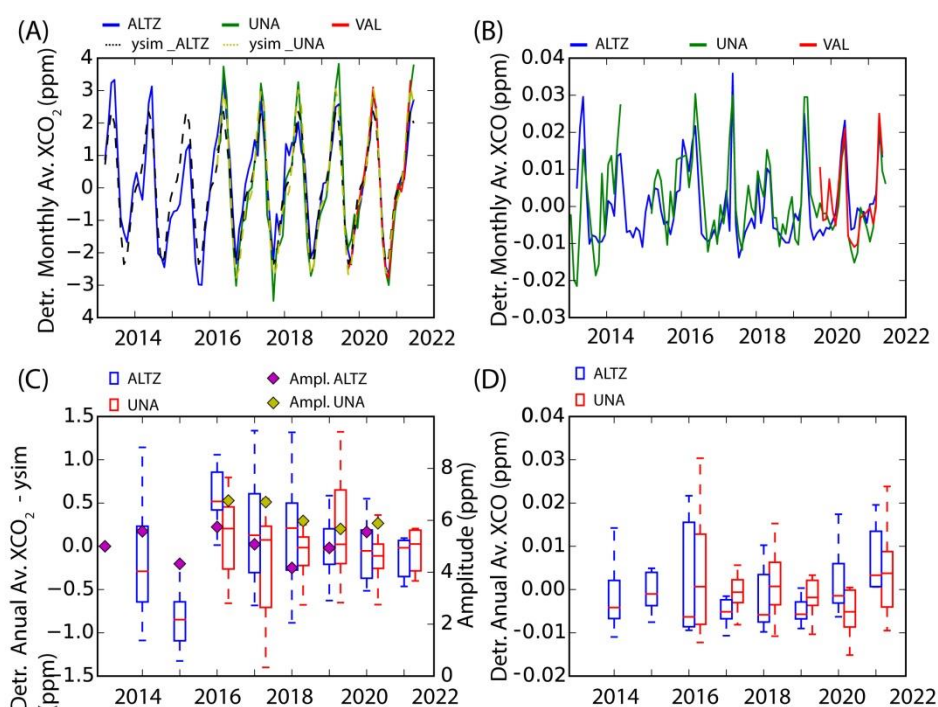
432



433

434 **Figure 3:** XCO₂ (A) and XCO (B) annual growth rates (AGR) and XCO₂ (C) and XCO (D) monthly-sampled annual
 435 growth rate (MAGR) obtained from total column and surface measurements for UNA, VAL, and ALTZ stations. In
 436 (A), the Mauna Loa (MLO) AGR trend was added in black dash-line. In (A) and (B) errors bars represent the standard
 437 error after removing annual cycles, reflecting the data sample quality. The standard error for the MAGR is shown as
 438 shaded area in (C) and (D).

439 At UNA, the XCO₂ AGRs and MAGRs time series (Fig. 3A and C) are very similar to those observed at the ALTZ
 440 station, except for the year 2020. During this year, the AGR dropped by ~20% at UNA before returning in 2021
 441 to the level of the previous two years. This behaviour contrasts with the AGR observed at ALTZ, which remains
 442 nearly constant between 2017 and 2021. The MAGR time series at UNA (Fig. 3C) shows that this drop is
 443 dominated by the exceptionally low June and October growth rates, representing the lowest MAGR values of the
 444 UNA time series. This observation is supported by the VAL MAGR, although the time series is much shorter. The
 445 surface CO₂ AGR at UNA shows a much higher interannual variability, with the strongest anomaly observed in
 446 2020, where the AGR is close to zero. A very clear decrease of the day-to-day and intraday CO₂ surface variability
 447 is observed in Fig. 2B from April to mid-September 2020, consistent with the XCO₂ MAGR anomaly.
 448



449
 450 **Figure 4: Interannual and annual variability of the detrended XCO₂ and XCO total column data at the UNA, VAL and**
 451 **ALTZ stations. In (C) and (D) the whisker diagrams are calculated from the monthly average detrended data. The**
 452 **amplitude is determined as the max-min values.**

453 Upon examining CO, the UNA XCO time series (Fig. 2C) has daily averages ranging between 0.10 and
 454 0.23 ppm with a mean and standard deviation of 0.12 and 0.02 ppm, respectively, but shows a decreasing rate (-4.0×10^{-3} ppm/year)
 455 over the whole measurement period. The VAL XCO time series show a very similar baseline
 456 to UNA, with a daily average difference lower than 0.02 ppm for 85% of the coincident dataset (Fig. S1). At the
 457 ALTZ background site, the XCO baseline and day-to-day variability are lower than at UNA and VAL, as expected
 458 (mean and standard deviation equal to 0.08 and 0.01 ppm, respectively). The surface CO time series (Fig. 2D)
 459 shows a more significant decreasing trend (-2.68×10^{-2} ppm/year) than the total column data at UNA, while the
 460 baseline at ALTZ remains constant around 0.11 ppm. The CO AGR and MAGR at ALTZ and UNA are shown in
 461 Fig. 3B and D. Generally, the XCO AGR and MAGR oscillate around their base level at the ALTZ and UNA
 462 stations, with short-term anomalies. At ALTZ, a strong negative XCO AGR anomaly is observed in 2017, which
 463 was not observed for XCO₂, likely resulting from the exceptionally high XCO columns measured during 2016.
 464 This is supported by the increase of the XCO MAGR from October 2015 to July 2016 (Fig. 3D), coinciding with

465 the first 10 months of the highest XCO₂ anomaly and followed by the lowest XCOMAGR values of the time series
 466 (around -0.02 ppm/year in April 2017). At the UNA station, the AGR slightly decreases between 2016 and 2020
 467 and increases again in 2021. The most significant and prolonged (>5 months) MAGR anomaly (Fig. 3D) occurred
 468 between April and September 2020, with negative values. Some short-term additional anomalies are observed, but
 469 only a few of them (in May 2018 and January 2019) are not affected by the limited number of available
 470 measurements.

471 **4.2 Seasonal variability and short-term cyclic events**

472 Annual cycles are observed for both total column XCO₂ and CO₂ surface measurements at ALTZ, UNA and VAL
 473 stations (Fig. 2). The maximum and minimum of the total column XCO₂ cycles are observed in May-June and
 474 September, respectively, with an average amplitude around 5 (ALTZ) and 6 (UNA) ppm.

475 To examine the temporal changes in amplitude and shape of the annual cycles, total column data were monthly-
 476 averaged, detrended by subtracting the linear part of the fit ($f(x) = ax$, in Eq. (7)), and compared to the detrended
 477 mean annual cycle ($f(x) - ax$) in Fig. 4. To obtain a longer-term view, we included the 2013-2015 period from the
 478 ALTZ station, previously published in Baylon et al. (2017), after applying the inter-calibration factors (section
 479 3.1.3). At ALTZ, two periods significantly deviated from the average XCO₂ seasonal cycle, i.e.: (i) the year 2015,
 480 where all the monthly averaged XCO₂ are below the fit and with one of the lowest seasonal amplitudes (~4.0 ppm,
 481 Fig. 4A and 4C) of the whole time series, and (ii) the year 2016, with higher monthly averages than the mean
 482 XCO₂ seasonal cycle and the highest amplitude (~5.8 ppm, Fig. 4A and 4C). At UNA, the difference with respect
 483 to the average XCO₂ seasonal cycle is not significant, except for the year 2020, where all the monthly averages
 484 are below the mean annual cycle (Figure 4C). During this period, the UNA and VAL XCO₂ monthly-averaged
 485 data fit exceptionally well with those of the ALTZ station between March 2020 and March 2021 in terms of shape
 486 and amplitude, while the UNA and VAL annual cycle amplitudes are slightly higher than those of ALTZ for the
 487 other years.

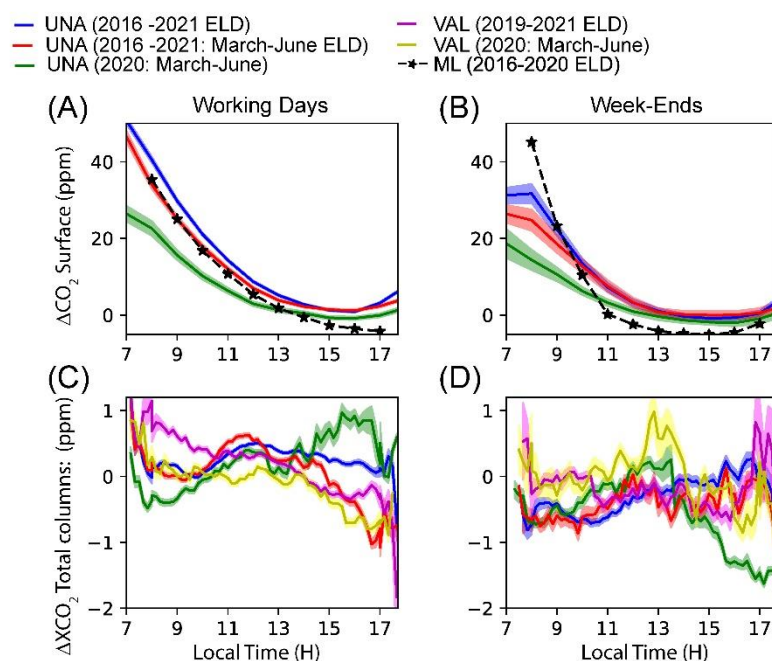
488 Regarding the CO₂ surface data (Fig. 2B), annual cycles are observed with maxima and minima reached mid-
 489 December and mid-September, respectively. As also reported in González del Castillo et al. (2022), the maximum
 490 occurred during winter, when shallower boundary layer prevails and the summer-autumn minimum can be
 491 explained by the dilution of trace gases in a deeper convective boundary layer and more active urban vegetation.
 492 XCO peaks every year in April-May at the three stations (Fig. 2C and Fig. 4B) and then shows minimal annual
 493 values in August, preceding by 1 month the minimum and maximum values of the XCO₂ time series. The April-
 494 May maximal annual values, also confirmed by TROPOMI measurements (Borsdorff et al., 2020), coincide with
 495 the biomass burning season and the periods during which the mixed layer reaches its maximum altitude (García-
 496 Franco et al., 2018). During 2015, the XCO time series show a very low maximum reached in February instead of
 497 May (Fig. 4B), contrasting with 2016, where high total column XCO values are reached in January and maintained
 498 for a period of at least 5 months. 2016 also corresponds to the year with the highest XCO variability of the time
 499 series (Figure 4D). Additionally, in 2018, the XCO annual cycles differ from the other years with lower values
 500 and a flat shape during the first semester of the year (January-May).

501 Surface CO data (Fig. 2D) also show periodic increases at the ALTZ station with maxima reached during April-
 502 May, coinciding with the maxima observed from total column XCO measurements. They confirm the increase of
 503 the CO emissions during the biomass burning season, at least dominant in the ALTZ measurements. However, at

504 the UNA station, cycles are also observed in the surface data but with a maximum coinciding with that of the CO₂
 505 surface data, and lagging behind the XCO₂ total columns. These cycles are likely dominated by other processes
 506 affecting both CO and CO₂ species such as the mixed layer seasonal dynamic.

507 4.3 Intraday variability

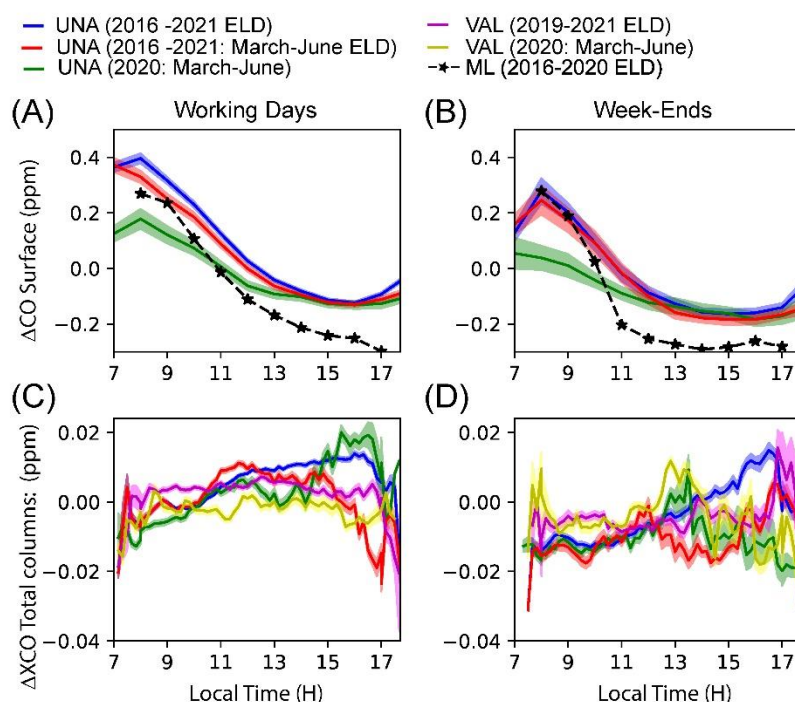
508 The intraday variability of the total columns and surface data are depicted in Fig. 5 and Fig. 6. Since the ALTZ
 509 total column data do not present a significant diurnal pattern (the hourly variability remains lower than the standard
 510 error of the time series), they are not presented in these plots.



511
 512 **Figure 5: Diurnal patterns of the detrended surface CO₂ mole fractions (A and B) and XCO₂ total columns (C and D)**
 513 **measured at UNA and VAL stations. For each panel, the different curves represent different time periods: in blue, the**
 514 **whole measurement period excluding the lock-down period (March-June 2020 ELD), in green the lock-down period**
 515 **(March-June 2020) and in red the whole measurement periods from March to June, excluding the lock-down. The**
 516 **standard errors are presented as shaded areas. Black curves represent the diurnal pattern of CO₂ in the Mixed Layer**
 517 **(ML) calculated from the total columns data for the UNA station.**

518 Total column data were detrended by removing the seasonal fit (black traces in Fig. 2A and Fig. 2C), and averaged
 519 over 10 min. To avoid a possible bias due to strong ventilation periods, a filter based on a ventilation index (VI)
 520 was applied, following recommendations in Hardy (2001), Su et al. (2018) and Storey and Price (2022). The VI is
 521 calculated as the product of average wind speed velocity (between the surface and 100 m height), and the planetary
 522 boundary layer height for UNA and VAL locations. The wind velocity and the MLH were estimated with the U
 523 and V wind components and the PBL height fields from the hourly ERA5 reanalysis product (Hersbach et al.,
 524 2020). In the MCMA, the surface wind speed presents a diurnal pattern, generally reaching a maximum during the
 525 afternoon between 14 and 15h LT (Fig. S4). The filter selects the days complying with the following criteria (i) a
 526 maximum wind velocity (average 10-100m height) between 10h and 12h LT lower than 1.5 m.s⁻¹ (threshold based
 527 on Stremme et al., 2013) and (ii) a daily VI lower than 2350 m².s⁻¹, which represents a commonly used threshold
 528 for selecting poor ventilation conditions (Hardy, 2001; Storey and Price, 2022). About 60% of the original XCO₂
 529 and XCO dataset is selected by applying the filter, and will be considered in the following analysis. We note that
 530 about 70% of discarded data corresponds to the January-May period of the year. Filtered total column XCO₂ and

531 XCO data were averaged by 10 min and presented in Fig. 5C-D and Fig. 6C-D, distinguishing between the working
 532 days (WD) and the week-end (WE) periods. To explore the 2020 lock-down influence on the diurnal pattern, three
 533 different periods were distinguished for each plot, the first one (blue trace: 2016 - 2021) corresponding to the
 534 whole measurement period excluding the interval between March and June 2020 corresponding to the lock-down
 535 period (hereafter, called “ELD” for “excluding the lock down period”), where a significant MAGR decrease was
 536 observed; the second (green trace: March- June 2020) only includes the lock-down period, and additionally
 537 excludes the rainy season to avoid bias due to incomplete daily time series; and the third period (red trace) is the
 538 same as the first one, but only considering the March to June months to be compared with the lock-down period.



539

540 **Figure 6: Same as Figure 5, but from surface CO and total column XCO measurements.**

541 Surface data from the CRDS analyzers were detrended by removing the background fit following the methodology
 542 described in the section 3.2, and filtered to be coincident with the filtered total column measurements (selection of
 543 data between 7 and 18 h LT and only including the days with low ventilation conditions). They were finally
 544 averaged by hours and presented in Fig. 5A-B and Fig. 6A-B for the WD and WE periods, respectively, for which
 545 each curve represents the periods mentioned above.

546

547 The surface CO₂ diurnal pattern at UNA station for the whole measurement period (2016-2021, Fig. 5A and B in
 548 blue) is consistent with the one previously described in Gonzalez del Castillo et al. (2022) for the 2014-2019
 549 period, with a maximum observed during the early morning (reached before 7 h LT), a minimum during the
 550 afternoon (between 15 and 16 h LT) and an average amplitude around 45 ppm. A lower amplitude of these cycles
 551 is observed at WE (average amplitude of 28 ppm) with respect to the WD periods. During the 2020 lock-down
 552 period (green curve), the WD surface CO₂ diurnal profile has a comparable amplitude (average amplitude of 26
 553 ppm) to those of the WE for the whole measurement period, and slightly higher than that observed during the lock-
 554 down WE periods (average amplitude of 22 ppm). The surface CO diurnal profile (Fig. 6: 2016-2021, blue curve)
 555 peaks at 8h and then decreases until 16 h LT during any day of the week. The WD and WE data shows amplitudes

556 of up to 0.5 ppm and 0.3 ppm, respectively. During the lock-down period the WD and WE amplitudes are much
557 lower (0.3 and 0.2, respectively), consistently with the CO₂ surface observations.

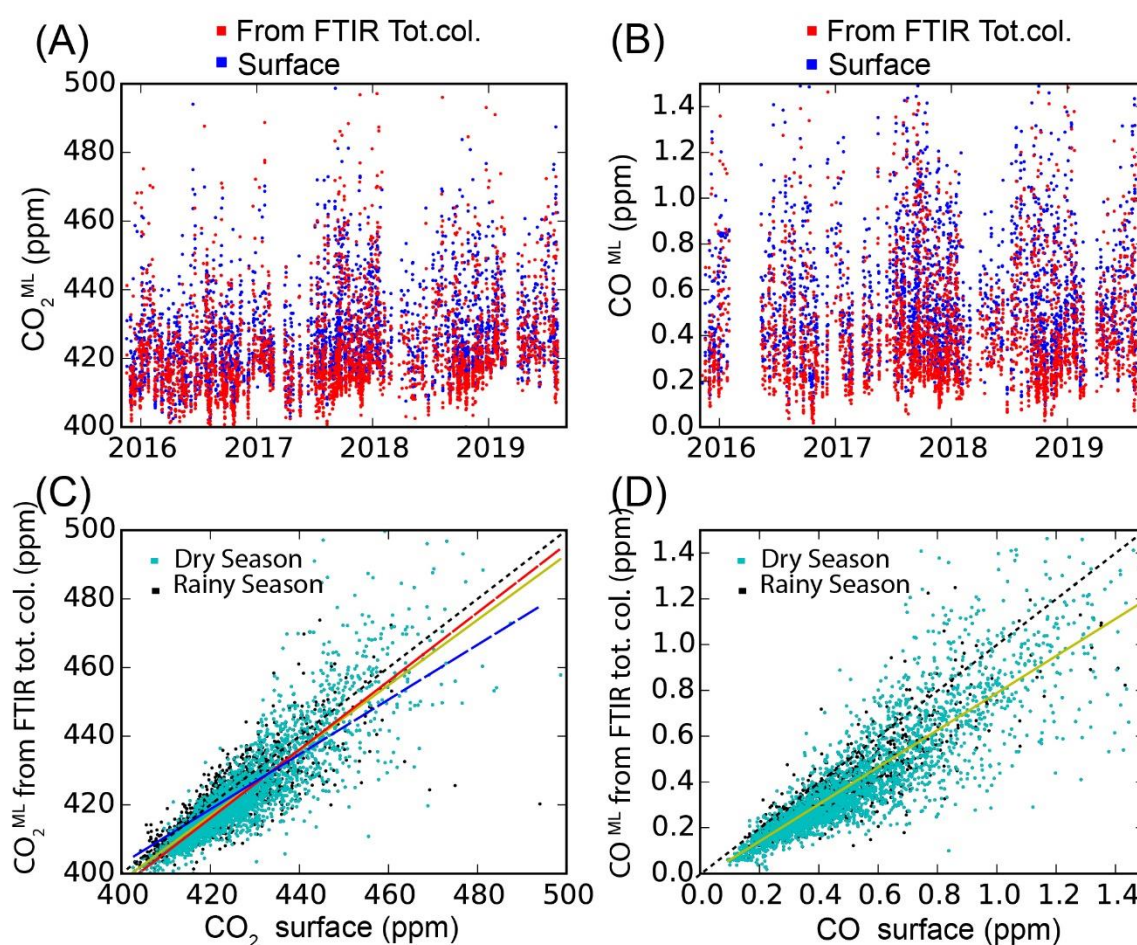
558 The XCO₂ and XCO diurnal patterns (Fig. 5C-D and Fig. 6C-D) have very different shapes than those of the surface
559 data, with amplitudes one order of magnitude lower. The variability observed between 7 and 8h is likely due to
560 the low number of measurements during this time interval, and will not be taken into account in the following
561 analysis. The UNA and VAL XCO₂ diurnal patterns significantly differ in shape. The VAL WD curve (magenta
562 trace) continuously decreases from 8h to 17h (amplitude around 2 ppm) during both the whole measurement and
563 lock-down periods, but during the lockdown period, lower values are generally recorded with higher intra-hour
564 variability between 11h and 14h. The general WD decreasing trend suggests a maximum reached during the early
565 morning (before 7 h LT). This observation is supported by the CO₂ surface measurements performed with the low-
566 cost medium precision CO₂ sensors (Porrás et al., 2023), recording a maximum between 6h and 7h LT. The UNA
567 XCO₂ WD diurnal pattern (blue trace) is almost constant until 10h, then increases until reaching a maximum around
568 12h, slightly decreases until 17h LT and finally shows an abrupt decrease after that. The amplitude of the diurnal
569 variability is around 1 ppm. During the lock-down period, the diurnal profile is different, increasing until 12h LT,
570 slightly decreasing until 13h LT and then increasing again until reaching a maximum at 16h, and finally abruptly
571 decreasing until 17h LT. The lock-down WD XCO₂ profile shows lower values than the other periods until 13h,
572 but the peak observed at 16h is not apparent for the other periods. Variability is generally lower at WE (<1ppm),
573 except for the lock-down period, for which an important decrease is observed after 14h LT, but it is likely affected
574 by a low number of measurement days. For XCO, the diurnal profiles also have different shapes at UNA and VAL.
575 At UNA, the March-June XCO diurnal profiles (red and green curves) resemble that of XCO₂ for both the lock
576 down and whole measurement periods. When considering the twelve months of the year (blue trace), the maximum
577 curve slightly increases between 12h and 16h, when it reaches its maximum. It contrasts with the variability of the
578 March to June months curves during this time interval, for which an increase is observed during the lock-down
579 period or a decrease if considering the whole measurement period. At VAL, the diurnal profile is fairly constant
580 until 17h with slightly lower values during the lock-down period.

581 The total column XCO diurnal profiles at WE are less reliable with larger standard errors, likely due to the low
582 number of considered measurements. An increase is nevertheless observed at UNA where the considered day's
583 number is statistically more reliable, with a peak around 17h LT, which was not observed for XCO₂.

584 The difference observed between the diurnal pattern of the XCO and XCO₂ at VAL and UNA is likely due to the
585 different advection drivers in the region mainly controlled by the topography. A Northern surface wind direction
586 (Figure S6) is generally dominating over the Mexican valley but is locally highly influenced by the mountainous
587 barriers. The West-northwest wind component at UNA is likely to be the effect of down-slope flows from the
588 mountain ridge in the early morning (6 – 9 LT mostly), while at VAL, the plateau-to-basin winds are the main
589 influx into the basin coming from the northwest in the morning. There can also be an influence from an up-valley
590 flow in the mornings (de Foy et al., 2006). More generally the VAL station is likely influenced by the north
591 mountain, generating a significant gradient in the CO distribution upwind of the VAL station (Figure 1). In
592 contrast, near the UNA station, the flat ground allows a more efficient mixing and due to the dominant North-
593 Northeast wind component in the late morning, the captured airmasses likely often reflects the MCMA plume
594 emissions.

595 4.4 CO and CO₂ within the mixed layer from FTIR and surface data.

596 Figure 7 shows the hourly-averaged CO₂ and CO concentration within the mixed layer (CO₂^{ML} and CO^{ML})
 597 products), calculated from the FTIR measurements (see section 3.4), concurrently to the surface data. The CO₂^{ML}
 598 and CO^{ML} products are in agreement with the surface observation, with a slope of 0.95 ± 0.02 ($R^2=0.74$) for CO₂
 599 (Fig. 7C) and 0.81 ± 0.02 ($R^2=0.74$) for XCO (Fig. 7D). For CO₂, the slope was found closer to 1.0 (1.00 ± 0.02)
 600 with an offset of -2.9 ± 0.2 and a better R^2 (0.77) when discarding the data corresponding to the rainy season. This
 601 effect is likely due to the removal of the incomplete daily time series frequently interrupted at the beginning of the
 602 afternoon during the rainy season.
 603



604
 605 **Figure 7: Comparison between (A) the CO₂^{ML} and (B) CO^{ML} products (red) derived from the ALTZ and UNA total**
 606 **column measurements and the surface measurements at the UNA station (blue). (C) and (D) represent the correlation**
 607 **plots for CO₂ and CO, respectively. In (C) and (D), we distinguished between data corresponding to the dry (November**
 608 **to May: cyan) and rainy (June to October: black) seasons. In (C), yellow, red and blue linear regression curves**
 609 **correspond to the whole measurement period (yellow: slope= 0.95 ± 0.02 ; Offset= 17.9 ± 0.2 ; $R^2=0.74$), the dry season (red:**
 610 **slope= 1.00 ± 0.02 ; Offset: -2.9 ± 0.2 ; $R^2=0.77$) and the rainy season (blue: slope= 0.80 ± 0.03 ; Offset: 83.7 ± 0.39 ; $R^2=0.66$). In**
 611 **(D), since no significant difference was found for the different period, the regression line (yellow: slope= 0.81 ± 0.02 ;**
 612 **offset: -0.021 ± 0.004 ; $R^2=0.74$) represent the whole measurement. The black dash line represents $y=x$.**

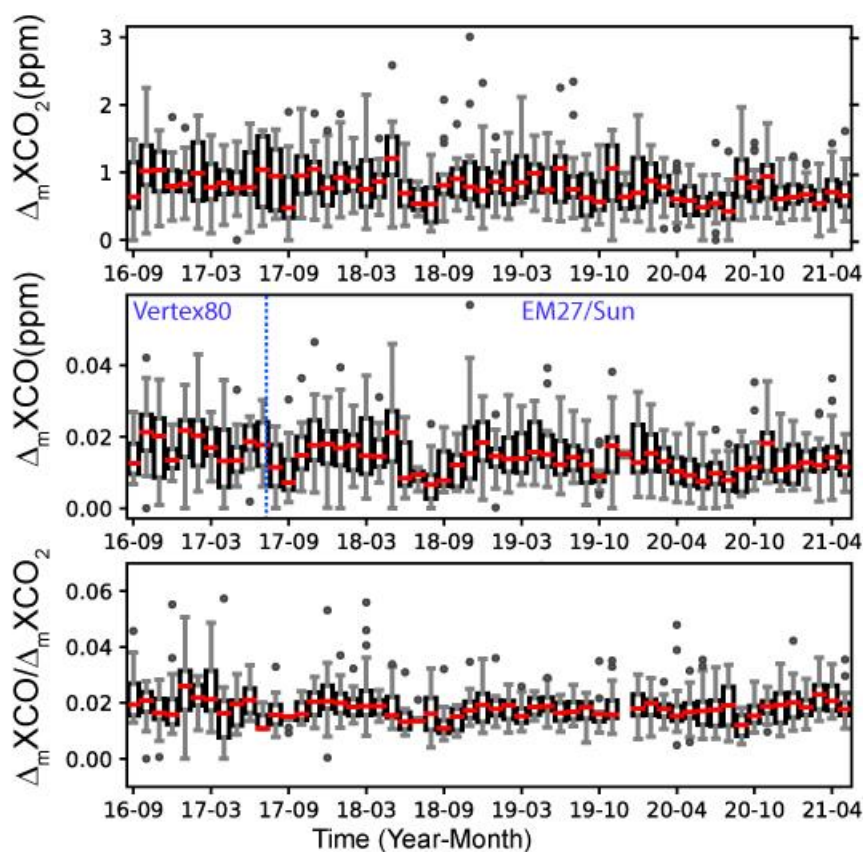
613
 614 The CO₂^{ML} and CO^{ML} diurnal patterns are presented in Fig. 5 and Fig. 6 (dash lines) together with those of surface
 615 measurements, after a similar filtering. The CO₂^{ML} and surface CO₂ diurnal patterns (Fig. 5A) are very similar in
 616 shape and amplitude, especially during the WD, although a small difference is observed at the end of the afternoon

617 (<5 ppm). This difference is likely due to the increase of the uncertainties of the MLH estimate when it is more
 618 diluted. The CO^{ML} and surface CO diurnal profiles (Fig. 6A) also have similar amplitudes and shape for both WD
 619 and WE, although the CO^{ML} diurnal profile shows lower values (offset around 0.1 ppm at WD). Despite this very
 620 simplified model, these results show that the total column and surface measurements are mutually very consistent
 621 when the seasonal and diurnal variability of the ML expansion above Mexico City is taken into account.

622 4.5 XCO_2 to XCO enhancements ratios

623 The XCO and XCO_2 correlated enhancements and their ratio can give insights into the combustion efficiency of
 624 the sources in a city, and therefore on their contributions. In this study we explored the variability of the
 625 XCO/XCO_2 ratios at both long-term and intraday scales.

626 For the long-term analysis, the XCO_2 “background” level was calculated using a statistical method, using the lower
 627 5th percentile of the measured Xgas over a 1-day running window (You et al., 2021). We did not use the ALTZ
 628 measurements because of (i) the periodic influence of the wildfires in the region during the dry season, and (ii) the
 629 discontinuity of our daily averaged time series. The enhancements above background $\Delta_m\text{XCO}_2$ and $\Delta_m\text{XCO}$
 630 measured at UNA and averaged by months and their ratios are presented in Fig. 8, as whisker diagrams.



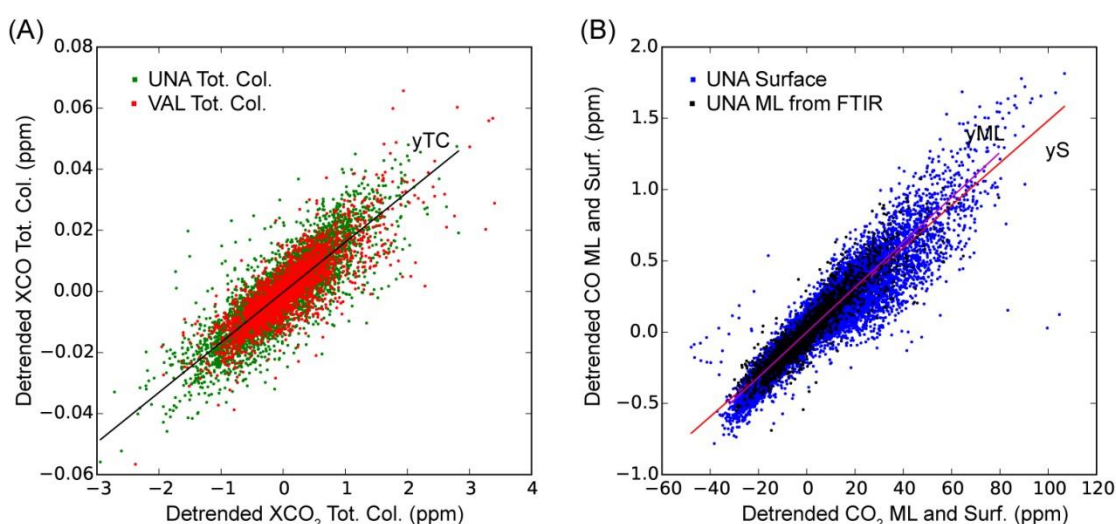
631
 632 **Figure 8: Whisker diagram representing by month the variability of ΔXCO_2 , ΔXCO and their ratio from the UNA**
 633 **measurements.**

634 Both $\Delta_m\text{XCO}_2$ and $\Delta_m\text{XCO}$ time series show a slight decrease over time (around 0.05 ppm/year and 0.001
 635 ppm/year, respectively). Although the $\Delta_m\text{XCO}/\Delta_m\text{XCO}_2$ ratio displays a variability around its mean value
 636 (0.018 ± 0.003), there are no discernible cyclic or long-term trend in the time series, except for the rainy periods of
 637 2017, 2018 and 2020 when low ratios (and low $\Delta_m\text{XCO}$ and $\Delta_m\text{XCO}_2$ values) were observed. The $\Delta_m\text{XCO}$ and
 638 $\Delta_m\text{XCO}/\Delta_m\text{XCO}_2$ ratio show a higher variability at the beginning of the time series (until July 2017) likely due to

639 the use of the CO Vertex products. The long term $\Delta_m XCO$, also observed in other studies (Garcia-Franco, et al.,
 640 2019; Molina, 2021, Hernández-Paniagua et al., 2021) likely reflect the successive air quality management
 641 programs implemented in the CDMX since the 1990s to improve the air quality, including technological
 642 advancements and fuel quality enhancements as well as refinery closures, industrial relocation, or fuel substitution.
 643 Regarding the low seasonal variability observed for the CO/CO₂ ratios, it is likely related to mass burning episodes
 644 and high-pressure weather conditions that occur during the dry season.

645 To perform the intraday analysis, the hourly-averaged data were first detrended by subtracting the daily average.
 646 The resulting $\Delta_i XCO_2$ vs. $\Delta_i XCO$ datasets are plotted in Fig. 9A. The entire $\Delta_i XCO_2$ and $\Delta_i XCO$ datasets showed
 647 a good correlation at both the UNA and VAL stations, with similar linear regression slopes around 0.0164 ± 0.0003 ,
 648 which is consistent with that found from the surface measurements and the ML product (Fig. 9B). Although there
 649 is an actual difference in the emission types of the southern and northern parts of the city, the North hosting
 650 industrial and commercial sources and the South being largely residential and commercial, the common and
 651 dominant source of CO in the MCMA (at UNA and VAL stations) could incriminate motorised vehicles. The data
 652 dispersion around the regression line likely reflects more punctual and local influence of other sources with an
 653 important week-to-week variability.

654



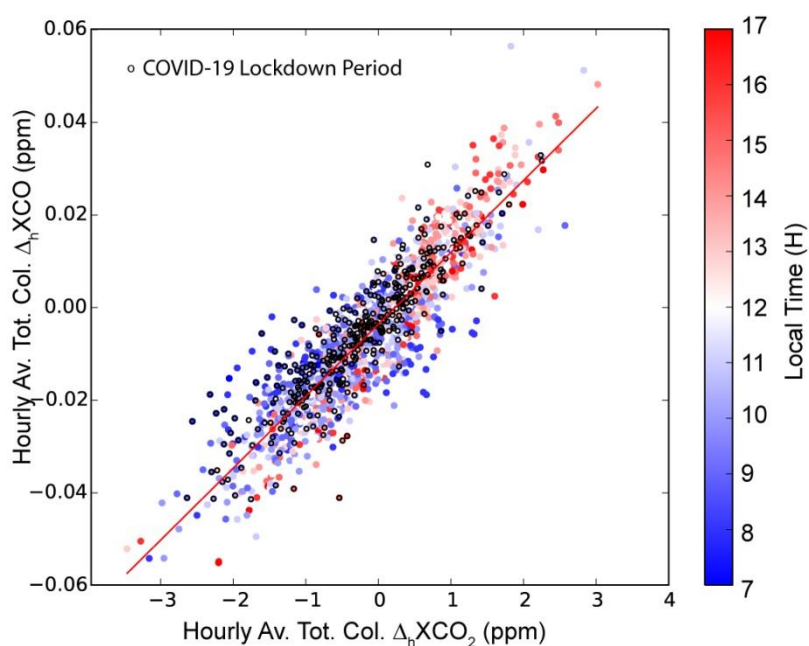
655

656

657 **Figure 9: A: Correlation plot of (A) the detrended (by removing the daily averages) hourly-average total column XCO₂**
 658 **vs. XCO data, and (B) the detrended hourly average Mixing Layer (ML) and surface CO₂ vs. CO products. Solid lines**
 659 **represent the linear regression lines, with the following parameters: TC slope= 0.0164 ± 0.0003 , $R^2=0.72$ for the total**
 660 **columns at UNA and VAL; yS slope= 0.0148 ± 0.0001 , $R^2=0.87$ for the surface products and yML slope= 0.0158 ± 0.0002 ,**
 661 **$R^2=0.88$ for the Mixing Layer products.**

662 On the other hand, the total column (UNA-VAL) differences, presented in Fig. S3 can also be used to calculate
 663 the $\Delta XCO/\Delta XCO_2$ ratio, with a more precise subtraction of a common background (which assumes a
 664 homogeneous background across the entire city) from the two stations. Figure 10 shows the hourly-average ΔXCO_2
 665 (UNA-VAL) vs. ΔXCO (UNA-VAL) correlation plot for the coincident measurement period. A well-defined
 666 linear correlation is observed with a slope of 0.015 ± 0.001 and a coefficient of determination of $R^2=0.80$, highly
 667 consistent with that found in Fig. 9. The use of the (UNA-VAL) total columns difference notably improved the
 668 coefficient of determination, by removing the regional long-term and short-term perturbations affecting the two
 669 sites. The intraday variability of the ΔXCO (UNA-VAL)/ ΔXCO_2 (UNA-VAL) ratio (Fig. 10: colour scale),

670 showing higher columns at VAL during the morning and at UNA during the afternoon likely reflect the North to
 671 South transport of air across the city. We note that the ratio remains the same during the lock-down period. We
 672 would expect lower intraday (UNA-VAL) ΔXCO and ΔXCO_2 amplitudes during the lock-down period, but it is
 673 not clearly apparent in this correlation plot.



674
 675 **Figure 10: Correlation plot of the ΔXCO (UNA - VAL) vs. ΔXCO_2 (UNA - VAL) hourly averages (colour scale**
 676 **depending on the time is shown to the right) for the coincident measurement period (September 2019 - June 2021). Dots**
 677 **with black edges highlight the measurements during the COVID19 lock-down period (March-June 2020). Regression**
 678 **line (in red): Slope: 0.015 ± 0.001 , $R^2=0.80$.**

679 4.6 Estimate of CO and CO₂ MCMA emissions.

680 The variability of the long-term CO emissions in the MCMA can be estimated, following the method detailed in
 681 Stremme et al. (2013). In that study, they assumed that, since the XCO emissions in the MCMA are mainly due to
 682 traffic pollution, the rapid changes observed in the XCO total column (less affected by the airmass vertical
 683 distribution) should reflect the CO fresh emissions under certain meteorological conditions. Low ventilation,
 684 strong turbulence in the mixed layer and limited zenithal angle of measurements are critical criteria to avoid
 685 enhancement due to horizontal transport or local heterogeneity. XCO growth rates can be estimated at specific
 686 time intervals complying with these conditions from long-term time series. Further details on the method and
 687 estimates of uncertainties due to these assumptions are given in Stremme et al. (2013). Here, we determined an
 688 optimised time interval for estimating the mean CO growth rate using (i) the diurnal surface wind speed patterns
 689 and (ii) the MLH growth rate, the latter reflecting the turbulence within the mixed layer (Fig. S4). The time interval
 690 complying with a rapid growth of the mixed layer and low surface wind speed ($< 2 \text{ m}\cdot\text{s}^{-1}$) was found between 10
 691 and 12h, which is in agreement with the requirements mentioned in Stremme et al. (2013). Growth rates and their
 692 uncertainties were determined by year, based on the linear regression (with 95% confidence interval) of the 10-
 693 min averaged detrended CO total columns over the 10-12h interval. For example, for the year 2018, we found a
 694 CO growth rate of $52 \pm 5 \text{ kg}\cdot\text{km}^{-2}\cdot\text{h}^{-1}$.

695 To extrapolate the growth rate over the MCMA, we used the TROPOMI CO total column data that we averaged
 696 over the 2018-2022 period (Fig. 1), following the same method as described in Stremme et al. (2013). We assume

697 that the total amount of fresh CO is proportional to the total emission of the MCMA and to the total column
 698 enhancement at the UNA site, which reflects the CO accumulated at this site. The ratio of the total accumulated
 699 CO in the MCMA to the accumulated CO at UNA is therefore the same as the emission ratio of the whole Megacity
 700 to the emission flux at UNA. Therefore this ratio is the extrapolation factor and represents an effective area, defined
 701 as Eq. (8):

$$702 \quad Eff_Area = \frac{\int(CO_{MCMA} - CO_{bgrd})}{CO_{UNA} - CO_{bgrd}} \quad (8)$$

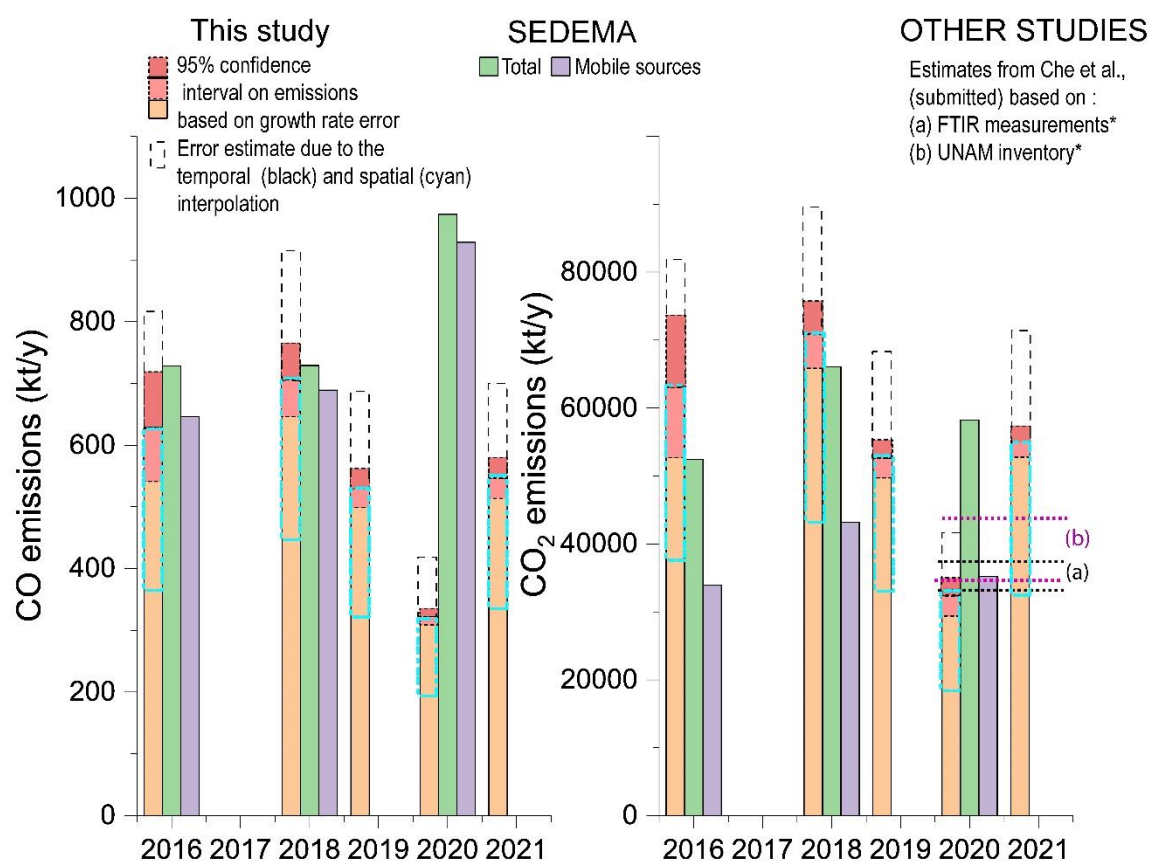
703 In Eq. (8), $(CO_{MCMA} - CO_{bgrd})$ is integrated over the area where the CO TROPOMI total columns are higher than
 704 a predefined background value. As the TROPOMI overflight time is around 13h30 LT, we cannot neglect the
 705 ventilation and slight advection is smoothing out the distribution, so that both the background and the column at
 706 UNA have to be chosen carefully. The background column was therefore estimated in two ways (i) from the
 707 smallest value observed upwind of the city (cross symbol in Fig. 1) at the elevation of the Mexican basin (contour
 708 line separating Mexico City from the Toluca area in the west in Fig. 1) and found to be 1.45×10^{18} molec.cm⁻² and
 709 (ii) from the Tecamac site, where the border of MCMA was assumed in Stremme et al. (2013) and where the
 710 column was found to be 1.60×10^{18} molec.cm⁻².

711 Due to advection, even locations slightly out of the megacity are presenting enhanced CO columns and it is not
 712 clear which is the background column in the Mexican basin. Figure S5 illustrated the sensitivity of the effective
 713 area to the background uncertainties. A 10% higher background leads to a 40% smaller extrapolation factor and a
 714 40% emission underestimate. The fresh CO was estimated from the TROPOMI data by removing the background
 715 (1.45×10^{18} molec.cm⁻²) to the average total columns found at UNA (1.93×10^{18} molec.cm⁻²) and was found to be
 716 4.79×10^{17} molec.cm⁻². In cases where the CO total column is lower than the background, likely due to the
 717 topography effect, we set the difference column to zero for the integration. This topographic effect is important
 718 for the considered area, as there are plenty of mountains around the basin, like the mountain ridge in the west
 719 (including Ajusco, Desierto de Leones, etc.), some mountains in the mountain ridge on the eastern part of the area
 720 including in the south the two volcanoes Popocatepetl and Iztaccihuatl.

721 Finally, we found effective areas of ~2017 km² (outer area, blue contour line in Fig.1) and ~1178 km² (inner area,
 722 red contour line in Fig.1) considering the two background values given above. The “inner area” reflects conditions
 723 without ventilation effect, therefore the outer area is more appropriate for the emission estimates given that the
 724 TROPOMI measurements occurred at 13:30 when the ventilation cannot be neglected. The other estimates
 725 calculated from the inner area will be thereafter only indicated within brackets and considered to estimate the
 726 sensitivity of the result.

727 Since the measured growth rate corresponds to a time interval of only 2 hours in the middle of the day, the CO
 728 intraday fluctuations have to be taken into account. Stremme et al. (2013) used a factor which was taken from the
 729 available bottom-up inventories and described that the CO emissions per/day are roughly 18.5 times the emission
 730 per hour at noon. Assuming the same factor, we estimate a CO rate around 0.71 ± 0.06 (0.42 ± 0.04) Tg/year for
 731 2018. If no information about the diurnal distribution of the emission rate is available, we should assume a uniform
 732 distribution and an upper value of the CO rate could be estimated using an intraday time interpolation factor of 24
 733 hours instead of 18.5, finally resulting in ~30% higher estimates. Despite the significant uncertainties introduced

734 by spatial and temporal interpolation, their impact on the relative variability, trends and anomalies of the emission
 735 rates is less important if the same method and assumptions are consistently applied across the entire time series.
 736 CO₂ emissions could not be directly estimated using the same method, given its complex diurnal pattern, which is
 737 a cumulative result of both natural and anthropogenic contributions and likely been influenced by additional
 738 factors, related to instrumental and retrieval effects (i.e: air mass dependence error with a sub-percentage
 739 contribution for CO₂, non-ideal column sensitivity of the retrieval which represent near 25% overestimation for
 740 CO₂ anomaly and 5% underestimation for CO anomaly in the PBL). Instead, we based our CO₂ estimates on the
 741 measured XCO/XCO₂ ratio. The average XCO/XCO₂ molec. ratio (0.0164 ± 0.0003) determined from the UNA
 742 and VAL total column measurement (Fig. 9) was converted to a mass ratio (multiplying it by the molecular weight
 743 ratio) and found to be 0.0100 ± 0.0002 . Considering this ratio, we estimated the CO₂ annual emission at 71 ± 6 (42 ± 4)
 744 Tg/year for 2018. Our estimates of CO and CO₂ emissions by year and their average over the whole time series,
 745 applying the same method, are presented in Fig. 11 and Table S3, concurrently with the SEDEMA inventories for
 746 the MCMA. We obtained a 2016-2021 CO and CO₂ average emissions of 0.55 ± 0.02 (0.32 ± 0.01) and 46 ± 2 (32 ± 1)
 747 Tg/year, respectively, when excluding the lockdown period (Table S3). Here, the given uncertainties are solely
 748 those stemming from the propagation of errors in growth rate estimates. Uncertainties on absolute values are much
 749 higher when considering spatial and temporal extrapolations errors, but they do not influence the interpretation of
 750 relative values.



*: The same intraday temporal interpolation factor was applied for the comparison. (a) and (b) were based on the 10/2020 - 05/2021 period

751
 752 **Figure 11: Comparison of CO and CO₂ emission estimations from UNA FTIR diurnal growth rates and from SEDEMA**
 753 **inventories. For CO₂ (right), the estimates from Che et al. (submitted) are also reported, although it was based on the 10/2020**
 754 **to 05/2021 period, after applying the same intraday temporal factor as used for our study to convert the Gg/hour to kt/year.**

755 5 Discussion

756 5.1 Long term variability

757 In this contribution, we characterised the seasonal and inter-annual variability and trends of the CO and CO₂ total
758 column and surface concentrations from two urban and one background stations. The average total column 2013-
759 2019 growth rate obtained at ALTZ (~2.5 ppm/year) and its inter-annual variability are in accordance with that
760 typical of the Northern Hemisphere measurements from TCCON stations (hereafter, NH-TCCON) (Sussman et
761 al., 2020: AGR of 2.4 ppm/year for the 2012-2019 period).

762 Both the NH-TCCON and ALTZ stations captured an important increase of the AGR in 2016 (+1.1 ppm/year for
763 the TCCON stations and +2.1 ppm/year for the ALTZ station with respect to 2015), coinciding with the most
764 intense ENSO (El Niño Southern Oscillation) event since the 1950s'. The impact of "El Niño" events on the carbon
765 cycle is not yet fully understood, although they are consistently accompanied by a global increase of XCO₂ due to
766 increasing drought in many regions and a decrease in global land carbon uptake. In 2016, an increase of 1.3
767 ppm/year was observed in the Mauna Loa in situ AGR with respect to 2015 (Betts et al., 2018), for which the
768 contribution of the 'El Niño' event was estimated at about 25%, the rest ascribed to an increase of the
769 anthropogenic emissions. In Mexico, the "El Niño" events are generally associated with a decrease in
770 precipitations, with deficits which can reach up to 250 mm in the South-Western area of the country, causing
771 drought and a higher occurrence of wild and forest fires (Bravo-Cabrera et al., 2018, González del Castillo et al.,
772 2020). Our observations from the ALTZ measurements highlight a much higher XCO₂ increase (+2.1 ppm/year)
773 during 2016 with respect to 2015 than that observed at the NH-TCCON stations. During this period a small increase
774 in the XCO MAGR (~ +0.02 ppm) is also observed at both ALTZ and UNA stations, maintaining the highest
775 values of the whole time series over more than 4 months. Assuming that the CO MAGR variability captured at the
776 ALTZ station during 2016 rather reflects a change in the global MCMA's emissions, we attempt to delineate the
777 global and local contributions in the 2016 XCO₂ ALTZ AGR increase. Adopting a molecular CO/CO₂ ratio of ~
778 0.016, a hypothetical increase of the XCO₂ MAGR over the 09/2015 - 09/2016 period due to the local emissions
779 would be around +1.2 ppm/year, thus about 60% of the observed increasing rate during this period (+2.1 ppm/year).
780 This gross estimate suggests that the El Niño regional effect only contributed at about 25% (0.9 ppm) to the
781 observed AGR increase, which is close to the estimate from the NH-TCCON stations (~ +1.1 ppm) and from in
782 situ data.

783 On the other hand, our long-term FTIR and surface time series allows examining the effect of the COVID-19 lock-
784 down on the tropospheric CO₂ and CO concentration above the MCMA at local and regional scales. The reduction
785 of the surface CO and CO₂ AGR at UNA (CO₂ AGR to a value close to zero, and CO AGR ~ -0.1 ppm/year) with
786 respect to the other years (Fig. 3), and the strong diminution of their amplitude in the mean diurnal cycles clearly
787 reflect a significant decrease of the local emissions near the UNA station, likely due to a drastic reduction of the
788 urban traffic (the average annual congestion level decreased from 52% in 2019 to 36% in 2020 in Mexico City,
789 from TomTom available estimates <https://www.tomtom.com/traffic-index/mexico-city-traffic/>).

790 The FTIR total column XCO₂ and XCO time series at UNA did not capture such a drastic change, only a small
791 punctual decrease of the MAGR lower than the standard deviation of the whole time series was observed between
792 April and October 2020. These results are in accordance with previous studies in other parts of the world. Although
793 a reduction of 8.8% of the global CO₂ emissions was observed during the first five months of 2020 (Liu et al.,

794 2020; Jones et al., 2020) and an annual reduction from 4 to 7% (Le Quéré et al., 2020), the atmospheric total
 795 column XCO₂ showed a less clear effect (Sussman et al., 2020).

796 **5.2 CO/CO₂ ratio and MCMA emission estimates**

797 In this study, we robustly determined the CO/CO₂ ratio characterising the combustion efficiency of the city
 798 (0.016±0.01) from both surface and total column measurements at two urban stations. We found the same ratio for
 799 the UNA and VAL stations, and this ratio is very consistent with that found using the (UNA-VAL) gradients and
 800 using the surface measurements. This ratio is also consistent with that reported by MacDonald et al. (2023),
 801 calculated from TROPOMI and OCO-2/3 measurements (0.019) and slightly higher than that obtained from the
 802 EDGAR, FFDAS and ODIAC inventories (ratio ~0.012) reported in the same study.

803 Our estimate of CO emissions from the UNA measurements is based on a simplified approach, limited to
 804 days with low ventilation and time intervals corresponding to the late morning hours. It assumes a homogeneous
 805 area in the footprint and averages selected days without discrimination. Given that the temporal and spatial
 806 extrapolation introduces large uncertainties, only the relative and interannual behaviour of the emission can be
 807 discussed here, but the approach demonstrates how close column growth rate can be related to emission flux, if
 808 meteorological conditions allow neglecting advection. Our estimated range of CO emissions are consistent with
 809 the SEDEMA inventories at least for the year 2016 (factor 0.98) and 2018 (factor 1.04) if considering that they are
 810 dominated by the mobile sources. However, it is not the case for 2020, for which our estimate is much lower than
 811 SEDEMA by a factor of 0.3. During the lock-down period we estimated a decrease of about 55% compared to
 812 2018 while in the SEDEMA report, 2020 is the year with the maximum CO emissions (increase of 35% compared
 813 to 2018 considering the mobile sources). Both of these estimates contrast with Kutralam-Muniasamy et al. (2021),
 814 which reported an increase of 1.1% during the lock-down using the RAMA surface data. The large difference
 815 observed between these different studies can be due to i) the different methods used for extrapolating in space and
 816 time the emissions, ii) higher uncertainties of the FTIR-based estimates due to an important reduction the selected
 817 days of measurements and iii) an over-estimation of the SEDEMA inventory due to a lack of data during the lock-
 818 down period. Our estimate is based on the extrapolation of data from only one station (UNA), for which the
 819 dominant source is mainly the UNAM traffic activity. During the lockdown, the UNAM was closed and a
 820 significant reduction of the local traffic was recorded, but this traffic reduction was likely not representative of the
 821 whole MCMA. However, the decrease of the **MAGR** at both VAL and UNA stations does not support the increase
 822 of the CO emissions estimated by the SEDEMA inventory. Interestingly, it was not possible to apply the same
 823 method to calculate CO emissions at VAL because the average growth rate was close to zero (Fig. 6). This
 824 behaviour at VAL is likely due to the fast dispersion of the pollutant at this site, weakening the link between the
 825 diurnal pattern and the emissions.

826 Regarding CO₂, our estimates also agree with the SEDEMA's inventory, especially if we consider the total
 827 emissions instead of mobile sources (factor of 1.2 and 1.1) for the years 2016 and 2018. For 2020, we estimated a
 828 decrease of 55% while the SEDEMA inventory indicates a decrease of about 10%. **The CO/CO₂ ratios calculated**
 829 **from the SEDEMA data for total emissions are similar to ours (0.014 and 0.011 in 2016 and 2018, respectively),**
 830 **suggesting that our average CO/CO₂ ratio is actually representative of the global mixing of the different sources**
 831 **of the MCMA, and not only dominated by the road traffic. Interestingly, according to the SEDEMA inventory,**
 832 **road traffic, the main anthropogenic CO source is identified by ratios (0.019 and 0.016 in 2016 and 2018,**

833 respectively) only slightly higher than our global average; whilst the industrial and domestic burning sectors, which
834 represent the second main CO₂ anthropogenic sources, produces a one order of magnitude lower ratio. In any case,
835 our measurements are well representative of the main source of the CO and CO₂ anthropogenic emissions. Indeed,
836 if we consider the 2018 SEDEMA ratio for mobile sources (0.016), we find CO₂ emissions of the order of 43,100
837 kt/year for this year, within ~5% of the SEDEMA estimates.

838 Our results were also compared with the estimates reported in Che et al. (2023, submitted), based on an intensive
839 FTIR measurement campaign performed during the 10/2020 to 05/2021 period and using a Column-Stochastic
840 Time-Inverted Lagrangian Transport model (X-STILT) and a bayesian inversion (Fig. 11). Considering the same
841 measurement period, our method leads to CO₂ emission estimates ranging between 29,000 and 49,800 kt/year
842 using inner and outer effective area, respectively, which is consistent with the estimates obtained in Che et al.
843 (submitted), ranging between 32,700 and 37,200 kt/year when applying the same intraday temporal extrapolation
844 factor. Although the method we used for estimating the MCMA emissions is coarse and contains large
845 uncertainties, mainly due to the temporal and space extrapolation, it shows the ability to use one station capturing
846 the variability of the anthropogenic emissions of the MCMA and providing a year-by-year follow-up emission
847 information without using complex dispersion models.

848 **6 Summary and conclusion**

849 We have analysed the variability of the total column XCO and XCO₂ above the MCMA from two urban and one
850 background stations. The long-term XCO₂ data at the ALTZ station shows an average annual growth rate of ~2.5
851 ppm/year, similar to what has been reported from TCCON stations in the northern hemisphere, and captured the
852 perturbation driven by the 2015-2016 El Niño event. The urban stations show a similar growth rate (~2.3 ppm/year)
853 and unlike at ALTZ, a slight decrease of XCO₂ and XCO during the COVID19 lock-down period could be
854 observed. The CO₂ and CO concentrations within the mixed layer, estimated from the FTIR total column
855 measurements and ceilometer data, were found to be consistent with the surface measurements. These findings
856 confirm that the concentrations near the surface are mainly controlled by the emissions and the daily behaviour of
857 the mixed layer in MCMA. Our long-term total column and surface time series from both urban stations allowed
858 us to determine with great confidence an average CO/CO₂ ratio, indicative of the Mexico City combustion
859 efficiency. The CO/CO₂ ratio over our long-term measurement period seems to be fairly constant and equals ~
860 0.016 (mass ratio: 0.010). This value is consistent with other studies such as from satellite measurements (OCO-
861 2/3 and TROPOMI) and the bottom-up inventories reported by MacDonald et al. (2023). Finally, we estimated the
862 CO emissions using the average daily growth rate determined from measurements at the UNA station. Although
863 this method likely leads to an under-estimate of the emissions due to the non-negligible effects of advection, our
864 results were found to be very consistent with the 2016 and 2018 SEDEMA inventories. **The same strategy could**
865 **not be applied at the VAL station, likely because of dominant southward advection of the airmass, due to the**
866 **complex topography in this part of the MCMA. In contrast, the UNA station is located in a flat ground downwind**
867 **of the main anthropogenic source of the MCMA which likely allows establishing a direct relationship between the**
868 **columnar measurements and the MCMA CO and CO₂ emissions.** We finally estimated the CO₂ emissions using
869 the CO growth rate and the CO/CO₂ ratio. The finding that our CO₂ emission estimates are within 20% of those of
870 SEDEMA for total emissions show that our ratio reflects not only the traffic sources but is also affected by other
871 sources such as industrial activities and domestic burning. The UNA station, with its advantageous orography, is

872 therefore a good site to capture well-mixed emissions from the city and serves as a site to follow the interannual
873 variability and trends of the emissions in this urban environment. Finally, this study showed the feasibility to
874 monitor the long-term evolution of anthropogenic CO₂ and CO emissions in Mexico City by deploying only a few
875 EM27/SUN instruments. **The methodology employed here for monitoring the long-term temporal variability of**
876 **CO emission fluxes is likely to be adapted to other urban areas where the topography damps the ventilation down**
877 **for several hours each day, thereby establishing that the column growth rate is dominated by the emission flux.**
878 **Although the straightforward model presented here is not intended to replace a complex transport/chemical model**
879 **for a precise estimate of city emissions, the results obtained demonstrate that it is nevertheless possible to track**
880 **their temporal evolution with a high degree of reliability.**

881 **7 Author contribution**

882 All the co-authors contributed in the discussion of concepts, and to the preparation of the manuscript. NT, WS and
883 MG were responsible of FTIR measurements and the data analysis. MG and WS lead the ALTZ station
884 development and its long-term operation. AB and EGC were responsible of the maintenance of the instruments at
885 the Alzomoni station. VA helped to classify the days and hours with low ventilation and strong turbulence and
886 provided the UNAM emission inventory. EGC was in charge of the in-situ measurements, with the support of OL.
887 MG and MR led the MERCI-CO₂ project. FH lead at KIT the German-Mexican collaboration for the deployment
888 of the high resolution FTIR spectrometer and supports its long-term operation as part of NDACC. FH has helped
889 in the design and setup of the spectrometer and solar tracker before it was shipped to Mexico. He has developed
890 the retrieval code PROFFIT and gives continuously support to the UNAM group for its use and in operating the
891 spectrometer. FH and CA lead the German-Mexican collaboration and give precious help for the EM27/Sun
892 measurements in the frame of the COCCON network. All the co-authors contributed of the **writing** of the
893 manuscript.

894 **8 Competing interests**

895 The authors declare that they have no conflict of interest.

896 **9 Acknowledgements**

897 **We thank the two reviewers for their very constructive comments, which help to significantly improve the**
898 **manuscript.** We acknowledge the CONACyT-ANR project 290589 ‘Mexico City’s Regional Carbon Impacts’
899 (ANR-17-CE04-0013-01) for funding. Also the former projects CONACYT 239618 “El estudio del ciclo de
900 Carbono y de los gases de efecto invernadero utilizando espectroscopia de absorción solar” and UNAM-DGAPA
901 PAPIIT IN111521/IN106024 are acknowledged. We acknowledge the CONACyT-ANR project 290589 ‘Mexico
902 City’s Regional Carbon Impacts’ (ANR-17-CE04-0013-01) for funding. We acknowledge the technical assistance
903 provided by Omar López, Alfredo Rodriguez, Miguel Robles, Delibes Flores, and the Instituto de Ciencias de la
904 Atmósfera y del Cambio Climatico (UNAM) for the institutional support to carry out this study. We thank T.
905 Blumenstock from the KIT for his precious help and fruitful discussion during the last years. We thank Dr. Thomas
906 Boulesteix for his help at the Alzomoni site, his fruitful discussions.

907

908 **10 References**

- 909 Alberti Arroyo, C. A.: Ground based FTIR and MAX-DOAS observations of greenhouse and trace gas
 910 emissions in the Rhine valley (Germany), St. Petersburg and Yekaterinburg (Russia), Karlsruhe Institut für
 911 Technologie (KIT), <https://doi.org/10.5445/IR/1000162056/v2>, 2023.
- 912 Alberti, C., Hase, F., Frey, M., Dubravica, D., Blumenstock, T., Dehn, A., Castracane, P., Surawicz, G., Harig,
 913 R., Baier, B. C., Bès, C., Bi, J., Boesch, H., Butz, A., Cai, Z., Chen, J., Crowell, S. M., Deutscher, N. M., Ene, D.,
 914 Franklin, J. E., García, O., Griffith, D., Grouiez, B., Grutter, M., Hamdouni, A., Houweling, S., Humpage, N.,
 915 Jacobs, N., Jeong, S., Joly, L., Jones, N. B., Jouglet, D., Kivi, R., Kleinschek, R., Lopez, M., Medeiros, D. J.,
 916 Morino, I., Mostafavipak, N., Müller, A., Ohyama, H., Palmer, P. I., Pathakoti, M., Pollard, D. F., Raffalski, U.,
 917 Ramonet, M., Ramsay, R., Sha, M. K., Shiomi, K., Simpson, W., Stremme, W., Sun, Y., Tanimoto, H., Té, Y.,
 918 Tsidu, G. M., Velazco, V. A., Vogel, F., Watanabe, M., Wei, C., Wunch, D., Yamasoe, M., Zhang, L., and Orphal,
 919 J.: Improved calibration procedures for the EM27/SUN spectrometers of the Collaborative Carbon Column
 920 Observing Network (COCCON), *Atmospheric Measurement Techniques*, 15, 2433–2463,
 921 <https://doi.org/10.5194/amt-15-2433-2022>, 2022.
- 922 Babenhauserheide, A., Hase, F., and Morino, I.: The Fossil Fuel Emissions of Tokyo estimated directly from
 923 measurements of the Tsukuba TCCON site, *Gases/Remote Sensing/Data Processing and Information Retrieval*,
 924 <https://doi.org/10.5194/amt-2018-224>, 2018.
- 925 Baylon, J. L., Stremme, W., Grutter, M., Hase, F., and Blumenstock, T.: Background
 926 CO₂ levels and error analysis from ground-based solar absorption IR measurements in
 927 central Mexico, *Atmos. Meas. Tech.*, 10, 2425–2434, <https://doi.org/10.5194/amt-10-2425-2017>, 2017.
- 928 Betts, R. A., Jones, C. D., Knight, Jeff. R., Keeling, Ralph. F., Kennedy, John. J., Wiltshire, A. J., Andrew, R.
 929 M., and Aragão, L. E. O. C.: A successful prediction of the record CO₂ rise associated with the 2015/2016 El
 930 Niño, *Phil. Trans. R. Soc. B*, 373, 20170301, <https://doi.org/10.1098/rstb.2017.0301>, 2018.
- 931 Bezanilla, A., Krüger, A., Stremme, W., and Grutter, M.: Solar absorption infrared spectroscopic
 932 measurements over Mexico City: Methane enhancements, *Atmósfera*, 27, 173–183,
 933 [https://doi.org/10.1016/S0187-6236\(14\)71108-7](https://doi.org/10.1016/S0187-6236(14)71108-7), 2014.
- 934 Borsdorff, T., Hasekamp, O. P., Wassmann, A., and Landgraf, J.: Insights into Tikhonov regularization:
 935 application to trace gas column retrieval and the efficient calculation of total column averaging kernels, *Atmos.*
 936 *Meas. Tech.*, 7, 523–535, <https://doi.org/10.5194/amt-7-523-2014>, 2014.
- 937 Borsdorff, T., Aan de Brugh, J., Hu, H., Aben, I., Hasekamp, O., and Landgraf, J.: Measuring Carbon
 938 Monoxide With TROPOMI: First Results and a Comparison With ECMWF-IFS Analysis Data, *Geophysical*
 939 *Research Letters*, 45, 2826–2832, <https://doi.org/10.1002/2018GL077045>, 2018.
- 940 Borsdorff, T., García Reynoso, A., Maldonado, G., Mar-Morales, B., Stremme, W., Grutter, M., and Landgraf,
 941 J.: Monitoring CO emissions of the metropolis Mexico City using TROPOMI CO observations, *Atmos. Chem.*
 942 *Phys.*, 20, 15761–15774, <https://doi.org/10.5194/acp-20-15761-2020>, 2020.
- 943 Bravo Cabrera, J. L., Azpra Romero, E., Rodriguez Gonzalez, F. J., and Rodriguez López, O.: Effects of ENSO
 944 on precipitation in Mexico City, *Investigaciones Geográficas*, <https://doi.org/10.14350/ig.59679>, 2018.
- 945 Buchwitz, M., Reuter, M., Schneising, O., Noël, S., Gier, B., Bovensmann, H., Burrows, J. P., Boesch, H.,
 946 Anand, J., Parker, R. J., Somkuti, P., Detmers, R. G., Hasekamp, O. P., Aben, I., Butz, A., Kuze, A., Suto, H.,
 947 Yoshida, Y., Crisp, D., and O'Dell, C.: Computation and analysis of atmospheric carbon dioxide annual mean
 948 growth rates from satellite observations during 2003–2016, *Atmos. Chem. Phys.*, 18, 17355–17370,
 949 <https://doi.org/10.5194/acp-18-17355-2018>, 2018.
- 950 Burgos-Cuevas, A., Magaldi, A., Adams, D. K., Grutter, M., García Franco, J. L., and Ruiz-Angulo, A.:
 951 Boundary Layer Height Characteristics in Mexico City from Two Remote Sensing Techniques, *Boundary-Layer*
 952 *Meteorol.*, 186, 287–304, <https://doi.org/10.1007/s10546-022-00759-w>, 2023.
- 953 Che, K., Cai, Z., Liu, Y., Wu, L., Yang, D., Chen, Y., Meng, X., Zhou, M., Wang, J., Yao, L., and Wang, P.:
 954 Lagrangian inversion of anthropogenic CO₂ emissions from Beijing using differential column measurements,
 955 *Environ. Res. Lett.*, 17, 075001, <https://doi.org/10.1088/1748-9326/ac7477>, 2022.
- 956 Che, K., Lauvaux, T., Taquet, N., Stremme, W., Xu, Y., Alberti, C., Lopez, M., García-Reynoso, A., Ciais, P.,
 957 Liu, Y., Ramonet, M., Grutter, M. (2024). CO₂ emissions estimate from Mexico City using ground- and space-
 958 based remote sensing. submitted to *Journal of Geophysical Research*.
- 959 Che, K., Lauvaux, T., Taquet, N., Stremme, W., Xu, Y., Alberti, C., Lopez, M., García-Reynoso, A., Ciais, P.,
 960 Liu, Y., Ramonet, M., Grutter, M. (2024). Urban XCO₂ gradients from a dense network of solar absorption
 961 spectrometers and OCO-3 over Mexico City. *Journal of Geophysical Research: Atmospheres*, 129(9),
 962 e2023JD040063., <https://doi.org/10.1029/2023JD040063>

- 963 Chen, J., Viatte, C., Hedelius, J. K., Jones, T., Franklin, J. E., Parker, H., Gottlieb, E. W., Wennberg, P. O.,
 964 Dubey, M. K., and Wofsy, S. C.: Differential column measurements using compact solar-tracking spectrometers,
 965 *Atmos. Chem. Phys.*, 16, 8479–8498, <https://doi.org/10.5194/acp-16-8479-2016>, 2016.
- 966 Chevallier, F., Deutscher, N. M., Conway, T. J., Ciais, P., Ciattaglia, L., Dohe, S., Fröhlich, M., Gomez-Pelaez,
 967 A. J., Griffith, D., Hase, F., Haszpra, L., Krummel, P., Kyrö, E., Labuschagne, C., Langenfelds, R., Machida, T.,
 968 Maignan, F., Matsueda, H., Morino, I., Notholt, J., Ramonet, M., Sawa, Y., Schmidt, M., Sherlock, V., Steele, P.,
 969 Strong, K., Sussmann, R., Wennberg, P., Wofsy, S., Worthy, D., Wunch, D., and Zimnoch, M.: Global CO₂ fluxes
 970 inferred from surface air-sample measurements and from TCCON retrievals of the CO₂ total column: TWO CO₂
 971 FLUX INVERSIONS, *Geophys. Res. Lett.*, 38, n/a-n/a, <https://doi.org/10.1029/2011GL049899>, 2011.
- 972 de Foy, B., Varela, J. R., Molina, L. T., and Molina, M. J.: Rapid ventilation of the Mexico City basin and
 973 regional fate of the urban plume, *Atmos. Chem. Phys.*, 6, 2321–2335, <https://doi.org/10.5194/acp-6-2321-2006>,
 974 2006.
- 975 Duren, R. M. and Miller, C. E.: Measuring the carbon emissions of megacities, *Nature Clim Change*, 2, 560–
 976 562, <https://doi.org/10.1038/nclimate1629>, 2012.
- 977 Frey, M., Sha, M. K., Hase, F., Kiel, M., Blumenstock, T., Harig, R., Surawicz, G., Deutscher, N. M., Shiomi,
 978 K., Franklin, J. E., Bösch, H., Chen, J., Grutter, M., Ohyama, H., Sun, Y., Butz, A., Mengistu Tsidu, G., Ene, D.,
 979 Wunch, D., Cao, Z., Garcia, O., Ramonet, M., Vogel, F., and Orphal, J.: Building the COllaborative Carbon
 980 Column Observing Network (COCCON): long-term stability and ensemble performance of the EM27/SUN
 981 Fourier transform spectrometer, *Atmos. Meas. Tech.*, 12, 1513–1530, <https://doi.org/10.5194/amt-12-1513-2019>,
 982 2019.
- 983 Frey, M. M., Hase, F., Blumenstock, T., Dubravica, D., Groß, J., Göttsche, F., Handjaba, M., Amadhila, P.,
 984 Mushi, R., Morino, I., Shiomi, K., Sha, M. K., De Mazière, M., and Pollard, D. F.: Long-term column-averaged
 985 greenhouse gas observations using a COCCON spectrometer at the high-surface-albedo site in Gobabeb, Namibia,
 986 *Atmos. Meas. Tech.*, 14, 5887–5911, <https://doi.org/10.5194/amt-14-5887-2021>, 2021.
- 987 García-Franco, J. L., Stremme, W., Bezanilla, A., Ruiz-Angulo, A., and Grutter, M.: Variability of the Mixed-
 988 Layer Height Over Mexico City, *Boundary-Layer Meteorol.*, 167, 493–507, <https://doi.org/10.1007/s10546-018-0334-x>, 2018.
- 989 García-Franco, J. L.: Air quality in Mexico City during the fuel shortage of January 2019. *Atmospheric*
 990 *environment*, 222, 117131, 2020.
- 991 Gisi, M.: Setup of precise camera based solar tracker systems and greenhouse gas measurements using a
 992 modified portable spectrometer, <https://doi.org/10.5445/IR/1000031248>, 2012.
- 993 Gisi, M., Hase, F., Dohe, S., and Blumenstock, T.: Camtracker: a new camera controlled high precision solar
 994 tracker system for FTIR-spectrometers, *Atmos. Meas. Tech.*, 4, 47–54, <https://doi.org/10.5194/amt-4-47-2011>,
 995 2011.
- 996 Gisi, M., Hase, F., Dohe, S., Blumenstock, T., Simon, A., and Keens, A.: XCO₂ measurements with a tabletop
 997 FTS using solar absorption spectroscopy, *Atmos. Meas. Tech.*, 5, 2969–2980, <https://doi.org/10.5194/amt-5-2969-2012>,
 998 2012.
- 1000 Goldberg, D. L., Lu, Z., Oda, T., Lamsal, L. N., Liu, F., Griffin, D., McLinden, C. A., Krotkov, N. A., Duncan,
 1001 B. N., and Streets, D. G.: Exploiting OMI NO₂ satellite observations to infer fossil-fuel CO₂ emissions from U.S.
 1002 megacities, *Science of The Total Environment*, 695, 133805, <https://doi.org/10.1016/j.scitotenv.2019.133805>,
 1003 2019.
- 1004 González Del Castillo, E., Taquet, N., Bezanilla, A., Stremme, W., Ramonet, M., Laurent, O., Xu, Y., Delmotte,
 1005 M., Grutter, M.: CO₂ variability in the Mexico City region from in situ measurements at an urban and a background
 1006 site, *Atm.*, 35, 377–393, <https://doi.org/10.20937/ATM.52956>, 2022.
- 1007 Grutter, M.: Multi-Gas analysis of ambient air using FTIR spectroscopy over Mexico City, *Atmosfera*, 16, 1–
 1008 13, 2003.
- 1009 Grutter, M., Rivera, O., Retama, A., Contreras, J., González, E., Porras, S., López, O., Arredondo, T., Díaz,
 1010 A., Robles, M., Sánchez B., Azpra, E., Ladino, L. Technical Report #4 in "EVALUACIÓN DE DISPOSITIVOS
 1011 BASADOS EN MICROSENSORES PARA EL MONITOREO CONTINUO DE LA CALIDAD DEL AIRE",
 1012 ICAYCC-UNAM 2023.
- 1013 Grutter, M., Flores, E., Basaldud, R., & Ruiz-Suárez, L. G. (2003). Open-path FTIR spectroscopic studies of
 1014 the trace gases over Mexico City. *ATMOSPHERIC AND OCEANIC OPTICS C/C OF OPTIKA ATMOSFERY I*
 1015 *OKEANA*, 16(3), 232-236.
- 1016 Gurney, K. R., Liang, J., O’Keeffe, D., Patarasuk, R., Hutchins, M., Huang, J., Rao, P., and Song, Y.:
 1017 Comparison of Global Downscaled Versus Bottom-Up Fossil Fuel CO₂ Emissions at the Urban Scale in Four U.S.
 1018 Urban Areas, *JGR Atmospheres*, 124, 2823–2840, <https://doi.org/10.1029/2018JD028859>, 2019.
- 1019 Hakkarainen, J., Szelağ, M. E., Ialongo, I., Retscher, C., Oda, T., and Crisp, D.: Analyzing nitrogen oxides to
 1020 carbon dioxide emission ratios from space: A case study of Matimba Power Station in South Africa, *Atmospheric*
 1021 *Environment: X*, 10, 100110, <https://doi.org/10.1016/j.aeaoa.2021.100110>, 2021.

- 1022 Hardy, C. C.: Smoke management guide for prescribed and wildland fire, National Wildlife Coordinating
1023 Group, 2001.
- 1024 Hase, F., Hannigan, J. W., Coffey, M. T., Goldman, A., Höpfner, M., Jones, N. B., Rinsland, C. P., and Wood,
1025 S. W.: Intercomparison of retrieval codes used for the analysis of high-resolution, ground-based FTIR
1026 measurements, *Journal of Quantitative Spectroscopy and Radiative Transfer*, 87, 25–52,
1027 <https://doi.org/10.1016/j.jqsrt.2003.12.008>, 2004.
- 1028 Hase, F., Frey, M., Blumenstock, T., Groß, J., Kiel, M., Kohlhepp, R., Mengistu Tsidu, G., Schäfer, K., Sha,
1029 M. K., and Orphal, J.: Application of portable FTIR spectrometers for detecting greenhouse gas emissions of the
1030 major city Berlin, *Atmos. Meas. Tech.*, 8, 3059–3068, <https://doi.org/10.5194/amt-8-3059-2015>, 2015.
- 1031 Hase, F., Frey, M., Kiel, M., Blumenstock, T., Harig, R., Keens, A., and Orphal, J.: Addition of a channel for
1032 XCO observations to a portable FTIR spectrometer for greenhouse gas measurements, *Atmospheric Measurement*
1033 *Techniques*, 9, 2303–2313, 2016.
- 1034 Hedelius, J. K., Viatte, C., Wunch, D., Roehl, C. M., Toon, G. C., Chen, J., Jones, T., Wofsy, S. C., Franklin,
1035 J. E., Parker, H., Dubey, M. K., and Wennberg, P. O.: Assessment of errors and biases in retrievals of XCO₂,
1036 XCH₄, XCO, and XN₂O from a 0.5 cm⁻¹ resolution solar-viewing spectrometer, *Atmos. Meas. Tech.*, 9,
1037 3527–3546, <https://doi.org/10.5194/amt-9-3527-2016>, 2016.
- 1038 Hedelius, J. K., Liu, J., Oda, T., Maksyutov, S., Roehl, C. M., Iraci, L. T., Podolske, J. R., Hillyard, P. W.,
1039 Liang, J., Gurney, K. R., Wunch, D., and Wennberg, P. O.: Southern California megacity
1040 CO₂ and CH₄ flux estimates using ground- and space-
1041 based remote sensing and a Lagrangian model, *Atmos. Chem. Phys.*, 18, 16271–16291,
1042 <https://doi.org/10.5194/acp-18-16271-2018>, 2018.
- 1043 Hernández-Paniagua, I. Y., Valdez, S. I., Almanza, V., Rivera-Cárdenas, C., Grutter, M., Stremme, W., García
1044 Reynoso, A., Ruiz-Suárez, L. G. (2021). Impact of the COVID-19 lockdown on air quality and resulting public
1045 health benefits in the Mexico City metropolitan area. *Frontiers in public health*, 9, 642630.
- 1046 Herrera, B., Bezanilla, A., Blumenstock, T., Dammers, E., Hase, F., Clarisse, L., Magaldi, A., Rivera, C.,
1047 Stremme, W., Strong, K., Viatte, C., Van Damme, M., and Grutter, M.: Measurement report: Evolution and
1048 distribution of NH₃ over Mexico City from ground-based and satellite infrared spectroscopic measurements,
1049 *Atmos. Chem. Phys.*, 22, 14119–14132, <https://doi.org/10.5194/acp-22-14119-2022>, 2022.
- 1050 Hersbach, H., Bell, B., Berrisford, P., Hirahara, S., Horányi, A., Muñoz-Sabater, J., Nicolas, J., Peubey, C.,
1051 Radu, R., Schepers, D., Simmons, A., Soci, C., Abdalla, S., Abellan, X., Balsamo, G., Bechtold, P., Biavati, G.,
1052 Bidlot, J., Bonavita, M., De Chiara, G., Dahlgren, P., Dee, D., Diamantakis, M., Dragani, R., Flemming, J., Forbes,
1053 R., Fuentes, M., Geer, A., Haimberger, L., Healy, S., Hogan, R. J., Hólm, E., Janisková, M., Keeley, S., Laloyaux,
1054 P., Lopez, P., Lupu, C., Radnoti, G., De Rosnay, P., Rozum, I., Vamborg, F., Villaume, S., and Thépaut, J.: The
1055 ERA5 global reanalysis, *Quart J Royal Meteorol Soc*, 146, 1999–2049, <https://doi.org/10.1002/qj.3803>, 2020.
- 1056 Jones, C. D., Hickman, J. E., Rumbold, S. T., Walton, J., Lamboll, R. D., Skeie, R. B., Fiedler, S., Forster, P.,
1057 M., Rogelj, J., Abe, M., Botzet, M., Calvin, K., Cassou, C., Cole, J. N. S., Davini, P., Deushi, M., Dix, M., Fyfe,
1058 J. C., Gillett, N. P., Ilyina, T., Kawamiya, M., Kelley, M., Kharin, S., Koshiro, T., Li, H., Mackallah, C., Müller,
1059 W. A., Nabat, P., Van Noije, T., Nolan, P., Ohgaito, R., Olivie, D., Oshima, N., Parodi, J., Reerink, T. J., Ren, L.,
1060 Romanou, A., Séférian, R., Tang, Y., Timmreck, C., Tjiputra, J., Tourigny, E., Tsigaridis, K., Wang, H., Wu, M.,
1061 Wyser, K., Yang, S., Yang, Y., and Ziehn, T.: The Climate Response to Emissions Reductions Due to COVID-19:
1062 Initial Results From CovidMIP, *Geophysical Research Letters*, 48, e2020GL091883,
1063 <https://doi.org/10.1029/2020GL091883>, 2021.
- 1064 Kiel, M., Eldering, A., Roten, D. D., Lin, J. C., Feng, S., Lei, R., Lauvaux, T., Oda, T., Roehl, C. M., Blavier,
1065 J.-F., and Iraci, L. T.: Urban-focused satellite CO₂ observations from the Orbiting Carbon Observatory-3: A first
1066 look at the Los Angeles megacity, *Remote Sensing of Environment*, 258, 112314,
1067 <https://doi.org/10.1016/j.rse.2021.112314>, 2021.
- 1068 Kutralam-Muniasamy, G., Pérez-Guevara, F., Roy, P. D., Elizalde-Martínez, I., and Shruti, V. C.: Impacts of
1069 the COVID-19 lockdown on air quality and its association with human mortality trends in megapolis Mexico City,
1070 *Air Qual Atmos Health*, 14, 553–562, <https://doi.org/10.1007/s11869-020-00960-1>, 2021.
- 1071 Le Quéré, C., Jackson, R. B., Jones, M. W., Smith, A. J. P., Abernethy, S., Andrew, R. M., De-Gol, A. J.,
1072 Willis, D. R., Shan, Y., Canadell, J. G., Friedlingstein, P., Creutzig, F., and Peters, G. P.: Temporary reduction in
1073 daily global CO₂ emissions during the COVID-19 forced confinement, *Nat. Clim. Chang.*, 10, 647–653,
1074 <https://doi.org/10.1038/s41558-020-0797-x>, 2020.
- 1075 Lei, R., Feng, S., Danjou, A., Broquet, G., Wu, D., Lin, J. C., O'Dell, C. W., and Lauvaux, T.: Fossil fuel CO₂
1076 emissions over metropolitan areas from space: A multi-model analysis of OCO-2 data over Lahore, Pakistan,
1077 *Remote Sensing of Environment*, 264, 112625, <https://doi.org/10.1016/j.rse.2021.112625>, 2021.
- 1078 Lian, J., Lauvaux, T., Utard, H., Bréon, F.-M., Broquet, G., Ramonet, M., Laurent, O., Albarus, I., Chariot, M.,
1079 Kotthaus, S., Haefelin, M., Sanchez, O., Perrussel, O., Denier Van Der Gon, H. A., Dellaert, S. N. C., and Ciais,
1080 P.: Can we use atmospheric CO₂ measurements to verify emission trends reported by cities? Lessons from a six-

- 1081 year atmospheric inversion over Paris, *Gases/Atmospheric Modelling and Data Analysis/Troposphere/Physics*
 1082 (physical properties and processes), <https://doi.org/10.5194/egusphere-2023-401>, 2023.
- 1083 Liu, Z., Ciais, P., Deng, Z., Lei, R., Davis, S. J., Feng, S., Zheng, B., Cui, D., Dou, X., Zhu, B., Guo, R., Ke,
 1084 P., Sun, T., Lu, C., He, P., Wang, Y., Yue, X., Wang, Y., Lei, Y., Zhou, H., Cai, Z., Wu, Y., Guo, R., Han, T.,
 1085 Xue, J., Boucher, O., Boucher, E., Chevallier, F., Tanaka, K., Wei, Y., Zhong, H., Kang, C., Zhang, N., Chen, B.,
 1086 Xi, F., Liu, M., Bréon, F.-M., Lu, Y., Zhang, Q., Guan, D., Gong, P., Kammen, D. M., He, K., and Schellnhuber,
 1087 H. J.: Near-real-time monitoring of global CO₂ emissions reveals the effects of the COVID-19 pandemic, *Nat*
 1088 *Commun*, 11, 5172, <https://doi.org/10.1038/s41467-020-18922-7>, 2020.
- 1089 Lu, S., Wang, J., Wang, Y., and Yan, J.: Analysis on the variations of atmospheric CO₂ concentrations along
 1090 the urban–rural gradients of Chinese cities based on the OCO-2 XCO₂ data, *International Journal of Remote*
 1091 *Sensing*, 39, 4194–4213, <https://doi.org/10.1080/01431161.2017.1415482>, 2018.
- 1092 MacDonald, C. G., Mastrogiacomo, J.-P., Laughner, J. L., Hedelius, J. K., Nassar, R., and Wunch, D.:
 1093 Estimating enhancement ratios of nitrogen dioxide, carbon monoxide and carbon dioxide using satellite
 1094 observations, *Atmos. Chem. Phys.*, 23, 3493–3516, <https://doi.org/10.5194/acp-23-3493-2023>, 2023.
- 1095 Makarova, M. V., Alberti, C., Ionov, D. V., Hase, F., Foka, S. C., Blumenstock, T., Warneke, T., Virolainen,
 1096 Y. A., Kostsov, V. S., Frey, M., Poberovskii, A. V., Timofeyev, Y. M., Paramonova, N. N., Volkova, K. A.,
 1097 Zaitsev, N. A., Biryukov, E. Y., Osipov, S. I., Makarov, B. K., Polyakov, A. V., Ivakhov, V. M., Imhasin, H. Kh.,
 1098 and Mikhailov, E. F.: Emission Monitoring Mobile Experiment (EMME): an overview and first results of the St.
 1099 Petersburg megacity campaign-2019, *Gases/Remote Sensing/Instruments and Platforms*,
 1100 <https://doi.org/10.5194/amt-2020-87>, 2020.
- 1101 Molina, L. T., Madronich, S., Gaffney, J. S., Apel, E., De Foy, B., Fast, J., Ferrare, R., Herndon, S., Jimenez,
 1102 J. L., Lamb, B., Osornio-Vargas, A. R., Russell, P., Schauer, J. J., Stevens, P. S., Volkamer, R., and Zavala, M.:
 1103 An overview of the MILAGRO 2006 Campaign: Mexico City emissions and their transport and transformation,
 1104 *Atmos. Chem. Phys.*, 10, 8697–8760, <https://doi.org/10.5194/acp-10-8697-2010>, 2010.
- 1105 Molina, L. T. Introductory lecture: air quality in megacities. *Faraday discussions*, 226, 9-52, 2021.
- 1106 Park, H., Jeong, S., Park, H., Labzovskii, L. D., and Bowman, K. W.: An assessment of emission characteristics
 1107 of Northern Hemisphere cities using spaceborne observations of CO₂, CO, and NO₂, *Remote Sensing of*
 1108 *Environment*, 254, 112246, <https://doi.org/10.1016/j.rse.2020.112246>, 2021.
- 1109 Porras, S., González del Castillo, M.E., López, O., Arredondo, T., Rivera, O., Ramonet, M., Laurent, O.,
 1110 Grutter, M.: Diseño y despliegue de una red piloto para la medición de CO₂ con un sistema de microsensores,
 1111 UNAM internal report, 2023: [http://www.epr.atmosfera.unam.mx/Microsensores-](http://www.epr.atmosfera.unam.mx/Microsensores-2022/documentos/4_Red_piloto_CO2.pdf)
 1112 [2022/documentos/4_Red_piloto_CO2.pdf](http://www.epr.atmosfera.unam.mx/Microsensores-2022/documentos/4_Red_piloto_CO2.pdf) (last accessed on May 20, 2024)
- 1113 Plaza-Medina, E. F., Stremme, W., Bezanilla, A., Grutter, M., Schneider, M., Hase, F., and Blumenstock, T.:
 1114 Ground-based remote sensing of O₃ by high- and medium-resolution FTIR spectrometers over the Mexico City
 1115 basin, *Atmos. Meas. Tech.*, 10, 2703–2725, <https://doi.org/10.5194/amt-10-2703-2017>, 2017.
- 1116 Pougatchev, N. S., Jones, N. B., Connor, B. J., Rinsland, C. P., Becker, E., Coffey, M. T., Connors, V. S.,
 1117 Demoulin, P., Dzhola, A. V., Fast, H., Grechko, E. I., Hannigan, J. W., Koike, M., Kondo, Y., Mahieu, E., Mankin,
 1118 W. G., Mittermeier, R. L., Notholt, J., Reichle, H. G., Sen, B., Steele, L. P., Toon, G. C., Yurganov, L. N., Zander,
 1119 R., and Zhao, Y.: Ground-based infrared solar spectroscopic measurements of carbon monoxide during 1994
 1120 *Measurement of Air Pollution From Space flights*, *J. Geophys. Res.*, 103, 19317–19325,
 1121 <https://doi.org/10.1029/97JD02889>, 1998.
- 1122 Rinsland, C. P., Jones, N. B., Connor, B. J., Logan, J. A., Pougatchev, N. S., Goldman, A., Murcray, F. J.,
 1123 Stephen, T. M., Pine, A. S., Zander, R., Mahieu, E., and Demoulin, P.: Northern and southern hemisphere ground-
 1124 based infrared spectroscopic measurements of tropospheric carbon monoxide and ethane, *J. Geophys. Res.*, 103,
 1125 28197–28217, <https://doi.org/10.1029/98JD02515>, 1998.
- 1126 Reißmann, M., Chen, J., Osterman, G., Zhao, X., Dietrich, F., Makowski, M., Hase, F., and Kiel, M.:
 1127 Comparison of OCO-2 target observations to MUCCnet – is it possible to capture urban XCO₂ gradients from
 1128 space?, *Atmos. Meas. Tech.*, 15, 6605–6623, <https://doi.org/10.5194/amt-15-6605-2022>, 2022.
- 1129 Rivera Cárdenas, C., Guarín, C., Stremme, W., Friedrich, M. M., Bezanilla, A., Rivera Ramos, D., Mendoza-
 1130 Rodríguez, C. A., Grutter, M., Blumenstock, T., and Hase, F.: Formaldehyde total column densities over Mexico
 1131 City: comparison between multi-axis differential optical absorption spectroscopy and solar-absorption Fourier
 1132 transform infrared measurements, *Atmos. Meas. Tech.*, 14, 595–613, <https://doi.org/10.5194/amt-14-595-2021>,
 1133 2021.
- 1134 Rodgers, C. D.: *Inverse Methods for Atmospheric Sounding: Theory and Practice*, WORLD SCIENTIFIC,
 1135 <https://doi.org/10.1142/3171>, 2000.
- 1136 Sha, M. K., De Mazière, M., Notholt, J., Blumenstock, T., Chen, H., Dehn, A., Griffith, D. W. T., Hase, F.,
 1137 Heikkinen, P., Hermans, C., Hoffmann, A., Huebner, M., Jones, N., Kivi, R., Langerock, B., Petri, C., Scolas, F.,
 1138 Tu, Q., and Weidmann, D.: Intercomparison of low- and high-resolution infrared spectrometers for ground-based
 1139 solar remote sensing measurements of total column concentrations of CO₂, CH₄ and CO, *Atmos. Meas. Tech.*,
 1140 13, 4791–4839, <https://doi.org/10.5194/amt-13-4791-2020>, 2020.

- 1141 Silva, S. J., Arellano, A. F., and Worden, H. M.: Toward anthropogenic combustion emission constraints from
 1142 space-based analysis of urban CO₂ /CO sensitivity, *Geophysical Research Letters*, 40, 4971–4976,
 1143 <https://doi.org/10.1002/grl.50954>, 2013.
- 1144 Storey, M. A. and Price, O. F.: Prediction of air quality in Sydney, Australia as a function of forest fire load
 1145 and weather using Bayesian statistics, *PLoS ONE*, 17, e0272774, <https://doi.org/10.1371/journal.pone.0272774>,
 1146 2022.
- 1147 Stremme, W., Ortega, I., and Grutter, M.: Using ground-based solar and lunar infrared spectroscopy to study
 1148 the diurnal trend of carbon monoxide in the Mexico City boundary layer, *Atmos. Chem. Phys.*, 9, 8061–8078,
 1149 <https://doi.org/10.5194/acp-9-8061-2009>, 2009.
- 1150 Stremme, W., Grutter, M., Rivera, C., Bezanilla, A., Garcia, A. R., Ortega, I., George, M., Clerbaux, C.,
 1151 Coheur, P.-F., Hurtmans, D., Hannigan, J. W., and Coffey, M. T.: Top-down estimation of carbon monoxide
 1152 emissions from the Mexico Megacity based on FTIR measurements from ground and space, *Atmos. Chem. Phys.*,
 1153 13, 1357–1376, <https://doi.org/10.5194/acp-13-1357-2013>, 2013.
- 1154 Su, T., Li, Z., and Kahn, R.: Relationships between the planetary boundary layer height and surface pollutants
 1155 derived from lidar observations over China: regional pattern and influencing factors, *Atmos. Chem. Phys.*, 18,
 1156 15921–15935, <https://doi.org/10.5194/acp-18-15921-2018>, 2018.
- 1157 Sussmann, R. and Rettinger, M.: Can We Measure a COVID-19-Related Slowdown in Atmospheric CO₂
 1158 Growth? Sensitivity of Total Carbon Column Observations, *Remote Sensing*, 12, 2387,
 1159 <https://doi.org/10.3390/rs12152387>, 2020.
- 1160 Toon, G., Blavier, J.-F., Washenfelder, R., Wunch, D., Keppel-Aleks, G., Wennberg, P., Connor, B., Sherlock,
 1161 V., Griffith, D., Deutscher, N., and Notholt, J.: Total Column Carbon Observing Network (TCCON), in: *Advances*
 1162 *in Imaging, Advances in Imaging*, Vancouver, journalAbbreviation: HISensE, JMA3, 2009.
- 1163 Viatte, C., Lauvaux, T., Hedelius, J. K., Parker, H., Chen, J., Jones, T., Franklin, J. E., Deng, A. J., Gaudet, B.,
 1164 Verhulst, K., Duren, R., Wunch, D., Roehl, C., Dubey, M. K., Wofsy, S., and Wennberg, P. O.: Methane emissions
 1165 from dairies in the Los Angeles Basin, *Atmos. Chem. Phys.*, 17, 7509–7528, [https://doi.org/10.5194/acp-17-7509-](https://doi.org/10.5194/acp-17-7509-2017)
 1166 [2017](https://doi.org/10.5194/acp-17-7509-2017), 2017.
- 1167 Vogel, F. R., Frey, M., Stauffer, J., Hase, F., Broquet, G., Xueref-Remy, I., Chevallier, F., Ciais, P., Sha, M. K.,
 1168 Chelin, P., Jeseck, P., Janssen, C., Té, Y., Groß, J., Blumenstock, T., Tu, Q., and Orphal, J.:
 1169 XCO₂ in an emission hot-spot region: the COCCON Paris campaign 2015, *Atmos. Chem.*
 1170 *Phys.*, 19, 3271–3285, <https://doi.org/10.5194/acp-19-3271-2019>, 2019.
- 1171 Wang, H., Jiang, F., Wang, J., Ju, W., and Chen, J. M.: Terrestrial ecosystem carbon flux estimated using
 1172 GOSAT and OCO-2 XCO₂ retrievals, *Atmos. Chem. Phys.*, 19, 12067–12082,
 1173 <https://doi.org/10.5194/acp-19-12067-2019>, 2019.
- 1174 Wang, Y., Broquet, G., Bréon, F.-M., Lespinas, F., Buchwitz, M., Reuter, M., Meijer, Y., Loescher, A.,
 1175 Janssens-Maenhout, G., Zheng, B., and Ciais, P.: PMIF v1.0: assessing the potential of satellite observations to
 1176 constrain CO₂; emissions from large cities and point sources over the globe using synthetic data, *Geosci. Model*
 1177 *Dev.*, 13, 5813–5831, <https://doi.org/10.5194/gmd-13-5813-2020>, 2020.
- 1178 Wu, D., Lin, J. C., Fasoli, B., Oda, T., Ye, X., Lauvaux, T., Yang, E. G., and Kort, E. A.: A Lagrangian
 1179 approach towards extracting signals of urban CO₂ emissions from satellite observations of atmospheric column
 1180 CO₂ (XCO₂): X-Stochastic Time-Inverted Lagrangian Transport model (“X-STILT v1”), *Geosci. Model Dev.*,
 1181 11, 4843–4871, <https://doi.org/10.5194/gmd-11-4843-2018>, 2018.
- 1182 Wunch, D., Wennberg, P. O., Toon, G. C., Keppel-Aleks, G., and Yavin, Y. G.: Emissions of greenhouse gases
 1183 from a North American megacity, *Geophysical Research Letters*, 36, 2009GL039825,
 1184 <https://doi.org/10.1029/2009GL039825>, 2009.
- 1185 Xu, Y., Lauvaux T., Grutter, M., Taquet, N., García-Reynoso, J.A., Laurent, O., Lopez, M., Lian, J., Lin, X.,
 1186 Stremme, W., Ramonet, M., Atmospheric CO₂ dynamics over a mountain urban basin: a case study of the Mexico
 1187 City metropolitan area, submitted.
- 1188 Ye, X., Lauvaux, T., Kort, E. A., Oda, T., Feng, S., Lin, J. C., Yang, E., and Wu, D.: Constraining fossil fuel
 1189 CO₂ emissions from urban area using OCO-2 observations of total column
 1190 CO₂, *Gases/Atmospheric Modelling/Troposphere/Physics (physical properties and*
 1191 *processes)*, <https://doi.org/10.5194/acp-2017-1022>, 2017.
- 1192 You, Y., Byrne, B., Colebatch, O., Mittermeier, R. L., Vogel, F., and Strong, K.: Quantifying the Impact of the
 1193 COVID-19 Pandemic Restrictions on CO, CO₂, and CH₄ in Downtown Toronto Using Open-Path Fourier
 1194 Transform Spectroscopy, *Atmosphere*, 12, 848, <https://doi.org/10.3390/atmos12070848>, 2021.
- 1195 Zhang, Q., Boersma, K. F., Zhao, B., Eskes, H., Chen, C., Zheng, H., and Zhang, X.: Quantifying daily NO_x
 1196 and CO₂ emissions from Wuhan using satellite observations from TROPOMI and OCO-2, *Atmos. Chem. Phys.*,
 1197 23, 551–563, <https://doi.org/10.5194/acp-23-551-2023>, 2023.
- 1198 Zhao, X., Marshall, J., Hachinger, S., Gerbig, C., Frey, M., Hase, F., and Chen, J.: Analysis of total column
 1199 CO₂ and CH₄ measurements in Berlin with WRF-GHG, *Atmos. Chem. Phys.*, 19, 11279–11302,
 1200 <https://doi.org/10.5194/acp-19-11279-2019>, 2019.

1201 Zhou, M., Ni, Q., Cai, Z., Langerock, B., Nan, W., Yang, Y., Che, K., Yang, D., Wang, T., Liu, Y., and Wang,
1202 P.: CO₂ in Beijing and Xianghe Observed by Ground-Based FTIR Column Measurements and Validation to OCO-
1203 2/3 Satellite Observations, *Remote Sensing*, 14, 3769, <https://doi.org/10.3390/rs14153769>, 2022.

Supplement of

CO₂ and CO temporal variability over Mexico City from ground-based total column and surface measurements

N. taquet et al.

Correspondence to: Noémie Taquet (noemi.taquet@gmail.com)

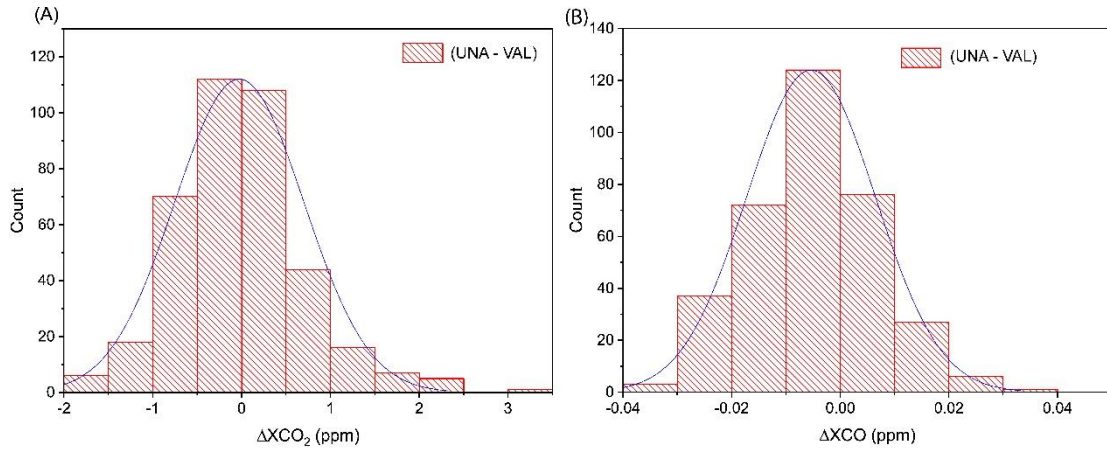


Figure S1: Statistical distribution of the (UNA-VAL) XCO₂ and XCO differences over the 2019-2021 period.

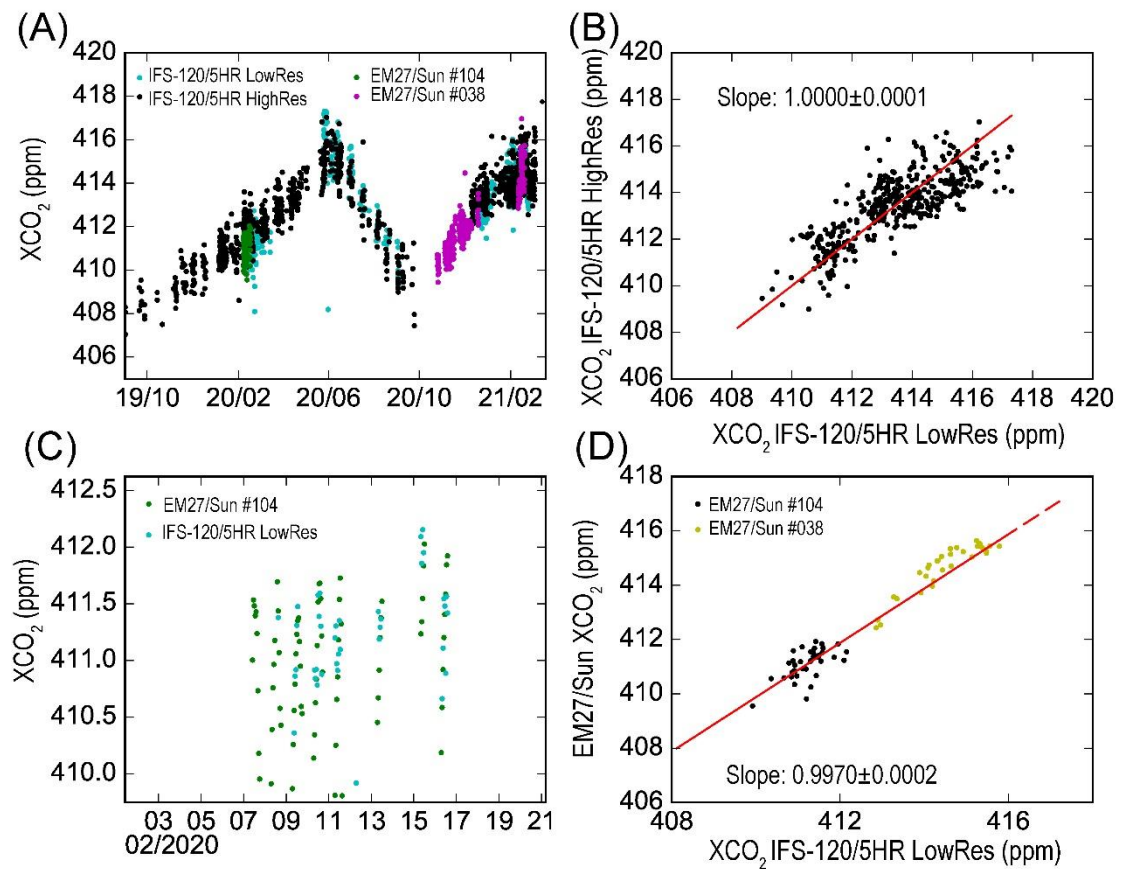


Figure S2: Determination of calibrated factors between the HR120/5 and EM27/Sun products from side-by-side measurements. (A) XCO₂ time series of from the different instruments. (B) Correlation plot of XCO₂ from the IFS120/5HR high and low resolution products after applying the calibration factors. (C) Zoom of (A) for February 2020. (D) Correlation plot of XCO₂ from EM27/Sun and IFS120/5HR low resolution products.

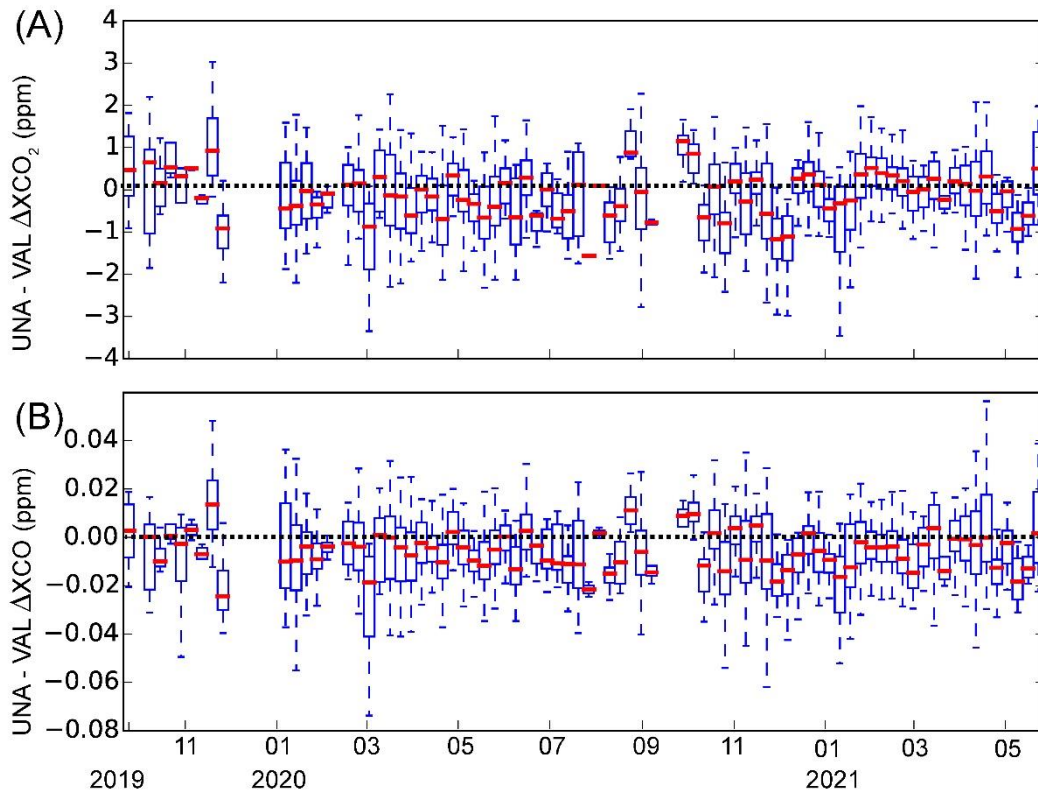


Figure S3: Whisker diagram representing the weekly-average difference between the UNA and VAL total columns of (A) XCO₂ and (B) XCO.

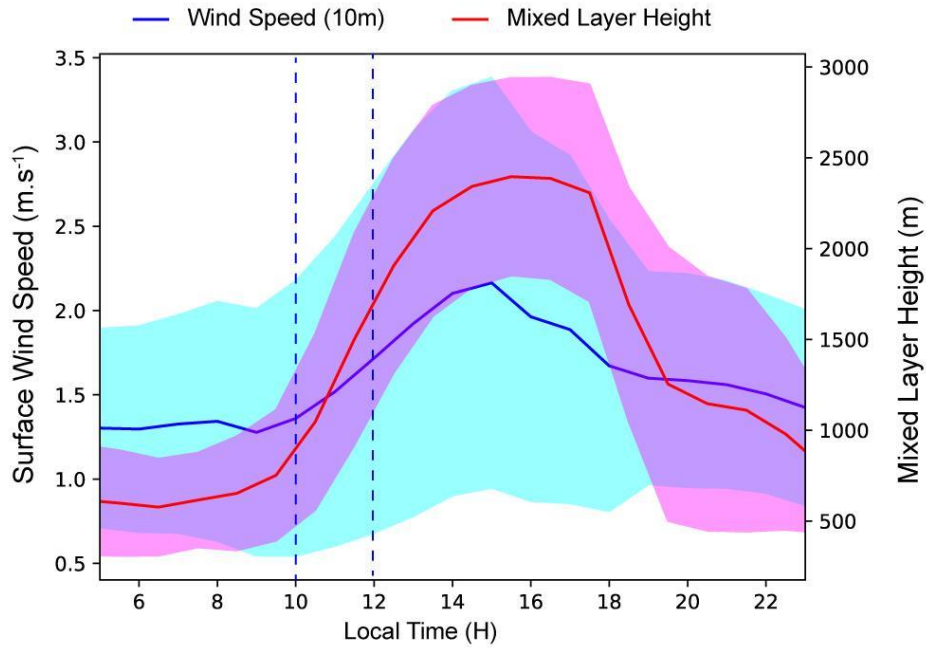


Figure S4: Diurnal pattern of the mixed layer height from the UNA ceilometer data and of the surface wind speed from the ERA5 data. The dash lines represent the time window used to calculate the XCO growth rate (see text for details).

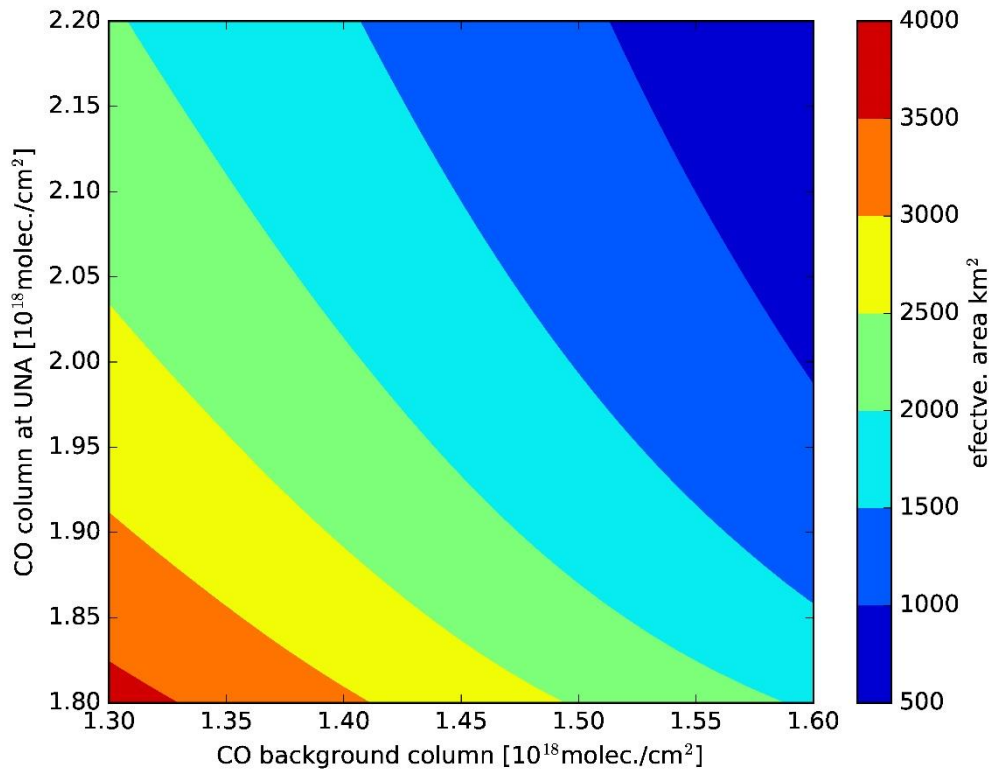


Figure S5: Sensitivity of the effective area to the background uncertainties.

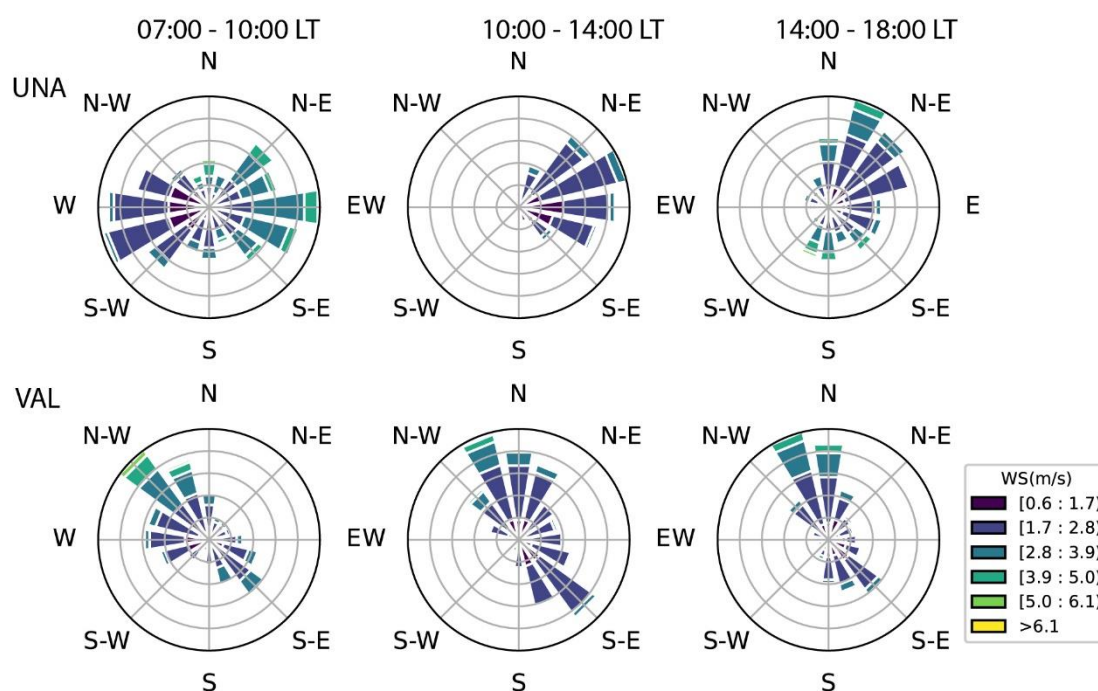


Figure S6: Dominant surface wind speed and direction at the UNA and VAL stations (average over 01/09/2019-01/06/2021) calculated from the Redmet and RUOA meteorological stations, selecting days complying with the VI filter (see text for details).

Table S1: Calibration factors determined for the intercalibration of all the FTIR studied products.

Instrument/product	Calibration factor
EM27_62 XCO ₂	1.0
EM27_104 XCO ₂	0.9983
EM27_38 XCO ₂	0.9986
EM27_62 XCO	1.0
EM27_104 XCO	1.0055
EM27_38 XCO	0.9907
HR_120/5 -XCO ₂	1.0043
VERTEX-XCO MIR	1.0001

Table S2: Parameters of correlation plots between the different products (after applying the calibration factors). R² stands for the coefficient of determination.

Instrument 1, product1	Instrument 2, product 2	Slope +/- errSlope; Offset +/- errOffset	R ²
EM27_62, XCO ₂	EM27_38 XCO ₂	1.00	1.0
EM27_62, XCO ₂	EM27_104 XCO ₂	1.00	1.0
EM27_104, XCO ₂	HR_120/5 -XCO ₂	0.9957+/-0.0002	0.96
EM27_38_104, XCO	HR_120/5 -XCO MIR	1.49+/-0.07 -0.034+/-0.005	0.96
HR_120/5 -XCO MIR	HR_120/5 -XCO NIR	0.98+/-0.01	0.96
EM27_62, XCO	VERTEX-XCO (MIR)	1.04+/-0.01	0.92

Table S3: CO and CO₂ emissions derived from inventories (SEDEMA) and from the FTIR data for the MCMA. *correspond to the indicated period but excluding the lock-down period.

Year	CO (inventory -Total) (kt/year)	CO (inventory Mobile source) (kt/year)	CO ₂ (inventory -Total) (kt/year)	CO ₂ (inventory) Mobile source) (kt/year)	CO (FTIR) from CO growth rates (kt/year)	CO (FTIR) uncert ainties ¹	CO ₂ (FTIR) from CO/CO ₂ ratio at UNA and CO growth rates (kt/year)	CO ₂ (FTIR) uncertainties ¹
2016	728.6	646.4	54,020	52,439	634.7	106.2	63,470	10,620
2018	728.9	689.3	66,031	43,217	716.6	64.3	71,660	6,430
2019					534.2	33.9	53,420	3,390
2020	974.0	928.5	58,273	35,271	328.4	18.7	32,840	1,870
2021					553.9	37.5	55,390	3,750
2016- 2020					547.6* 519.2	21.25* 21.4	54,760* 51,920	2,125* 2,400

¹ only includes the propagated growth rate error. An estimation of errors due to the spatial and temporal interpolation is given in Figure 11 and discussed in the text.